ABSTRACT

Title of Document: ENERGY SAVINGS AND THERMAL COMFORT OF SEPARATE SENSIBLE AND LATENT COOLING AIR-CONDITIONING SYSTEMS

Jiazhen Ling, Doctor of Philosophy, 2011

Directed By: Professor, Reinhard Radermacher, Mechanical Engineering

Conventional air conditioning (AC) systems have limited control of sensible cooling and latent cooling capacities; therefore additional energy-consuming devices, i.e. electric heaters, are often used to reheat the conditioned air in order to provide thermal comfort for the building occupants. Separate sensible and latent cooling (SSLC) AC systems are capable of providing better control of cooling at no extra overload in the form of energy input. Moreover, because of a higher coefficient of performance (COP) in the sensible cooling cycle, the SSLC technology reduces total energy input to vapor compression systems (VCS), and makes AC systems more energy efficient.

This dissertation explores and compares two main methods for implementing the SSLC concept: cycle options for SSLC systems and methods of indoor heat transfer. One of these options consists of two independent VCS, and the other consists of one VCS removing sensible load only and one solid desiccant wheel (DW) regenerated with the waste heat from the VCS. The objectives of the system option

study are to understand the reasons behind energy savings and explore the best possible configurations of SSLC systems in different summer outdoor conditions. The simulation results of the first kind of SSLC system show that the energy savings come from a reduced compressor power input of the sensible cycle. Under wide ranging ambient conditions, the amount of energy savings varies from 22% to 50% over conventional system energy input. However, such a system has limited independence of varying sensible to latent load ratio and the extra cost of an internal heat exchanger. The integration of VCS and DW overcomes these limitations. An experimental setup was constructed in an environmental chamber to test the performance of the second kind of SSLC system using carbon dioxide as refrigerant. The experimental results show only a 7% improvement by using SSLC systems, and two negative factors hindering SSLC systems from achieving more energy savings were later identified. As a result, the application of divided heat exchangers is proposed as a solution to address one of the issues. An optimal SSLC system, which incorporates the application of divided heat exchangers, an enthalpy wheel and other energy-saving methods, was modeled and demonstrated a doubling of the COP as compared to a conventional AC system.

The second method crucial to implementing SSLC is a so called “low ΔT indoor heat exchanger” which is being introduced as an improved sensible heat exchanger design for the successful implementation of SSLC system concept. Its capability of providing both radiative heat transfer and convective heat transfer leads to better thermal comfort to occupants. Compared to the baseline fan-coil unit, the low ΔT indoor heat exchanger creates better thermal comfort in terms of reducing

temperature stratification from head to feet by 0.8 K and providing higher operative temperature at the foot level in winter. Numerical models were developed to simulate the operative temperature field created by the low ΔT indoor heat exchanger. The model had only an average deviation of 0.4 K compared to the experimental data. The air temperature simulation in the model was later replaced by the proper orthogonal decomposition (POD) method. The POD method provides simulation results almost identical to CFD simulation (maximum deviation of 0.1 K), and moreover reduces the computation time from 24 hours to only minutes.

The major contributions in this dissertation are listed as follow:

Exploration of energy saving potential of the SSLC systems:

- Design, fabricated and tested an SSLC air conditioning system and compared its performance to a conventional system
- Compared the performance of SSLC systems using two refrigerants, R-410A and CO_2
- Based on experimental results, established models to simulate SSLC systems
    - Simulated SSLC system performance under different ambient conditions
    - Optimized the vapor compression cycle operation under each ambient condition
    - Explored maximum energy saving options (configurations) of an SSLC system

Thermal comfort study of the low ΔT heat exchanger:

- Established a low ΔT heat exchanger test facility with sensors for operative temperature measurement
- Compared the thermal comfort zone created by the baseline fan-coil unit and low ΔT heat exchanger system
- Developed models to simulate the thermal comfort zone in an office setting
    - Simulate natural convection by a commercial CFD tool and obtain 2D air temperature field in the conditioned space
    - Simulate radiation cooling (heating) and obtain 3D mean radiation temperature field in the conditioned space
- Developed a reduced-order POD model to replace the CFD simulation of air temperature in the conditioned space and verify the POD model by comparing its results to the original CFD model

ENERGY SAVINGS AND THERMAL COMFORT OF SEPARATE SENSIBLE AND LATENT COOLING AIR-CONDITIONING SYSTEMS

By

Jiazhen Ling

Dissertation submitted to the Faculty of the Graduate School of the
University of Maryland, College Park, in partial fulfillment
of the requirements for the degree of
Doctor of Philosophy
2011

Advisory Committee:
Professor Reinhard Radermacher, Chair
Assistant Professor Amir Riaz
Associate Professor Bao Yang
Associate Professor Gary Pertmer, Dean's representative
Professor Gregory Jackson
Research Associate Professor Yunho Hwang

Dedication

To Vivian Ling (凌薇薇)

My beloved daughter who will be born in September 2011

Acknowledgement

I am forever grateful for my advisor, Dr. Radermacher, for giving me the opportunity to conduct research at Center for Environmental Energy Engineering (CEEE). I came in as a student interested in obtaining a Ph.D. but through his guidance and advice, today I am a researcher interested in finding solutions to all problems. I am also grateful to my dissertation committee members, Dr. Jackson, Dr. Yang, Dr. Riaz and Dr. Pertmer for their time and effort in making this dissertation more valuable to the engineering and scientific community.

I would like to offer a special note of thanks for Dr. Hwang who gave me numerous advices and comments on my day-to-day research. He has shown unlimited amount of patience in answering my questions. His professional and meticulous working attitude also sets a great example for me.

I would also like to thank Mr. Osamu Kuwabara from Sanyo Electric. He taught me the skills of conducting experiments and made me feel like I am a real engineer. The working experience with him has become a valuable asset in my PhD study. The experiments related to the low ΔT heat exchangers would not exist in my dissertation without the help from Mathias Koepke. He set up the experimental facility and conducted the tests with great care. The data from the tests are priceless for my later research.

I would like to thank every colleague in CEEE for the help I received in the past four and half years, especially Jan Muehlbauer. His creative ideas on building

test facility saved me huge amounts of time and provided me with better results than I can ever imagine.

Most importantly, I am indebted to my wife Yuan Zhang and my parents. Without their continuous love and sacrifice, the achievement would not be possible.

Table of Contents

List of Tables

List of Figures

Nomenclature

a	Coefficient of the POD modes	
AR	Aspect ratio	
ARI	Air-Conditioning and Refrigeration Institute	
C	Kernel matrix	
CHP	Cooling, heating and power	
COP	Coefficient of performance	
c_p	Specific heat	($kJmol^{-1}k^{-1}$)
D	Diameter	(m)
e	Internal energy	($kJkg^{-1}$)
EES	Engineering equation solver	
F	View factor	
g	Gravitational acceleration	(ms^{-2})
Gr	Grashof number	
HX	Heat exchanger	
$\dot{m}$	Mass flow rate	(kgs^{-1})
N	Rotation speed	(rpm)
Nu	Nusselt number	
P	Pressure lift	(Pa)
Pr	Prandtl number	
PR	Pressure ratio	
$\ddot{q}$	Source term (per volume)	
Q	Air flow rate	(m^3s^{-1})
Ra	Rayleigh number	

RH	Relative humidity	
SHF	Sensible heat Factor	
SSLC	Separate sensible and latent cooling	
T	Temperature	(K)
UA	Overall heat transfer conductance of heat exchanger	(kWK^{-1})
V, *v*	Velocity	(ms^{-1})
VFR	Volume flow rate	(m^3s^{-1})

Greek Letters

α	Thermal diffusivity	(m^2s^{-1})
β	Thermal expansion coefficient	(K^{-1})
ε	Turbulent dissipation	
η	Compressor efficiency	
κ	Turbulent kinetic energy	
μ	Dynamic viscosity	(Pa·s)
ν	Kinematic viscosity	(m^2s^{-1})
ρ	Density	(kgm^{-3})
τ	Time term	
φ	POD mode	
Φ	Dissipation term	
ΔP	Pressure drop	
ΔT	Degree of subcooling/superheat	

Subscripts

1	SSLC system
2	Baseline system
iso	Isentropic
ref	Refrigerant
vol	Volumetric
r	Radiation
c	Convection
s	Surface
∞	Quiescent fluid

Chapter 1: Introduction and Literature Review

1.1 Introduction to the Separate Sensible and Latent Cooling Systems

During operation of a conventional air-conditioning (AC) system, two kinds of cooling, i.e., sensible cooling and latent cooling are provided to a conditioned space. The sensible cooling is provided by supplying cold air to reduce the temperature of the conditioned space. The source creating the cold air is the evaporator which is filled with two-phase refrigerant to absorb heat. When the refrigerant temperature in the evaporator is below the dew point of the room air, it causes water vapor in moist air to condense on the evaporator and therefore reduces the humidity ratio of air. The drier air removes the latent load in the space. Figure 1 shows a psychrometric process where point B refers to the dew point of room air and point D refers to supply air.

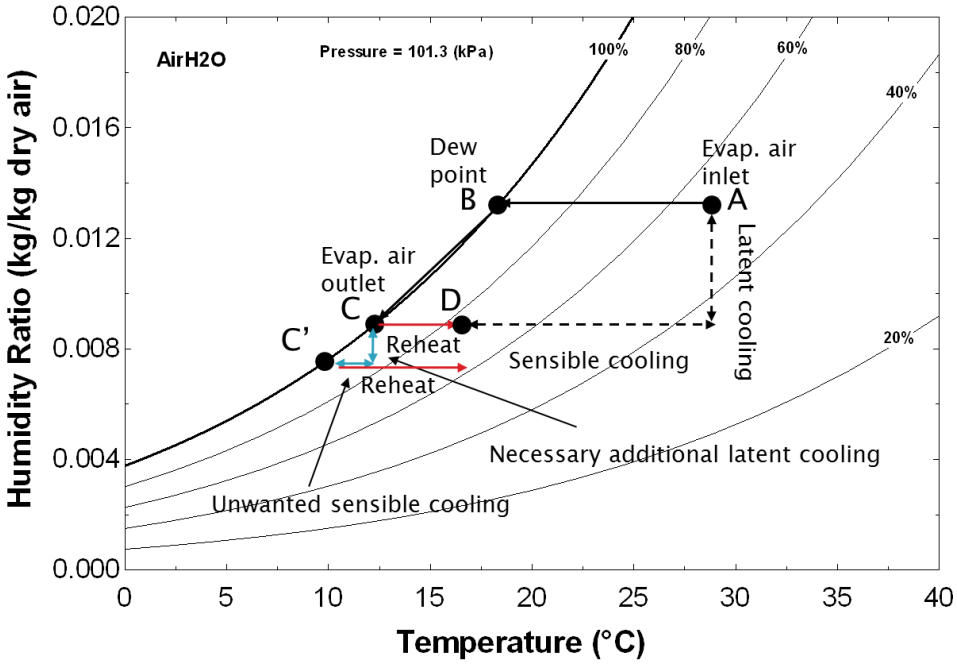

Figure 1: Psychrometric process of conventional AC operation.

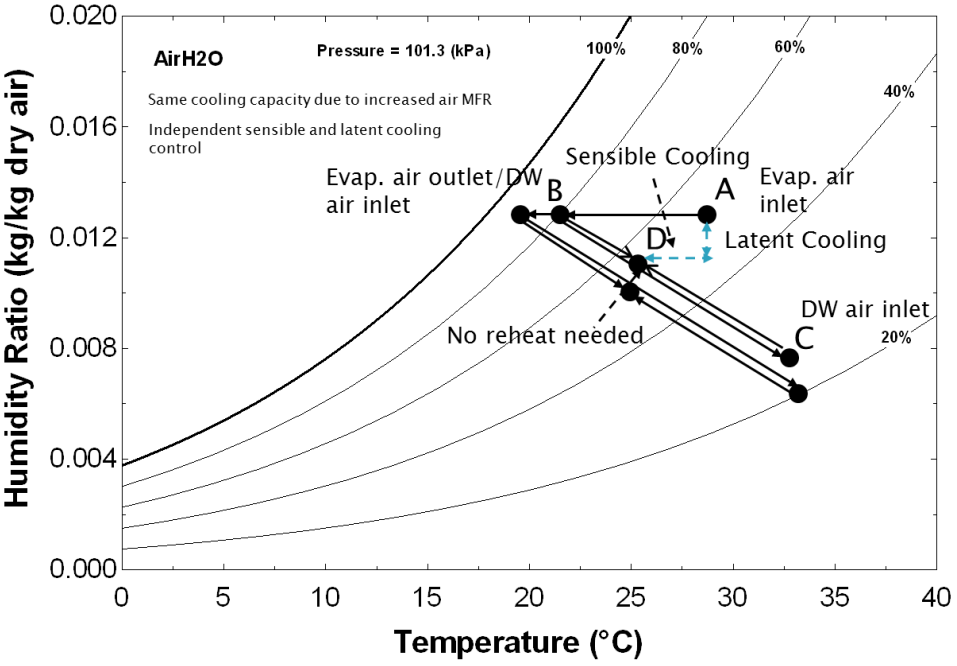

Figure 2: Psychrometric process of one kind of SSLC system (VCS + DW)

There are two limitations related to the operation of conventional AC systems:

- Reheat process reduces system COP

Theoretically, the process of supply air flowing through the evaporator follows the path that is composed of a horizontal sensible load removal part (point A to point B) and a latent load removal part along the100% relative humidity (RH) line from B to C. Usually, the temperature of point C is too low for thermal comfort, therefore a reheat process, typically adopted in commercial buildings, is added to increase the temperature of point C to the temperature of point D. The reheat process, usually carried out by electric heaters, requires extra energy input and increases the total net energy input. Hence, the reheat process reduces the COP.

$$\text{COP} = \frac{\text{useful refrigerating effect}}{\text{net energy input}}$$ (McQuinston, 2005)

- Conventional AC systems lack the independent control of sensible and latent cooling

The reheat process in conventional systems is in fact caused by the lack of independent control of sensible and latent cooling. The path from point B to point C along the 100% RH line reveals that the amount of latent cooling and the amount of sensible cooling are co-dependent to each other and relevant to the slope of the 100% RH line. That is to say, removing a certain amount of water vapor requires an accompanying ratio of temperature reduction. Therefore, the more the latent cooling, the more likely leads to sensible over-cooling. Such a dependent relationship not only costs a reheat stage but also causes a control issue in a conventional AC systems' operation. For example, when more people enter the room, extra latent cooling (the vertical blue arrow pointing downward) is required. The supply air point moves downwards to point C'. Meanwhile, an unnecessary amount of sensible cooling (the

horizontal blue arrow pointing leftward) has to be added to the room as well. This requires more reheat power input to increase temperature for thermal comfort and further reduces the COP.

In order to overcome the two limitations of conventional systems, separate sensible and latent cooling (SSLC) systems are hereby proposed as a solution. Figure 2 plots the psychrometric process of one kind of SSLC systems, which consists of one VCS and one solid desiccant wheel (DW). The VCS provides only sensible cooling (point A to point B) required by the conditioned space at both elevated air temperature leaving the evaporator (point B in Figure 2 vs. point C in Figure 1) and a higher air mass flow rate (MFR). The reason for a higher air MFR requirement is to compensate for the reduced enthalpy difference of air across the evaporator, and to maintain the capacity of sensible cooling. Since the VCS operates above the dew point temperature of air and cannot provide latent cooling, the DW is used to reduce the water vapor content in the part of the air leaving from the sensible evaporator. The part of the dry air from the DW mixes with the rest of the air from the evaporator and is delivered to the conditioned space (point D).

DWs absorb water vapor in air and provide latent cooling; but they generate heat of adsorption during the process and increase the dry air temperature. Theoretically, the amount of latent cooling is equal to the amount of sensible heat generation. Hence the operation of DWs follows an isenthalpic line, which is from point B to point C in Figure 2.

SSLC systems have two features during their operations:

- No reheat process is needed

Since the VCS used in an SSLC system operates above the dew point temperature, the supply air temperature (see point D in Figure 2) is thermally comfortable enough to be sent to the conditioned room directly. No reheat is necessary in SSLC systems.

- Independent control on sensible and latent cooling

An SSLC system uses a VCS to provide sensible cooling. In consequence, any fluctuations of sensible cooling demand can be simply met by changing the capacity of the VCS. The control method to deal with the fluctuations of latent cooling demand is a little bit more complicated. Of course, the rotation speed of DW can be adjusted to meet the fluctuations of latent cooling demand within a certain range. Any latent cooling demand change beyond the reach of rotation speed adjustment can be met by either increasing the regeneration temperature or increasing the air MFR through a DW. It should be noted that although a DW is a stand-alone device providing latent cooling, any amount of the latent capacity change would theoretically lead to the same amount of change in sensible heat generation. Therefore, the VCS must increase the cooling capacity to cover the extra heat. However, such an increase will not lead to over-cooling because the VCS still operates above the dew point.

1.2 Thermal Comfort of SSLC System

To evaluate the performance of an air-conditioning system, thermal comfort is another important factor need to be considered besides energy consumptions. As an

example, in summer, people can reduce the energy consumption by raising the thermostat reading. However, there is an upper limit for most of people who refuse to raise the thermostat anymore. According to the ASHRAE standard 55, thermal comfort is defined as the condition of mind which expresses satisfaction with the thermal environment and is assessed by subjective evaluation. Although the evaluation is subjective, there are several parameters that are considered to have significant impacts on the occupants. They are air temperature, mean radiation temperature, humidity ratio of air, air velocity, occupant's metabolic rate and clothing insulation. The first four parameters are directly controlled by the AC unit in a conditioned space. To be more specific, it is the indoor unit of the AC unit that controls the air conditions. Therefore, in order to study the thermal comfort of the SSLC system, the research should be focused on the design of indoor unit, i.e., the sensible cycle evaporator.

There are several issues regarding to the sensible evaporator design that need to be addressed in the thesis. How to solve the problem of large air side pressure drop? What is the thermal comfort condition of using sensible evaporators? The first question comes from the requirement of larger amount of air MFR through the sensible heat exchanger in order to compensate the smaller air enthalpy difference than that of a conventional system. To reduce the air side pressure drop, the frontal area of the sensible heat exchanger has to be larger than conventional heat exchanger so that the air velocity can be reduced. Some current products, such as chilled ceiling panels and heated floor systems, utilize large frontal area to provide sensible cooling and heating. The common characteristic of the two systems is that it has a low

temperature difference between the working fluid (refrigerant) and the indoor air. For example the chilled ceiling panels use cold water temperature typically of 16 – 18°C to keep the room air temperature at around 25°C. However, conventional evaporators use refrigerant temperature around 7 – 10°C to keep the same indoor condition. This dissertation introduces a new term called "low ΔT heat exchanger" to describe the improved design of sensible heat exchanger such as chilled ceiling panels. Another benefit of using the low ΔT heat exchanger comes from its capability of providing radiative heat transfer to the occupants. This unique capability helps low ΔT heat exchanger control the mean radiation temperature (MRT). MRT, as mentioned above, is one of the factors affecting occupant's thermal comfort, but it cannot be effectively controlled by convectional systems.

1.3 Literature Review

1.3.1 Literature Review on SSLC Systems

There exist different methods to achieve the separation of the sensible cooling and latent cooling. Ling et al. (2009) proposed the most straightforward method. Ling's idea was to separate the two forms of cooling by two vapor compression systems. The first system removes sensible load only, while the second system removes both latent load and a small amount of sensible load. Under the standard ambient conditions (35°C, 44% relative humidity (RH)), the energy consumption of such an SSLC system was reduced by 30% compared with that of a conventional system, and the savings was reported to be up to 50% under the hot and dry condition (37°C, 15% RH). Although Ling's separation method is straightforward, there are two problems need to be addressed. First the sensible cycle cannot remove the entire sensible load in the system. There is always a small amount of sensible load associated with the process of latent load removal in the latent cycle. Because the energy savings of the SSLC system comes from the high-COP sensible cycle, an incomplete separation means such configuration is not the best option (Ling et al. 2009). Second, an internal heat exchanger is required in the SSLC configuration to recover the cooling from the latent cycle, but the extra cost of the internal heat exchanger was not considered in the paper. More studies were focused on the application of using a vapor compression cycle for sensible load removal and solid/liquid desiccant equipment for latent load removal. Yadav (1995) investigated a hybrid system consisting of a liquid desiccant and a vapor compression system. The objective of the study was to find the best operating condition of such system, and the

conclusion was that either having a low sensible heat factor (SHF) condition or when the ambient humidity ratio was high. The SHF is defined as the ratio of sensible heat over the total heat load. Dai et al. (2001) studied the application of integrating a liquid desiccant device and a vapor compression cycle. The test was conducted under the AHRI standard 210/240 conditions (35°C, 44% RH, AHRI, 2008) and the cooling capacity was 5 kW. The coefficient of performance (COP) of the vapor compression cycle improved from 2.2 to 3.39 because of the assistance from the liquid desiccant. Ma et al. (2006) utilized a similar configuration to a larger scale application. A green building demonstration project in Shanghai required a total 60 kW cooling capacity, and the latent cooling was provided by a liquid desiccant unit powered by waste heat from a heat pump. The sensible heat was removed by two 10 kW adsorption chillers powered by a 150 m^2 solar collector and the heat pump powered by electricity. The performance of this complicated system was evaluated at two different SHFs, 0.7 and 0.58, and the COP's were 44.5% and 73.8%, respectively, higher than a conventional VCS. Other than the energy savings results, no economic analysis was conducted. Similar study was also conducted by Katejanekarn et al. (2008) in Thailand. Dhar and Singh (2001) simulated a hybrid system of a solid desiccant wheel (DW) and a vapor compression cycle. They demonstrated that the hybrid system had maximum energy savings under hot and dry weather. In hot and humid region, energy savings was still possible but the space latent load should be high. Depending on different desiccant materials, the temperatures of regeneration can vary between 50°C and above 100°C, therefore different heat sources are reported to drive desiccant devices. Jia et al. (2006) studied the performance of a solid DW using lithium chloride as the adsorbent.

The temperature required to regenerate the wheel was set to be 100°C, and one regeneration heater was used as a heat source. Ghali (2008) numerically simulated a hybrid system in the ambient conditions of Beirut. The main feature of this hybrid system was that the regenerative heat needed by the desiccant wheel was partly supplied by the condenser dissipated heat while the rest was supplied by an auxiliary gas heater. The hybrid air conditioning system was compared with a 23 kW vapor compression unit for a typical office in Beirut characterized by a high latent load. The size of the vapor compression subsystem was reduced to 15 kW at the peak load when the regeneration temperature was fixed at 75 °C. Also the sensible heat ratio of the combined hybrid system increased from 0.47 to 0.73. The paper also conducted a preliminary economic analysis. The annual running costs savings for the hybrid system was 418.39 USD for a gas cost price of 0.141 USD/kg. The payback period of the hybrid system was less than five years when the initial cost of the hybrid air conditioning system priced an additional 1712.00 USD. Hence, for a 20-year life cycle, the life cycle savings of the hybrid air conditioning system were 4,295.19 USD. Casas and Schmitz (2004) studied the integration of a DW and a cooling, heating, and power (CHP) unit. In their study, the waste heat from the CHP unit could be utilized for lithium chloride regeneration. However, the regeneration temperature was only in the range between 50°C and 60°C. The difference in regeneration temperatures in these works may be caused by different dehumidification requirements. Besides lithium chloride, silica gel is another widely accepted candidate for desiccant material, and its regeneration temperature is usually higher than 70°C (Neti, 2000). Different energy efficiency evaluation method was

also reported in literature. Exergy analysis of a solar driven hybrid system was investigated by Ahmed et al. (1998). They compared the performance of the hybrid system operated at different ambient conditions and different mass flow rates through the desiccant wheel. The conclusion was that the maximum irreversibility was generated at an ambient vapor pressure of 3.33 kPa and a desiccant mass flow rate of 5 kg $hr^{-1}m^{-2}$.

1.3.2 Literature Review on Thermal Comfort Standards

In 2004, ASHRAE released the standard 55-2004, Thermal Environmental Conditions for Human Occupancy, to specify the combinations of indoor thermal environmental factors and personal factors that will produce thermal environmental conditions acceptable to a majority of the occupants within the space. A PMV index, predicted mean vote, is used to measure a large group of persons' thermal sensation on a seven-level scale which uses +3 to be hot and -3 to be cold.

Table **1** lists the detail definition of the PMV. The seven-level scale is usually enough to describe the thermal sensation in building applications, however higher numbers than 3 and lower numbers than -3 are also found in some literature to describe thermal sensation in extreme conditions, such as the cabin of a car parking in direct sunlight in summer for a long time.

Table 1: Thermal sensation based on PMV scale

PMV scale	Thermal sensation
+3	hot
+2	warm
+1	slightly warm
0	neutral
-1	slightly cool
-2	cool
-3	cold

Six primary factors, which are metabolic rate, clothing insulation, air temperature, radiant temperature, air speed and humidity, are included in the standard when defining conditions for thermal comfort. Besides the primary factors, there are a number of other secondary factors affecting comfort in some circumstances. Figure 3 plots two thermal comfort zones on a psychrometric chart. Compared with other conventional psychrometric chart, the x-axis in the figure represents operative temperatures instead of dry-bulb temperatures. It is because the operative temperature takes both the dry-bulb temperature and the radiant temperature into consideration. The operative temperature can be calculated from Eq. (1). Two different thermal comfort zones are plotted for summer and winter because clothing insulation is

different. The boundaries of these two zones are determined by using Eq. (2) and Eq. (3), which calculate the maximum and minimum operative temperature ranges of the comfort zones. There is no unanimous agreement on what should be the low side comfort range of humidity, but ASHRAE suggests it should be higher than 2 gkg^{-1} dry air. Air speeds greater than 0.2 ms^{-1} (40 $ftmin^{-1}$) may be used to increase the upper operative temperature limit for the comfort zone in certain circumstances

$$t_o=\frac{h_r\bar{t}_r+h_c t_a}{h_r+h_c} \quad (1)$$

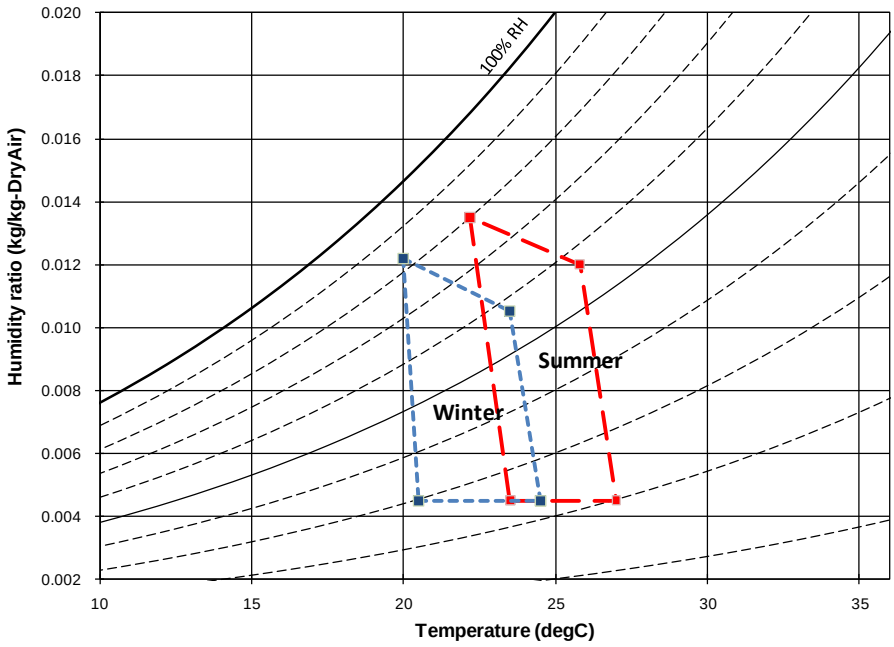

Figure 3: ASHRAE thermal comfort zones for winter and summer

$$T_{min,Icl}=[(I_{cl}\text{-}0.5\ clo)T_{min,1.0clo}+(1.0clo\text{-}I_{cl}T_{min,0.5clo}]/0.5\ clo \quad (2)$$

$$T_{max,Icl}=[(I_{cl}-0.5\ clo)T_{max,1.0clo}+(1.0clo-I_{cl})T_{min,0.5clo}]/0.5\ clo \quad (3)$$

where

$T_{max,Icl}$ is the upper operative temperature limit for clothing insulation I_{cl}

$T_{min,Icl}$ is the lower operative temperature limit for clothing insulation I_{cl}

I_{cl} is the thermal insulation of the clothing in question (clo)

Besides ASHRAE Standard 55-2004, International Standards Organization (ISO) has also established a set of standards to address the thermal comfort issue. ISO standard 7730: 2005, Ergonomics of the thermal environment—Analytical determination and interpretation of thermal comfort using calculation of the PMV and PPD indices and local thermal comfort criteria, describes the PMV (Predicted Mean Vote) and PPD (Predicted Percentage Dissatisfied) indices and specifies acceptable conditions for thermal comfort. ISO 8996:2004, Ergonomics of the thermal environment—Determination of metabolic rate, describes six methods for estimating metabolic heat production, which are divided into three levels according to accuracy. ISO 9920:2007, Ergonomics of the thermal environment—Estimation of thermal insulation and water vapor resistance of a clothing ensemble, provides an extensive database of the thermal properties of clothing and garments. The properties are based upon measurements on heated manikins where basic (or intrinsic) thermal insulation is measured as well as vapor permeation properties of garments and ensembles.

Since most vehicles have a HVAC system to control the thermal environment of the cabin, thermal comfort is also extensively studied by automotive thermal engineers. Compared to the building thermal load, 50 per cent of the automotive

thermal load is due to the solar heat gain (Shimizu et al. 1983). Radiative heat exchange can account for up to 70 per cent of the global sensible heat exchange between human and environment. However, the most significant difference between the field of building thermal comfort study and automotive thermal comfort is how to model the human body. For building thermal comfort modeling, Fanger (1967) proposed a single comfort equation to express thermal comfort of occupants exposed to constant conditions at constant metabolic rate for a long/sufficient period of time and such effort is later included into ASHRAE and ISO standards. However, considering the fact that solar radiation always varies during driving, automotive thermal comfort should be categorized to a dynamic boundary condition problem. The other difference is the volume of the cabin is much smaller to a space in the building, which makes the air flow field in the cabin extremely non-uniform. For example, air velocity can be largest at the outlet of air vents but almost be zero at passengers' backs due to the direct contact with the seat. Because of the non-uniformity and transient nature of automotive thermal comfort problems, automotive engineers have been working on developing detailed human body models to address the transient and non-uniform nature of automotive thermal comfort. The operative temperature is usually replaced by equivalent temperature or other more advanced physiology model to better capture thermal sensation of passengers in the cabin. Figure 4 describes the flow chart of automotive thermal comfort evaluation.

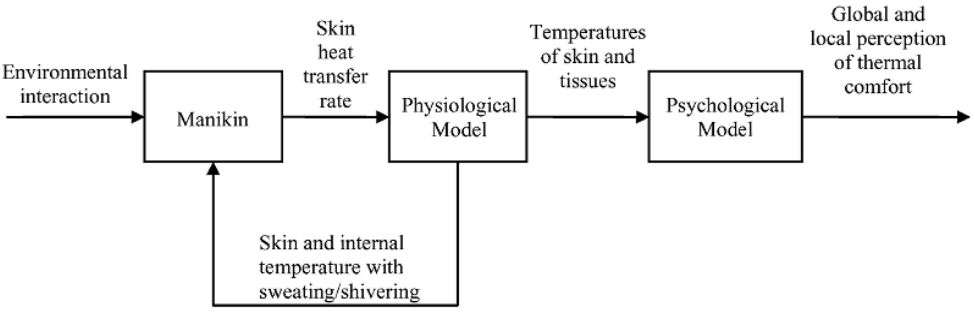

Figure 4: Block diagram for evaluating the perception of human thermal comfort (Source: Walgama et al. 2006)

Olesen et al. (1988) was among the first to develop a detail human body model for better physiology (skin temperature) measurement. Table 2 shows the 16-segment manikin model as well as the surface areas results. The paper also studied five different clothing ensembles with the same total thermal insulation, but very different distributions of the insulation on the body in experiments with 16 sedentary subjects. The asymmetry was ranging from unclothed upper part to unclothed lower part of the body. Their experimental study provides a method for quantifying the non-uniformity of a clothing ensemble and examines how it influences local thermal discomfort.

Table 2: Thermal manikin: main dimensions and skin areas of the 16 segments (Source: Olesen et al. (1988))

Body segments	Segment number	Surface area [m^2]	Fraction of total body surface area [%]	
Left foot	1	0.062	3.5	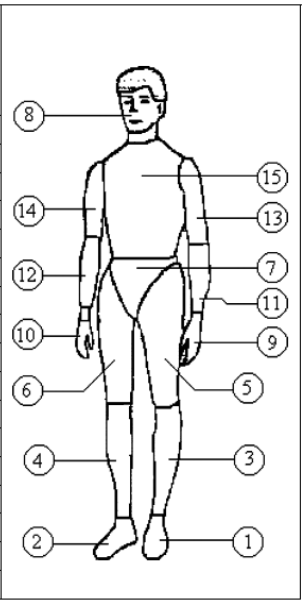
Right foot	2	0.062	3.5	
Left fibula	3	0.140	8.0	
Right fibula	4	0.140	8.0	
Left thigh	5	0.160	9.1	
Right thigh	6	0.160	9.1	
Pelvis	7	0.080	4.6	
Head	8	0.180	10.4	
Left hand	9	0.050	2.9	
Right hand	10	0.050	2.9	
Left forearm	11	0.062	3.5	
Right forearm	12	0.062	3.5	
Left upperarm	13	0.077	4.4	
Right upperarm	14	0.077	4.4	
Chest	15	0.185	10.6	
Back	16	0.204	11.7	
The whole body		1.751	100.0	

Tanabe et al. (1994) later added sensible and latent heat exchange between each part of the body and the environment. The 16-segment body used in the paper was a female manikin and the total surface area of the body was therefore smaller than Olesen's model. In order to better address the thermal comfort of a person in a non-uniform condition such as car cabin, the paper used an equivalent temperature (t_{eq}), which was defined as the temperature of a uniform enclosure in which a thermal manikin with realistic skin surface temperatures would lose heat at the same rate as it would in the actual environment, to calculate PMV. The idea of equivalent temperature has been widely accepted in automotive thermal comfort calculation.

Han et al. (2001) also used a 16-segment male manikin model and improved the model by dividing each segment into four body layers (core, muscle, fat and skin tissues) and a clothing layer. The improved model had the ability to predict local thermal comfort level of an occupant in a highly non-uniform thermal environment,

and formulated the thermal comfort as a function of air velocity, humidity, direct solar flux, as well as the level of activity and clothing type of each individual. The author also emphasized the use of equivalent homogeneous temperature (EHT), which is similar to t_{eq} in Tanabe's work, to quantify thermal comfort in the non-homogeneous (non-uniform) area. Kaynakli et al (2005) used Olesen's manikin model but was focused on thermal comfort of passengers during vehicle's initial warm-up and cooling period. In early minutes of warm-up, heat loss from body to environment is very high due to low inside air and surface temperatures. The average skin temperature of the body and contact temperature of hand with steering wheel were reported to fall to 32°C and 17.5°C, respectively. The thermal sensation (TS) was recorded as low as - 4.5 which was in the range between very cold and painfully cold and became neutral in 12 minutes. Opposite to the warm-up period, the TS starts from a very high value of 8 due to large sensible heat exchange between body and high temperature cabin. It takes almost 30 minutes to reach TS neutral.

Walgama et al. (2006) presented a comprehensive survey of research studies regarding automotive thermal comfort. The work was classified according to whether it is concerned with the passenger compartment environment or the condition of the passengers and their interaction with the compartment. The review included factors associated with passenger compartment conditions, such as flow field and temperature field, which affect the thermal comfort of the occupants. The evolution of thermal comfort models was reviewed. Also included were various computational and empirical models for predicting physiological response and the sensation of thermal comfort in the non-uniform transient environment of a vehicle.

1.3.3 Literature Review on Natural Convection and Its Enhancement

Natural convection refers to the motion of a flow is driven simply by the interaction of a difference in density in a gravitational field. The driving force of such density difference is a temperature difference, as in atmospheric and oceanic circulations, or in the air current arising from a cooling object. It may also be due to variation in composition or phase of a fluid, such as in most air rising. Natural convection is quite a different transport process compared with forced convection. The flow and temperature fields are invariably completely coupled and must be considered together. The flows are relatively weak, because the velocities are always relatively small and the inertial and viscous effects of momentum transport are usually of the same order.

The basic equations of natural convection are continuity, momentum and energy equations, which are listed as Eq. (4) through Eq. (6) (Gebhart, 1971). The $\ddot{q}$ in the energy equation represents the source term over volume, and the Φ represents the dissipation term.

$$\frac{\partial \rho}{\partial \tau}+\nabla\cdot\left(\partial\vec{V}\right)=0 \tag{4}$$

$$\rho\frac{D\vec{V}}{D\tau}=\rho\left[\frac{\partial\vec{V}}{\partial\tau}+\left(\vec{V}\cdot\nabla\right)\vec{V}\right]=\rho\vec{g}-\nabla p+\mu\nabla^2\vec{V}+\frac{\mu}{3}\nabla(\nabla\cdot\vec{V}) \tag{5}$$

$$\rho\frac{De}{D\tau}=\rho\left[\frac{\partial e}{\partial\tau}+\left(\vec{V}\cdot\nabla\right)e\right]=\nabla\cdot k\nabla t+q'''-p\nabla\cdot\vec{V}+\mu\Phi \tag{6}$$

The complexity and coupling inherent in natural convection processes are apparent in this set of equations. Motion results because ρ is subject to change

according to temperature. The density term in equations can only be solved by considering the "temperature" equation. The energy equation, in turn, inevitably involves velocity. Thus, the distributions of ρ, $\vec{V}$, and e in space (x, y, z), and perhaps also in time τ, must be found simultaneously from these governing equations.

In spite of the aforementioned complexity, governing equations are still useful to provide a great amount of information on natural convection problems. Most of the information comes from the simpler forms of the governing equations which are applicable in most physical circumstances. The most widely applied assumption is Boussinesq approximation. It assumes a linear density variation corresponding to temperature in the $\rho\vec{g}$ term (see Eq. (7)) and neglects the density variation in other places.

$$\rho_\infty - \rho = \rho\beta\Delta t = \rho\beta(t - t_\infty) \tag{7}$$

where

ρ is the density

β is the thermal expansion coefficient

t is the temperature

Natural convection problems can be further classified as either external one (free convection) or internal one (natural convection). Ostrach (1964), Ede (1967) and Gebhart (1979) conducted comprehensive reviews on the first problem. The second problem is considerably more complex than external one. This is because at large Rayleigh numbers (see Eq. (8) for definition), classical boundary-layer theory yields the same simplifications for external problems that are so helpful in other fluid-flow

problems, i.e., the region exterior to the boundary layer is unaffected by the boundary layer.

$$Ra=\frac{g\beta}{\nu\alpha}(T_s-T_\infty)x^3 \tag{8}$$

where

Ra is the Rayleigh number

g is the gravitational acceleration

T_s is the surface temperature

T_∞ is the quiescent temperature

v is the kinematic viscosity

α is the thermal diffusivity

β is the thermal expansion coefficient

x is the characteristic length

For confined natural convection, on the other hand, boundary layers form near the walls but the region exterior to them is enclosed by the boundary layers and forms a core region. Because the core is partially or fully encircled by the boundary layers, the core flow is not readily determined from the boundary conditions but depends on the boundary layer, which, in turn, is influenced by the core. The interactions between the boundary layer and core constitute a central problem that the flow pattern cannot be predicted a priori from the given boundary conditions and geometry. In fact the situation is even more intricate because it often appears that more than one global core flow is possible and flow sub-regions, such as cells and layers, may be imbedded in the core (Ostrach 1972, Ostrach 1982, Ostrach and Hantman 1981). Figure 5 shows one kind of widely studied enclosures. It is a square

enclosure with the side length of L. The upper and lower walls (ceiling and floor) are assumed to be well thermally insulated, and the left and right walls are at constant temperatures of T_c and T_h, respectively.

The stability of the natural convection problem is another widely discussed topic in literature. Taking the problem of a horizontal layer of fluid heated from below as an example, Schluter et al. (1965) pointed out that when a horizontal layer of fluid is heated from below, thermal expansion causes a density gradient opposite to the direction of gravity. In cases where the temperature gradient exceeds a certain critical value the static state of the fluid becomes unstable because the buoyancy force is sufficient to overcome the dissipative effects. The resulting cellular convective flow cannot be uniquely determined by the momentum equation and boundary conditions (Schluter et al. (1965)). Malkus and Veronis (1958) showed for special solutions that the degeneracy persists for finite amplitude solutions. They demonstrated that flows with rectangular or hexagonal cell pattern are finite amplitude solutions and that their number is infinite because the ratio of side lengths of a rectangular is a free parameter. Schluter et al. (1965) concluded that the instability of the hexagonal cell pattern was in a range between the critical Rayleigh number and a certain supercritical value. Beyond that, the rolls are stable.

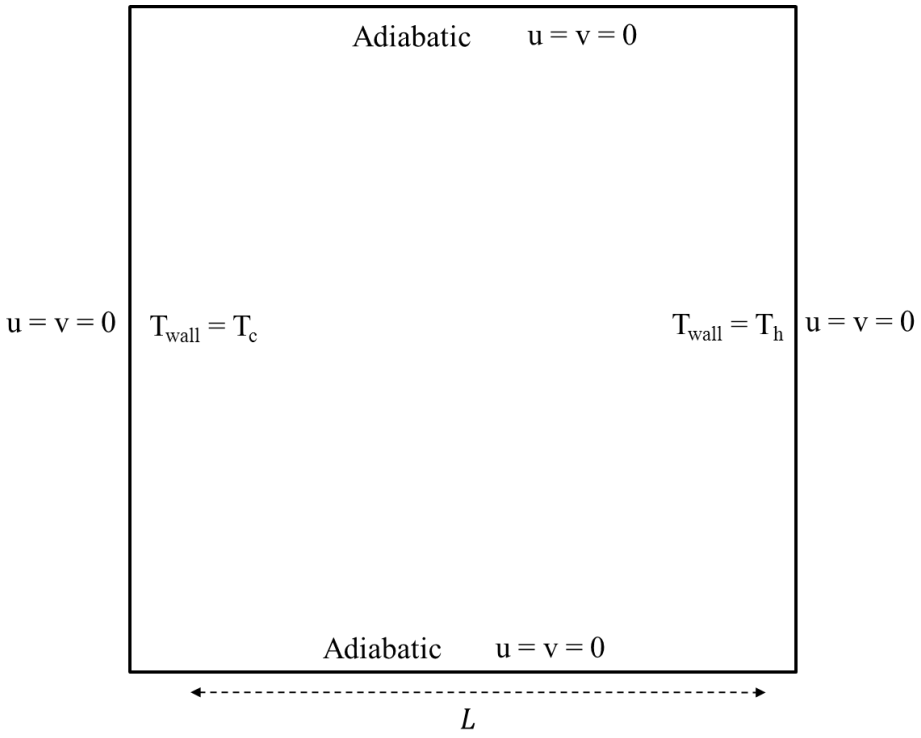

Figure 5: A 2D enclosure with boundary conditions and dimensions for natural convection study

Henkes and Hoogendoorn (1995) presented the governing equations, Eq. (9) through Eq. (14), for turbulent natural convection in an enclosure with simplifications.

2D steady state continuity equation for incompressible flow is:

$$\frac{\partial u}{\partial x}+\frac{\partial v}{\partial y}=0 \tag{9}$$

Momentum equations with Boussinesq assumption are:

$$u\frac{\partial u}{\partial x}+v\frac{\partial u}{\partial y}=-\frac{1}{\rho}\frac{\partial p}{\partial x}+\frac{\partial}{\partial x}(\nu+\nu_t)\left(2\frac{\partial u}{\partial x}\right)+\frac{\partial}{\partial y}(\nu+\nu_t)\left(\frac{\partial u}{\partial y}+\frac{\partial v}{\partial x}\right) \tag{10}$$

$$u\frac{\partial v}{\partial x}+v\frac{\partial v}{\partial y}=-\frac{1}{\rho}\frac{\partial p}{\partial y}+g\beta\left(T-\frac{T_h+T_c}{2}\right)+\frac{\partial}{\partial x}(\nu+\nu_t)\left(\frac{\partial v}{\partial x}+\frac{\partial u}{\partial y}\right)+\frac{\partial}{\partial y}(\nu+\nu_t)\left(2\frac{\partial v}{\partial y}\right) \tag{11}$$

Energy equation is:

$$u\frac{\partial T}{\partial x}+v\frac{\partial T}{\partial y}=\frac{\partial}{\partial x}\left(\frac{\nu}{Pr}+\frac{\nu_t}{\sigma_T}\right)\frac{\partial T}{\partial x}+\frac{\partial}{\partial y}\left(\frac{\nu}{Pr}+\frac{\nu_t}{\sigma_k}\right)\left(\frac{\partial T}{\partial y}\right) \tag{12}$$

Turbulent kinetic energy equation (k-ε model) is:

$$u\frac{\partial k}{\partial x}+v\frac{\partial k}{\partial y}=\frac{\partial}{\partial x}\left(\nu+\frac{\nu_t}{\sigma_k}\right)\frac{\partial k}{\partial x}+\frac{\partial}{\partial y}\left(\nu+\frac{\nu_t}{\sigma_k}\right)\left(\frac{\partial k}{\partial y}\right)+P_k+G_k-\epsilon \tag{13}$$

Turbulent dissipation equation (k-ε model) is:

$$u\frac{\partial \epsilon}{\partial x}+v\frac{\partial \epsilon}{\partial y}=\frac{\partial}{\partial x}\left(\nu+\frac{\nu_t}{\sigma_\epsilon}\right)\frac{\partial \epsilon}{\partial x}+\frac{\partial}{\partial y}\left(\nu+\frac{\nu_t}{\sigma_\epsilon}\right)\left(\frac{\partial \epsilon}{\partial y}\right)+[C_{\epsilon 1}(P_k+c_{\epsilon 3}G_k)-c_{\epsilon 2}\epsilon]\left(\frac{\epsilon}{k}\right) \tag{14}$$

with

$$P_k=\nu_t\left[2\left(\frac{\partial u}{\partial x}\right)^2+2\left(\frac{\partial v}{\partial y}\right)^2+\left(\frac{\partial u}{\partial y}+\frac{\partial v}{\partial x}\right)^2\right]$$

$$G_k=-\frac{\nu_t}{\sigma_T}g\beta\frac{\partial T}{\partial y}, \qquad \nu_t=c_\mu\frac{k^2}{\epsilon}$$

de Vahl Davis (1968) was probably among the first who studied the natural convection problem in an enclosure, although he only considered the problem in two conditions and both of them were limited in the laminar region. One condition was natural convection in a square enclosure with the Rayleigh number of 2×10^5 and the other was natural convection in a rectangular enclosure (aspect ratio of 5) with the Rayleigh number of 1.25×10^6.

Cormack et al. (1974) extended the geometry of the enclosure to any small aspect ratio which was defined as the width of the enclosure should be at least 12 times larger than the height. The walls of the enclosure were heated differentially. One analytic solution in terms of an asymptotic expression for the Nusselt number was presented in the study. The streamline profile was also plotted and it demonstrated that there were two regimes: a parallel flow in the core region and a second, non-parallel flow near the ends of the enclosure.

Ostrach. (1988) provided a wide review on previous natural convection problem. It covered different geometries of enclosures including cylinders, rectangular enclosures of large aspect ratio and rectangular enclosures of small aspect ratio. As being pointed out in the conclusion, earlier research focused on searching analytical or experimental solutions. However, there was an ever-increasing proliferation of numerical solutions to such problems with more complications.

Henkes and Hoogendoorn (1995) reported the outcomes of a workshop on turbulent natural convection in enclosures. The problem was defined as: a 2D square enclosure whose side length is unit with hot left and cold right vertical walls and adiabatic horizontal walls. Air with $Pr = 0.71$, assuming a Boussinesq fluid, at $Ra = 5\times10^{10}$. All the participants solved the problem by different CFD software packages. Their results were compared and numerical accuracies were reported against each other.

Aounallah et al. (2005) used a commercial CFD software package, Fluent, to solve the similar problem as Henkes and Hoogendoorn but at a smaller Rayleigh number of 1.58×10^{9}. Three different mesh grids, 100×100, 120×120 and 200×200,

were studied but no significant improvement of accuracy were reported by refining the grid. K-ω SST model was adopted to solve the turbulent equations. Both temperature and stream function field were very similar to the results of Henkes and Hoogendoorn's work. One of the paper's contributions was development of a reduced order correlation of the heat flux at the hot wall in terms of the normalized Nusselt number.

Besides 2D convection problems, Sigey et al. (2004) studied a three dimensional enclosure in the form of a rectangular enclosure containing a conventional heater built into one wall and having a window in the same wall. In this problem, the Rayleigh number was varied from 5×10^{10} to 5×10^{11}. Temperature stratification was reported in the paper: The room was stratified into three regions, a cold upper region, a hot region in the confluence of the hot and cold streams and a warm lower region. The results also showed that the location of the heater, as well as the size of the window, has an important influence on the overall heat transfer through the room.

Ogut. (2009) used water-based nanofuids as the working fluid in an inclined square enclosure. The enclosure was heated at a constant heat flux on the left wall and cooled on the right. The floor and ceiling were kept adiabatic. Five types of particles were taken into consideration: Cu, Ag, CuO, Al_2O_3, and TiO_2. Polynomial differential quadrature (PDQ) method was applied to solve the governing Equations. A parametric study was performed for inclination angles from 0° to 90°. It was found that nano-particles increased the average heat transfer rate, and the largest

improvement (63.9%) came from using Ag at a concentration of 20% volume fraction.

Instead of applying an adiabatic-wall assumption, a further effort was made to make the wall assumption more realistic. Liaqat and Baytas (2001) studied a square enclosure with constant wall temperature and finite conductive properties. The space was filled with a Bousinessq fluid with a Prandtl number of 7.0 containing a uniform volumetric heat source. Control volume method was applied and the SIMPLER algorithm (Patankar, 1980) was utilized to handle the pressure and velocity coupling of governing equations. Isotherms and streamlines (in normalized form) obtained from the study are plotted in

Figure 6.

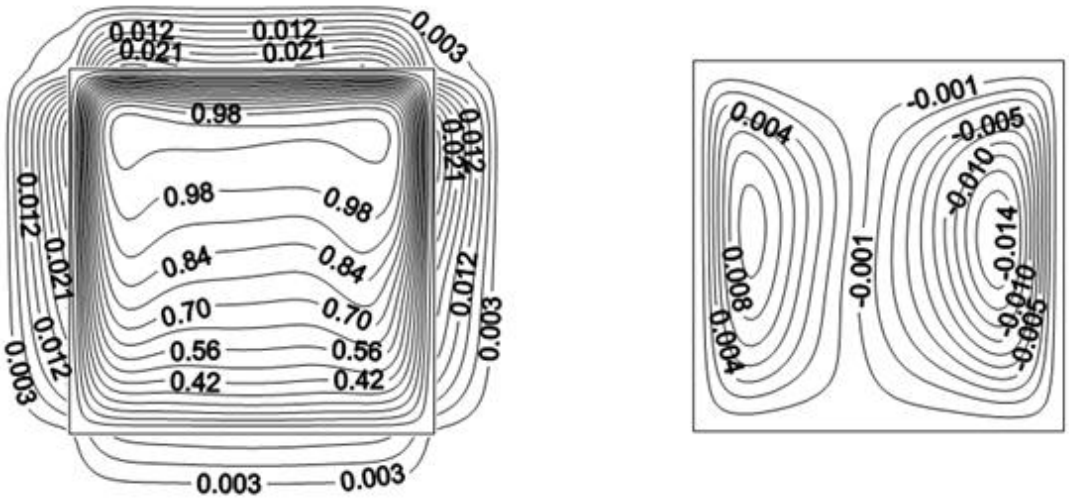

Figure 6: Isotherms and streamlines for $Ra = 10^7$, stainless steel walls

(Source: Liaqat et.al (2001))

Sharma et al. (2007) added radiation into the natural convection problem. The conjugate turbulent natural convection problem was also defined in a rectangular

enclosure filled with air, and the walls were of finite thickness t_w and finite conductivity k_w. The floor of the enclosure was maintained at a constant temperature t_h, and its external surface was exposed to ambient temperature at t_c. K-ε model was applied to solve the turbulent problem. A correlation, Eq. (16), was developed to predict the overall heat transfer rate in terms of the Nusselt number (see Eq. (15) for definition):

$$Nu = \frac{hL}{k_f} \tag{15}$$

where

L is the characteristic length

k_f is the thermal conductivity of the fluid

h is the convective heat transfer coefficient

$$Nu_c = 0.152 AR^{0.267} Ra^{0.34} \tag{16}$$

where

AR is the aspect ratio varied from 0.5 to 2.0, and the Rayleigh number is from 10^8 to 10^{12}.

Bouali et al. (2005) also considered radiation and applied his model into an inclined rectangular enclosure. From the comparison shown in Figure 7, it was found that radiation improved the heat transfer in the enclosure.

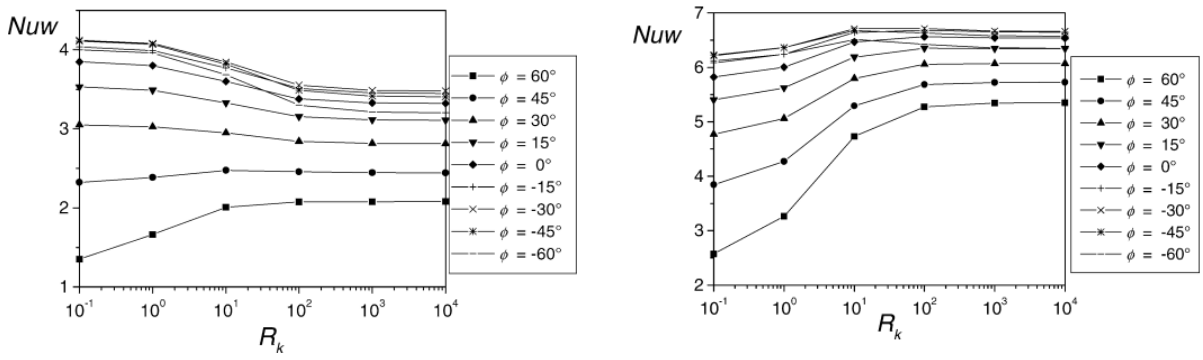

Figure 7: Comparison of the Nusselt number in the enclosure with (right) and without radiation (Source: Bouali et al. (2005))

Ben-Nakhi and Chamkha (2007) added an inclined thin heated fin into the square enclosure (Figure 8). Surprisingly, rather than improving the heat transfer, the existence of the fin reduces the average Nusselt number. Two reasons were given: restraining natural convection and increasing heating surface.

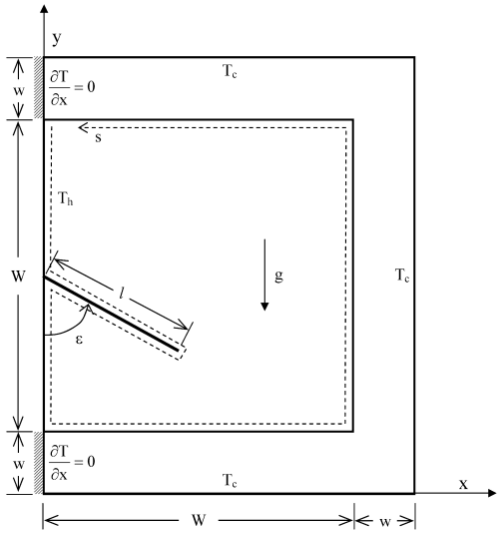

Figure 8: Schematic diagram and coordinate system for a square enclosure with inclined fin at the center of the hot wall (Source: Ben-Nakhi et al. (2007))

Cuckovic-Dzodzo (1999) complicated the enclosure problem by partitions which separated the enclosure into three parts. (Figure 9)

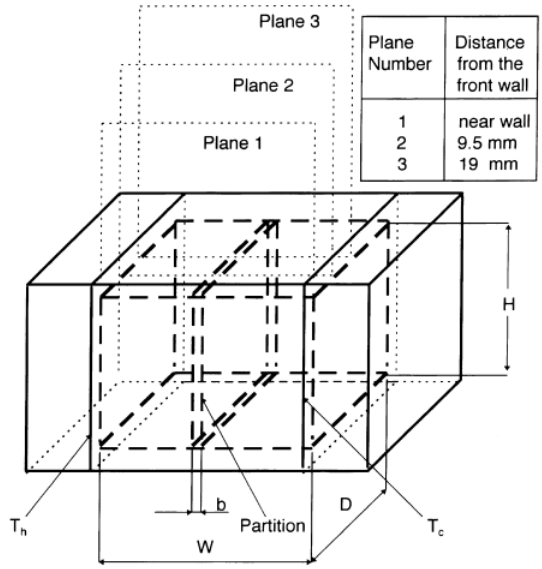

Figure 9: Schematic diagram of an enclosure with partition (Source: Cuckovic-Dzodzo et al. (1999))

The isotherms and streamlines of the problem with the Rayleigh number of 2.6×10^5 were plotted as shown in Figure 10.

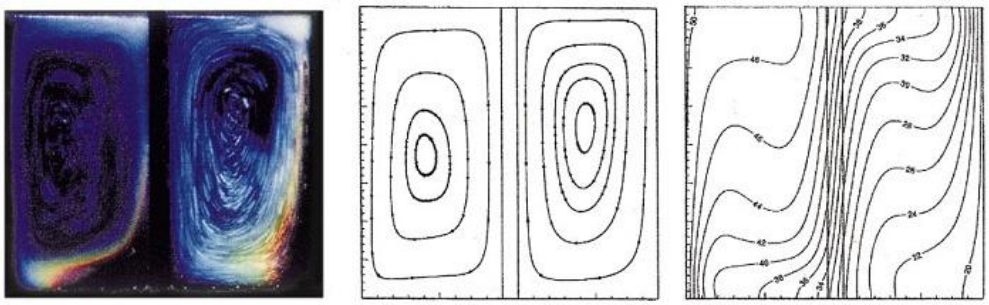

Figure 10: Streamlines and isotherms of the partitioned enclosure (Left two are streamlines and the right one is isotherms) (Source: Cuckovic-Dzodzo et al. (1999))

Because natural convection has a lower heat exchange rate compared with forced convection, many researchers have been working on the exploration of natural convection enhancement methods. The addition of different configurations of fin and active oscillators are two most widely reported practices. Both practices aim to disturb the growth of thermal boundary layer and promote effective heat transfer.

Frederick (2006) numerically studied the enhancement of natural convection by placing a thick vertical fin in the middle of a differentially heated cubical enclosure. He focused on investigating the variation of the Nusselt number with different Rayleigh numbers and thermal conductivity ratios. A main circulation and a flow restriction were observed but they were only significant at low Rayleigh numbers. A secondary circulation cell was reported at high thermal conductivity ratios. Long fins were found to be more effective in promoting heat transfer. Fujii (2007) studied the effect of the inclination angle of a finned surface to enhance natural convection. The fins were constructed on a 250 mm × 240 mm × 3 mm aluminum base plate. The angle of air flow through these fins changed from 30° to 90°. It was concluded that the enhancement was most significant at 60°. At this angle, the convective heat transfer rate was 19% higher than that of a vertical finned surface. A correlation of the Nusselt number and inclination angle was also obtained. Instead of vertically placed fins, Dialameh (2008) investigated the fluid flow and heat transfer through horizontal rectangular thick fin arrays. The lengths of these fins are under 50mm. Results showed that there were two types of flow depending on the ratio of height to length. If the ratio is smaller than 0.24, the air can only enter into the channel from fin end regions. However, the air flow can also enter into the middle parts of the fins if the ratio is greater than 0.24. With regards to the enhancement of natural convection, the natural convection heat transfer coefficient (HTC) increases with the fin spacing and the temperature difference, but decreases with the fin length. It was reported that the fin thickness and fin height did not affect the HTC considerably. Two correlations (Eq. (17) and Eq. (18)) were proposed to predict the

average Nusselt number of an array of fins based on the Rayleigh number, the ratio of fin height and fin length, the ratio of fin spacing and fin length and the ratio of fin height and fin thickness.

$$Nu_s=0.625(Ra)^{0.2382}\left(\frac{H}{L}\right)^{0.3674}\left(\frac{S}{H}\right)^{0.3303}\left(\frac{H}{t}\right)^{-0.0504} \quad \text{for } Ra < 1500 \quad (17)$$

$$Nu_s=0.5007(Ra)^{0.2828}\left(\frac{H}{L}\right)^{0.4468}\left(\frac{S}{H}\right)^{0.3901}\left(\frac{H}{t}\right)^{-0.083} \quad \text{for } Ra > 1500 \quad (18)$$

Heindel et al. (1995) investigated the single phase natural convection enhancement by a discrete heat source with parallel plate fin arrays. Compared to unfinned conditions, the parallel plate fin arrays provided 24 and 15 times more heat flux for vertical and horizontal cavity orientation, respectively. Horizontal orientation was more favored because it generated nearly uniform heat transfer from the source. A porous medium model was also developed to simulate fluid flow and heat transfer from a dense array of parallel plate fins mounted to on wall of a vertical cavity. Fluid penetration and heat transfer was found to increase within the porous regions as the applied power (modified Rayleigh number) increased. Numerical predictions were in reasonable agreement with experimental results for the vertical orientation, with the Brinkman-Forchheimer-extended Darcy model following the data more closely than the Brinkman extended Darcy model. AlEssa et al. (2008) numerically examined the heat transfer enhancement from a horizontal rectangular fin embedded with triangular perforations under natural convection (see Figure 11). The fin's heat dissipation rate was compared to that of an equivalent solid one. Several conclusions were drawn:

i) The temperature drop along the perforated fin length is consistently larger than that on an equivalent non-perforated fin.

ii) For certain values of triangular dimensions, the perforated fin can enhance heat transfer. The magnitude of enhancement is proportional to the fin thickness and its thermal conductivity.

iii) The extent of the heat dissipation rate enhancement for perforated fins is a complicated function of the fin dimensions, the perforation geometry and the fin thermophysical properties.

iv) The gain in the heat dissipation rate for the perforated fin is a strong function of both the perforation diameter and lateral spacing. This function attains a maximum value at a given perforation diameter and spacing, which are called the optimum perforation dimension b_o, and the optimum spacing S_{yo}, respectively.

v) The perforation of fins enhances the heat dissipation rates and at the same time decreases the expenditure for fin materials.

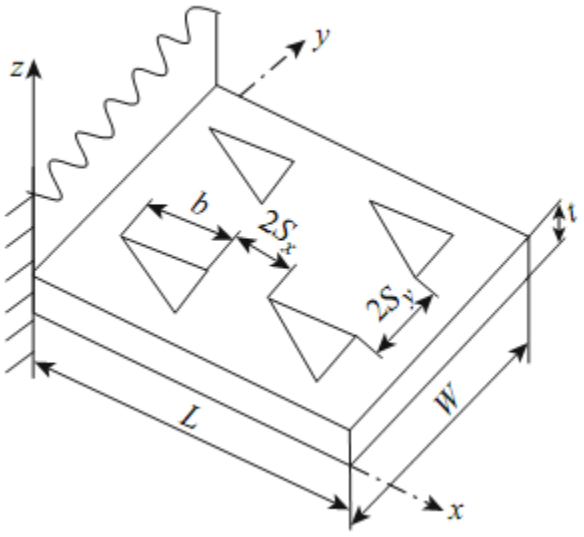

Figure 11: Fin with equilateral triangular perforations to enhance natural convection (Source: AlEssa et al. (2008))

Van Lear and Sparrow (2010) developed a numerical simulation code to study an active enhancement device for natural convection in the interfin spaces of a fin array (see Figure 12). A baseline solution for the non-enhanced situation revealed that the confinement created by the walls of adjacent fins and the base surface contributed to a drastic reduction of the HTC values compared with those for the standard vertical plate. Enhancement was achieved by alternately introducing and extracting air into and from the space. The frequency of introduction/extraction cycle was varied over values of 0, 10, 50 and 100 Hz. Even at a low oscillation frequency of 10 Hz, the interfin HTCs were significantly enhanced but not sufficiently to overcome the confinement effect. At 100 Hz, the enhancement gave rise to coefficient values that about 64 times greater than the unenhanced values.

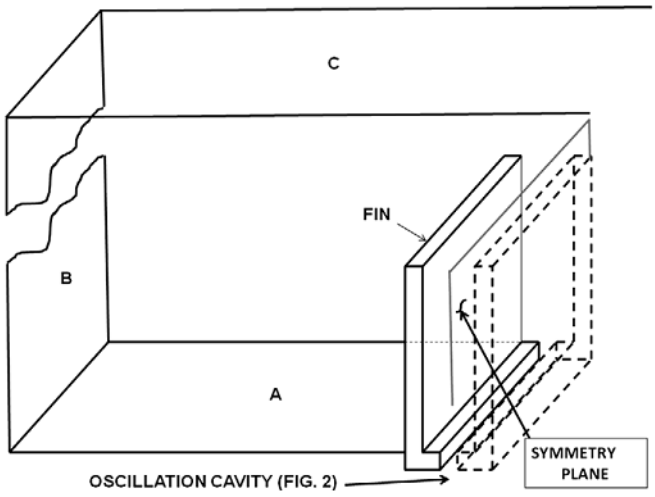

Figure 12: Schematic diagram of the physical system (Source: Van Lear and Sparrow (2010))

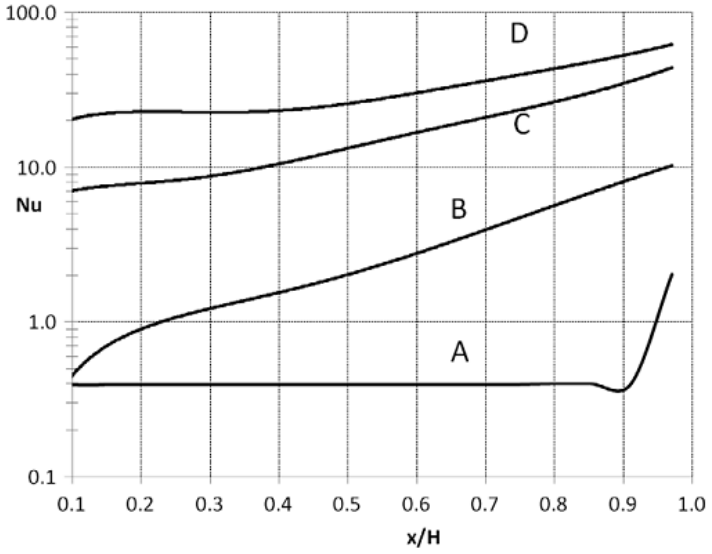

Figure 13: Local cycle-averaged Nusselt number results for the surface of the fin facing the neighboring fin. Curve designation: (A) baseline, no oscillation, (B) 10 Hz, (C) 50 Hz and (D) 100 Hz. (Source: Van Lear and Sparrow (2010))

Tsuji et.al (2007) conducted an experimental study (Figure 14) on heat transfer enhancement for a turbulent natural convection boundary layer in air along a vertical flat plate by inserting a long flat plate in the span-wise direction (simple heat transfer promoter) and a short flat plate aligned in the span-wise direction (split heat transfer promoter) with clearance into the near-wall region of the boundary layer. For the simple heat promoter, the HTC increases by a peak value of approximately 37% in the downstream region of the promoter compared with those in the usual turbulent natural convection boundary layer. For the split heat transfer promoter, the enhancement was approximately 60% in the downstream region of the promoter.

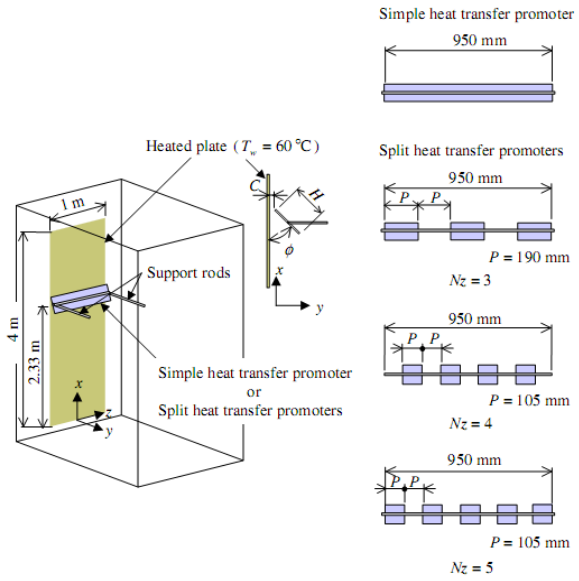

Figure 14: Experimental apparatus, simple heat transfer promoter and split heat transfer promoters (Source: Tsuji et al. (2007))

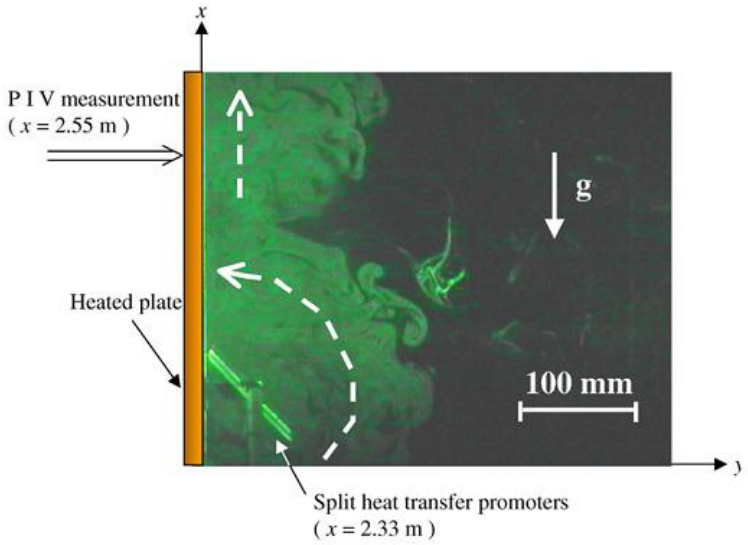

Figure 15: Visualized fluid motions in the downstream region of a split heat transfer promoter (*x*-*y* plane, *Nz* = 5) (Source: Tsuji et al. (2007))

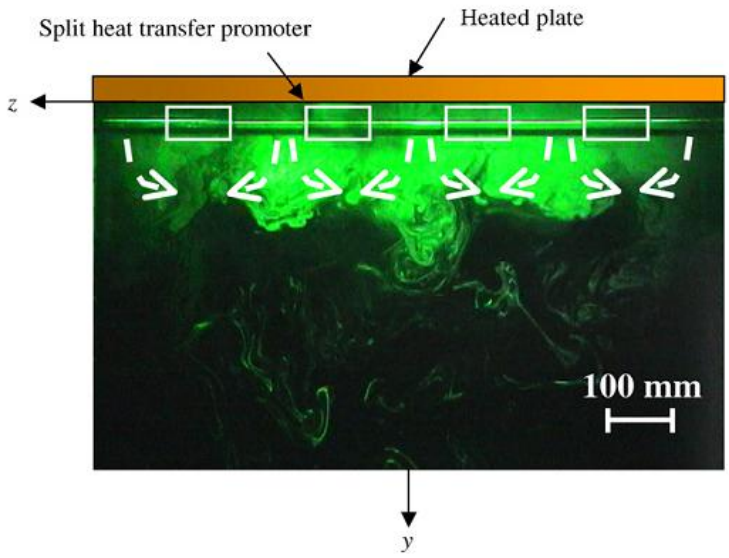

Figure 16: Visualized fluid motions in the downstream region of a split heat transfer (*y*-*z* plane, *Nz* = 4) (Source: Tsuji et al. (2007))

1.3.4 Literature Review on View Factor Calculation

As described in the previous chapter, thermal comfort can be valued in terms of operative temperature. Eq. (1) points out that the mean radiant temperature (MRT) should be evaluated as part of the effort to obtain operative temperature as well as air temperature.

The MRT is a concept arising from the fact that the net exchange of radiant energy between two objects is approximately proportional to their temperature difference multiplied by their ability to emit and absorb heat (emissivity). MRT is simply the area weighted mean temperature of all the objects surrounding the body. This is valid as long as the absolute temperatures of objects in question are large compared to the temperature differences, allowing linearization of the Stefan-

Boltzmann Law in the relevant temperature range. Technically, MRT is defined as the uniform temperature of a surrounding surface giving off blackbody radiation (emissivity e = 1) which results in the same radiation energy gain on a human body as the prevailing radiation fluxes which are usually very varied under open space conditions. Eq. (19) formulates the expression for the MRT, which is the summation of surface temperature multiplying by a view factor from a person to the surface.

$$t_r = \sum F_{p\text{-}i} t_{si} \tag{19}$$

where, t_r is the MRT, F_{p-i} is the view factor (angle factor, configuration factors, form factors or shape factors) from a person to surface i, and t_{si} is the surface temperature.

The view factor in the Eq. (19) refers to the proportion of all that radiation which leaves person and strikes surface p. Figure 17 and Eq. (20) explain the calculation of the view factor between two infinitesimal surfaces, where dA_1 and dA_2 are two infinitesimal surfaces, and s is the distance between the two surfaces. The angle between line s and the surfaces d_{A1} and d_{A2} are θ_1 and θ_2, respectively.

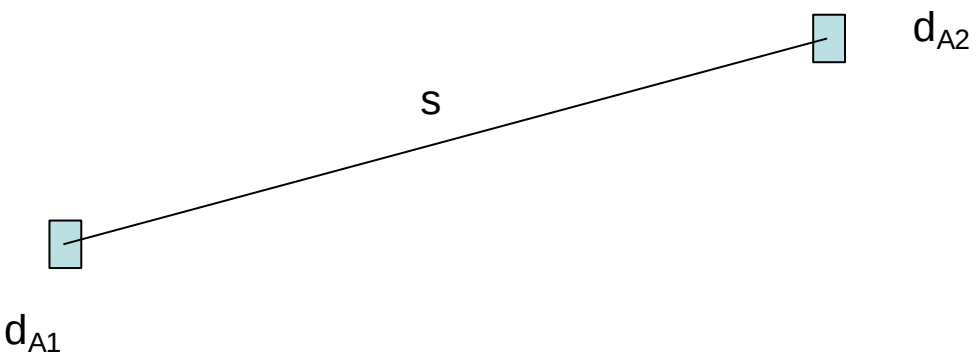

Figure 17: Schematic diagram of view factor between two infinitesimal surfaces

$$F_{d_{A1}\text{-}d_{A2}} = \iint_{A_1,A_2} \frac{\cos\theta_1 \cos\theta_2}{\pi s^2} dA_1 dA_2 \tag{20}$$

Because of the double surface integral in the Eq.(20), analytical solutions of view factor between two finite surfaces can be difficult, or sometimes impossible to obtain, if the geometries of the surfaces are complicated such as spheres, cylinders. Dunkle (1963) calculated the view factors from the inner-wall of a room to an occupant who either stands or sits inside the room. In order to simplify the complicated surface integral of a human body, the body was treated as a sphere. The equivalent sphere radii of the standing occupant and the seated occupant are expressed by:

$$R^2 = 0.65 + \cos\alpha(0.715 + 0.52|\cos\varphi|) \tag{21}$$

$$R^2 = 1.365 + (0.2 + 0.673\sin\alpha)\cos\alpha\cos\varphi \tag{22}$$

where α is the vertical angle from horizontal to point on surface, φ is the azimuth angle between direction faced and point on surface.

Eq. (21) refers to the radius of a standing person and Eq. (22) refers to the radius of a seated person. The two view factors which from a point on a wall to the two spheres are provided as below. Eq. (23) refers to the view factor of a standing person, and Eq. (24) refers to the one of a seated person.

$$f=\frac{R^2D}{(x^2+y^2+z^2)^{\frac{3}{2}}} \tag{23}$$

$$f=\frac{R^2Dh\omega^{\frac{1}{3}}}{30.8(x^2+y^2+z^2)^{\frac{3}{2}}} \tag{24}$$

Feingold and Gupta (1970) found the analytical solution to evaluate the view factors from a sphere to a coaxial disk; from a sphere to an infinitesimal area lying in a plane which does not intersect the sphere; from a sphere to a segment of a coaxial disk, from a sphere to a coaxial rectangle; from a sphere to a coaxial right circular cylinder; from a sphere to a Polygon; from a sphere to a noncoaxial disk. Sabet and Chung (1987) proposed a general Equation to calculate the view factor from a sphere to any nonintersecting planar surfaces:

$$F_{2\text{-}1}=\frac{d}{2\pi}\int_{x_1}^{x_2}\frac{f(x)}{(x^2+d^2\sqrt{x^2+[f(x)]^2+d^2})}dx \tag{25}$$

where: *2* is the sphere surface; *1* is any nonintersecting planar surface; *d* is the distance of the center of the sphere to the plane; *f(x)* is a characteristic function depending on the shape of the planar surface.

1.3.5 Literature Review of Multi-mode Heat Transfer

In the field of air-conditioning and refrigeration, the combination of radiative and natural convective heat transfer was first studied to investigate the performance of wire-and tube condensers of refrigerators.

Tagliafico and Tanda (1997) investigated the air-side heat transfer from wire-and-tube heat exchangers in the application of refrigeration. The radiation heat transfer between refrigerant and ambient air was modeled using a diffuse, gray-body network method. The natural convection part was modeled by a semi-empirical correlation. It was reported that the fractional contribution of convection to the combined-mode heat transfer was between 40% and 70% depending on the temperature difference and heat exchanger configuration (pitch-to-diameter ratio of the wires, pitch-to-diameter ratio of the tubes and normalized heat exchanger height).

$$Nu=0.66\left(\frac{RaH}{d_t}\right)^{0.25}\left\{1-\left[1-0.45\left(\frac{d_t}{H}\right)^{0.25}\right]\times\exp(-s_w/\varphi)\right\} \tag{26}$$

where

$$\varphi=\left(\frac{C_1}{H}\right)^{0.4}s_w^{0.9}s_t^{-1.0}+\left(\frac{C_1}{H}\right)^{0.8}\left[\frac{C_2}{T_t-T_\infty}\right]^{0.5}s_w^{-1.5}s_t^{-0.5}$$

$$s_1=\frac{p_t-d_t}{d_t};s_w=\frac{p_w-d_w}{d_w};C_1=28.2\text{ m};C_2=264\text{ K}$$

Melo and Hermes (2009) proposed a more complicated correlation by considering more parameters, Eq. (27), and Table 3 describes the dimensionless used in the equation.

$$\pi_0=5.68\cdot\pi_1^{0.6}\pi_2^{-0.28}\pi_3^{0.49}\pi_4^{0.08} \quad (27)$$

Table 3: Dimensionless group and description in Eq. (27) (Source: Melo and Hermes (2009))

Dimensionless group	Description
$\pi_0=(h_c+h_r)/h_r$	Combined heat transfer coefficient
$\pi_1=A_w/(A_t+A_w)$	Heat transfer surface
$\pi_2=(p_t-d_t)/d_t$	Tube spacing
$\pi_3=(p_w-d_w)/d_t$	Wire spacing
$\pi_4=(t_{avg}-t_{air})/t_{film}$	buoyancy

Bansal et al (2003) developed a model using FORTRAN 90 code and simulated the wire-and-tube condenser under different ambient conditions. The modeling results show that the dominant heat transfer mode for wire-and-tube condenser is by convection, which contributes up to 65% of the total heat transfer. Gupta et al (2008) improved Bansal's model by considering the effects of aluminum tape to a hot-wall condenser.

Rao et al. (2006) focused on a more fundamental study whose subject were only two fins in an enclosure (Figure 18). Alternating direction implicit (ADI) method was used to solve the governing equations. Isotherms and stream lines were obtained in the paper as well as the average Nusselt number and a fin effectiveness correlation.

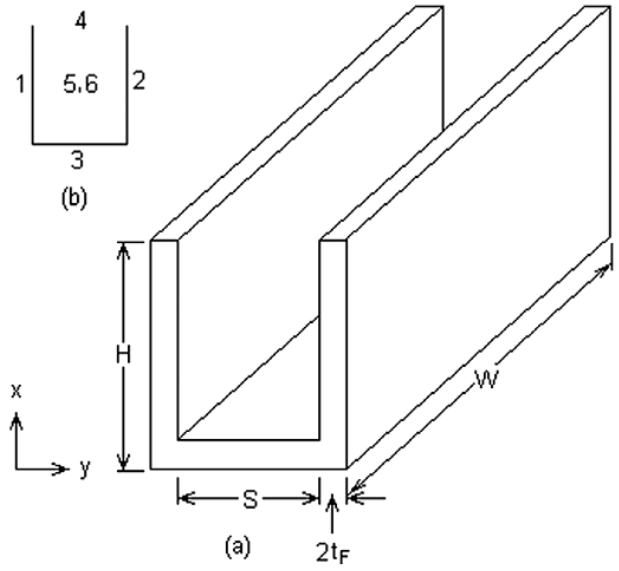

Figure 18: (a) Physical model of two-fin enclosure. (b) Different surfaces in radiation enclosure (Source: Rao et al. (2006))

Kuznestov and Sheremet (2008) numerically studied the convective-radiative heat transfer in an enclosure having finite thickness heat-conducting walls and a heater at the bottom. Air (Pr = 0.7) was the fluid inside the enclosure, and the Grashof number in the problem was varied from 10^5 to 10^7. Isotherms and streamlines were obtained and the influence of some parameters, such as the Grashof number, the transient factor, the optical thickness and the heat conductivity ratio, on formation of thermo-hydrodynamic modes was analyzed. It was determined, that taking into account of the radiative heat transfer leads to the temperature increase in the gas cavity on the average of 11% at $0 < \tau < 200$. Talukdar (2004) studied the multi-mode heat transfer in a porous channel bounded by isothermal parallel plates. Chiu (2007) investigated the problem in rectangular ducts rotating about a parallel axis. Both Chiu et al. (2007) and Premachandran (2006) studied the problem in a horizontal channel.

Krishnan et al. (2004) conducted an experimental and semi-experimental investigation on steady-state natural convection and surface radiation between three parallel vertical plates with a hot plate in the middle and the other two unheated ones each side. The radiative heat transfer (in terms of Nusselt number) calculation was conducted by the radiosity-irradiation method, and the convective heat transfer (in terms of the Nusselt number) was obtained from an experiment featuring six plate spacing ranging from 12.66 to 52.2 mm and for an order of magnitude range of wall-to ambient temperature difference. It was concluded that even at low temperature, 310K, the significance of radiation heat transfer rate cannot be ignored. A correlation for the average convective Nusselt number was also developed at the range of $2{,}370<Gr<872{,}700$.

1.4 Summary of Literature Review

In the current study of SSLC systems, most papers use one vapor compression cycle for sensible cooling and a desiccant device for latent cooling. The desiccant device can be either a solid desiccant wheel or liquid desiccant. Due to the restriction of regeneration temperature, the desiccant device has to be reactivated either by waste heat from a CHP unit or an electric heater.

ASHRAE standard 55 provides a complete guideline to evaluate the indoor thermal comfort conditions. The ASHRAE thermal comfort zone uses the operative temperature instead of air temperature as its measurement which implies the importance of MRT in the thermal comfort evaluation. In the automobile industry, the thermal comfort of car cabins has been widely discussed. Both experimental work

and numerical work are presented in the literature review. However, due to the unsymmetrical and extreme ambient conditions during the driving and the restricted cabin space, the thermal comfort model cannot be applied for large indoor space, such as office settings.

For the simulation of natural convection in an enclosure, CFD simulation is so far the only feasible option for the large Rayleigh number case. Analytical solutions or asymptotic solutions are either restricted to apply for small enclosures or for special dimensions like infinite long enclosures.

Through the literature review, the following areas are found to be worthy of further investigations. With the advance in material technology, solid desiccant wheel can now be regenerated at a lower temperature of around 50°C. This provides the opportunity of utilizing waste heat from the condenser to regenerate the desiccant wheel. Consequently, the new system can get rid of additional electric heaters or using waste heat from CHP units and therefore, further improves the COP of SSLC systems. It is necessary to study the characteristics of integration of VCS and condenser waste heat-driven DW. There is currently few literature related to thermal comfort analysis of SSLC systems or its sensible heat exchanger. The review of section 1.3.3 through 1.3.5 suggests that in order to simulate the operative temperature field created by the sensible heat exchanger, the air temperature can be obtained through CFD simulation and the MRT can be calculated analytically using view factor equations. It is also worthwhile to investigate any possible alternative method to save the computation cost of the CFD simulation of air temperature.

1.5 Research Objectives

The proposed work focuses on two main areas: energy saving and thermal comfort analysis when separate sensible and latent cooling (SSLC) systems are employed. For the energy savings aspect, the related research includes:

- Design an SSLC air conditioning system and compare its performance to a conventional system
- Compare the performance of SSLC systems using two refrigerants, R-410A and CO_2
- Based on the experimental results, establish models to simulate SSLC systems
    - Simulate SSLC system performance under different ambient conditions
    - Optimize the vapor compression cycle operation under each ambient condition
    - Explore maximum energy saving options (configurations) of an SSLC system

For the thermal comfort aspect, the following research was conducted:

- Establish experimental facility for thermal comfort measurement in a conditioned space and use the facility to validate the simulation results by thermal comfort models
- Establish a simulation tool to obtain thermal comfort zones in a space air-conditioned by low ΔT heat exchangers
    - Simulate natural convection and obtain air temperature field in the conditioned space

- Simulate radiation cooling (heating) and obtain mean radiation temperature field in the conditioned space
- Predict "operative temperature"

Chapter 2: Energy Saving Analysis of SSLC Systems

In Chapter 2, the energy saving potential of SSLC systems is investigated. Two different configurations of SSLC systems are discussed here. One SSLC system consists of two vapor compression cycles and the other one consists of one vapor compression cycle and one solid desiccant wheel. The first configuration is theoretically studied and simulated under different ambient conditions. The second configuration is studied both theoretically and experimentally because of its better performance. The technique of using divided HX is proposed to further improve the COP of SSLC systems. Finally, the SSLC-DW-enthalpy wheel (EW) configuration is introduced as the most energy saving SSLC system.

2.1 SSLC Systems Using Two Vapor Compression Cycles

2.1.1 System Description

The SSLC systems discussed in this section are called 2VCC SSLC systems. They use one vapor compression cycle to handle the sensible cooling load and a second one to handle the latent cooling demand from indoor and outdoor air. A counter flow internal heat exchanger is also used in the system to utilize the cooling from the latent evaporator for pre-cooling of the incoming air. Two different configurations of 2VCC SSLC systems are shown in Figure 19. In the first configuration, the sensible and latent heat exchangers are arranged in series along the process air flow direction. Return air from the space is mixed with outdoor fresh air before flowing into the sensible evaporator. After it passes through the sensible evaporator, the air flow is divided into two streams. While one stream is sent to the

reheat heat exchanger for pre-cooling and is processed through the latent evaporator, the other stream is bypassed. The air stream exiting the latent evaporator is then reheated through the reheat heat exchanger. The air stream bypassing and the one passing through the reheat heat exchanger are both sent to the space as supply air. In the second configuration, the sensible and latent heat exchangers are arranged in parallel. The only difference between the serial and parallel configurations is that in the parallel configuration the return air stream is split into two streams before being mixed with outdoor fresh air, and passes through the sensible heat exchanger.

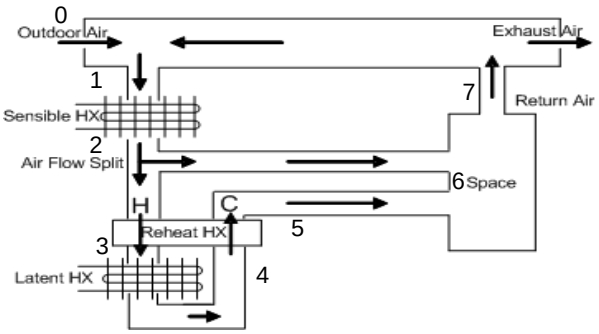

(a) Serial configuration

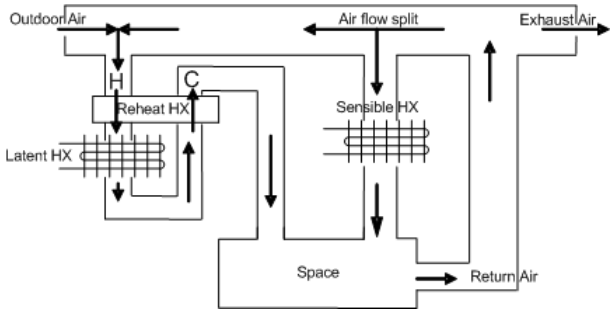

(b) Parallel configuration

Figure 19: Schematic diagram of the 2VCC SSLC system (showing only air loop)

2.1.2 System Modeling Approaches

Engineering Equation Solver (EES) (F-chart software, 2009) was used to model 2VCC SSLC systems. A conventional combined system was also simulated in the EES for comparison purpose. Assumptions used in the model are as follows:

Air side:

- Pressure drops and heat loss in the ducts and pipes are neglected.
- Return air and outdoor fresh air are well mixed.
- The air mixing process is adiabatic.
- Temperature distribution and mass distribution in the space are uniform.
- The ventilation air flow rates are the same in all systems.

Refrigerant side:

- Refrigerant: R-410A
- Degree of subcooling: 5 K (Whitman et al., 2004)
- Degree of superheating: 10 K (Whitman et al., 2004)
- Isenthalpic expansion
- Condenser pressure drop: 100 kPa (Casson et al., 2002)
- Evaporator pressure drop: 50 kPa (Domanski et al., 2005)
- Isentropic efficiency is calculated as a function of the pressure ratio (ASHRAE 2008): $\eta_{iso}=0.9-0.0467\times PR$ (Hwang, 2004).
- Volumetric efficiency is calculated as a function of the pressure ratio (ASHRAE 2008): $\eta_{vol}=1-0.04\times PR$ (Hwang, 2004)
- Compressor motor efficiency: 0.95 (ASHRAE, 2008)

Initial Conditions:

- Outdoor air condition is set to 35°C, 44% relative humidity (RH) (ARI standard 210/240, 2006)
- Outdoor air volume flow rate is set to be 0.9 m^3s^{-1} (ANSI/ASHRAE standard 62.1, 2004)
- Space air condition is set to 27°C, 50% RH (ARI standard 210/240, 2006)
- Space load is 100 kW.
- Sensible heat factor (SHF) of the space is 0.7.
- For the baseline system, the volume flow rate of air is set to be 5 m^3s^{-1} based on the space load of 100 kW (ASHRAE standard 140, 2004)

Ranges of conditions studied in the parametric study are:

- Outdoor temperature: 15°C ~ 37°C
- Outdoor humidity ratio: 5.8 gkg^{-1} dry air (15°C, 55% RH) ~ 28 gkg^{-1} dry air (37°C, 70% RH)

2.1.3 Modeling Results

Figure 20 shows the psychrometric processes of the two 2VCC SSLC systems (solid line) and the conventional reheat system (dotted line) in a psychrometric chart.

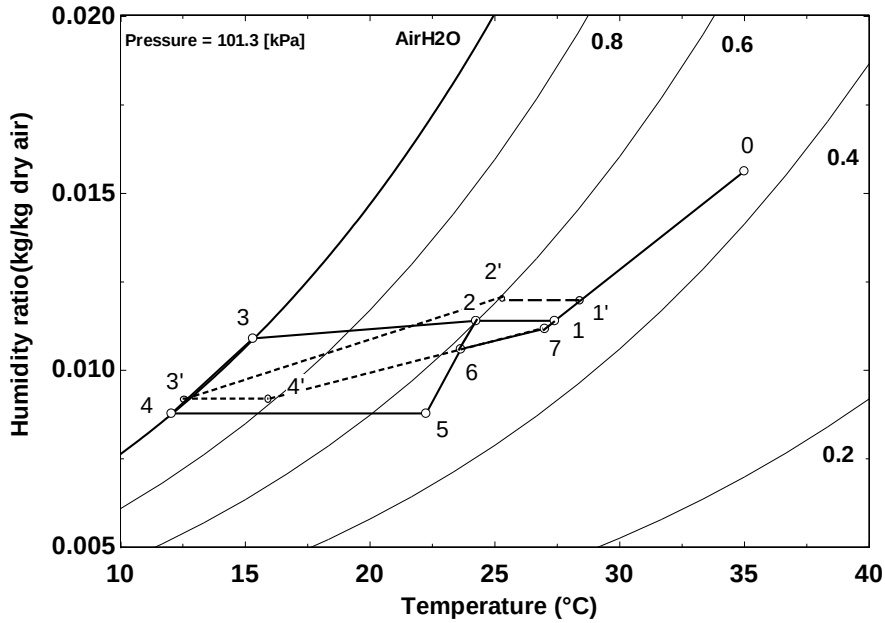

a) Psychrometric process of the serial SSLC configuration and the baseline system

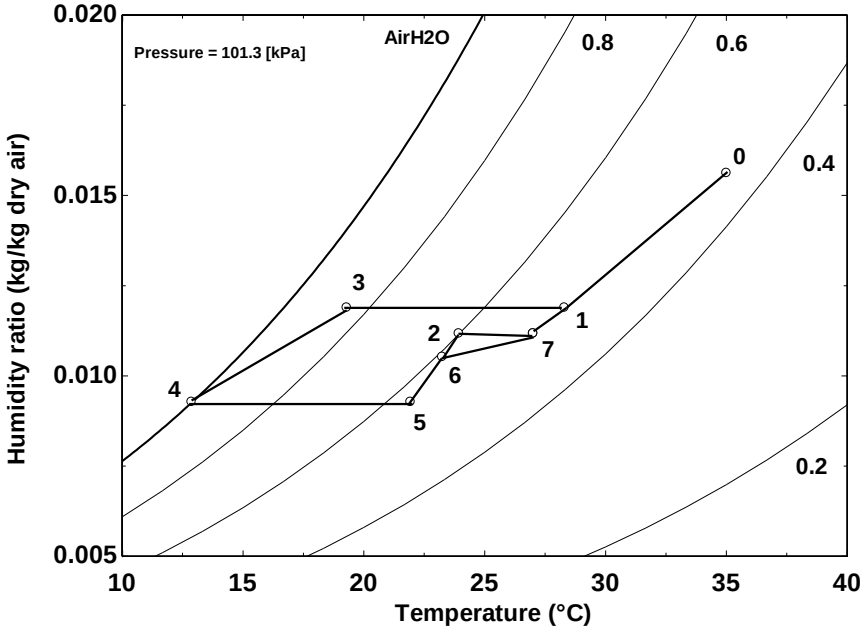

b) Psychrometric process of the parallel SSLC configuration

Figure 20: Comparison of SSLC systems and baseline system in psychrometric chart

(2VCC SSLC system: 0: outdoor condition, 7: indoor condition, 1: mixing point, 2: after sensible HX, 3: after pre-cooling, 4: after latent HX, 5: after reheat, 6: supply air;
Baseline system: 1': mixing point, 2': after pre-cooling, 3': after evaporator, 4': after reheat and supply air)

For the baseline system, in order to meet the cooling demand of the space, especially the dehumidification demand, which is 30 kW (from SHF = 0.7), air temperature exiting the evaporator is 12.8°C (from air flow rate 5 m^3s^{-1}), which is much lower than the dew point temperature 16.7°C. Based on the size of the evaporator used in the model, the evaporating temperature of the baseline system is 6.0°C. Decreasing the temperature of the return air below the dew point temperature consumes much power in the vapor compression cycle. The COP of the baseline system is 3.9. For the 2VCC SSLC system using serial configuration, the sensible heat load is removed separately at first. This is achieved by simply decreasing the return air temperature by 3°C. In this case, the air flow rate is increased to meet the total sensible load at a reduced temperature difference between the air and refrigerant. In order to do a fair comparison to the baseline system, the same air flow rate is used for the latent heat removal cycle of the SSLC. It is cooled down to approximately the same temperature as in the baseline system, which is 12.0°C. The power consumption of the SSLC system is 30% lower than the baseline system. The COP of the SSLC is 5.45, which is 39% higher than that of the baseline system. For the SSLC system using parallel configuration, the sensible heat load is removed by decreasing the return air temperature by 3°C. The same air flow rate is used for the latent heat removal cycle of the SSLC as in the baseline system, and it is also cooled down to 12.8°C. The COP of the SSLC system using parallel configuration is 5.50, which is 41% higher than that of the baseline system. The reasons behind these energy savings are described as follows. In the baseline system, the sensible cooling load is 78.3 kW, which accounts for about 64% of the total load, which is 119.6 kW,

including the space load and the ventilation load. The vapor compression cycle consumes 20 kWe. It also accounts for 64% of the total power, which is 30.5 kWe, to meet the sensible cooling load. However, in the SSLC system, the refrigerant evaporating temperature of the sensible cycle is increased to 19.1°C due to the higher air temperature. The sensible cycle compressor pressure ratio is decreased from 2.93 (baseline system) to 2.00 (SSLC system). The power consumption of the sensible cycle is reduced to 9.7 kWe, which means 10.3 kWe are saved as compared to the baseline system. For the latent cycle, both the baseline system and the SSLC system consume about the same power to remove the same amount of water vapor (16 gs^{-1}) as expected.

In order to keep the size of heat exchangers (HX) (excluding the internal HX) the same as for the baseline system, the total UA values (see Eq. (28) for definition) of evaporators and condensers are both set to be 50 kW K^{-1}, i.e., $UA_{total}=UA_{evap.}+UA_{cond.}=$Constant

$$UA=\frac{\dot{Q}}{\Delta T} \tag{28}$$

where:

$\dot{Q}$ is the heat exchanger capacity in kW

ΔT is the nominal temperature difference between refrigerant and air in K

Since there are two evaporators in the SSLC system which are responsible for a higher UA value than the one in the baseline system, a higher condensing approach temperature is expected in the SSLC system. This results in a slight increase in the power consumption of the latent cycle. However, the SSLC system still consumes 8.6

kWe less power than the baseline because of the less power input to the sensible cycle. In the sensible cycle, higher isentropic efficiency is expected than the baseline because the pressure ratio is reduced from 2.93 to 2.00. Indeed, the isentropic efficiency is increased from 0.76 to 0.81. There are also other benefits resulting from the SSLC system. The total displacement volume of the two compressors in the SSLC system can be 25% smaller than that in the baseline system. However, it should be noted that the evaporator air flow rate is increased from 5 m^3s^{-1} of the baseline to 15.9 m^3s^{-1} of the SSLC system. This is because the sensible cycle requires more air to meet the sensible cooling load with smaller air enthalpy difference than the baseline. This raises a question whether the increased power consumption of the fan motor will offset the power savings from compressors. This question is addressed in the following parametric studies.

2.1.4 Parametric Studies

Parametric studies were conducted in order to study charateristics of the 2VCC SSLC system under different operating conditions. In the parametric studies, the air temperature leaving the sensible evaportor was varied from 19°C, which was close to the dew point temperature, to 25.5°C. As shown in Figure 21, the COP of the SSLC system increases with the increase of the air temperature leaving the sensible evaporator. However, the trade off is the higher air mass flow rate. Figure 21 also shows that the highest COP coincides with the highest air mass flow rate, which is almost five times as high as the baseline system.

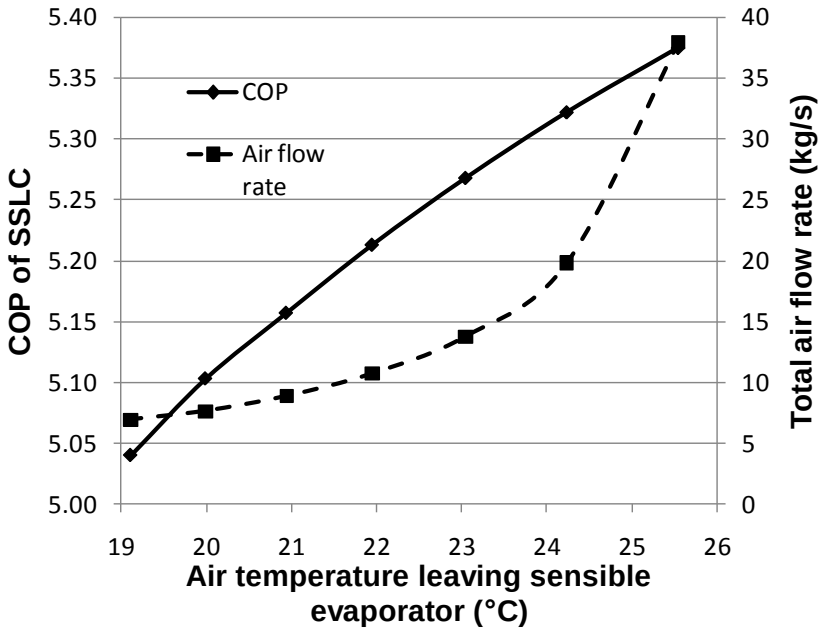

Figure 21: COP and total air flow rate under different air temperature leaving sensible evaporator

If both the COP benefit and the higher air mass flow rate disadvantage are considered, the temperature leaving the sensible evaporator can be set between 22°C (70% RH) and 24°C (60% RH). Since the higher temperature condition (24°C, 60% RH) shows a higher COP, that condition is selected for the rest of the study. The SSLC system shows different power saving potentials under different ambient conditions.

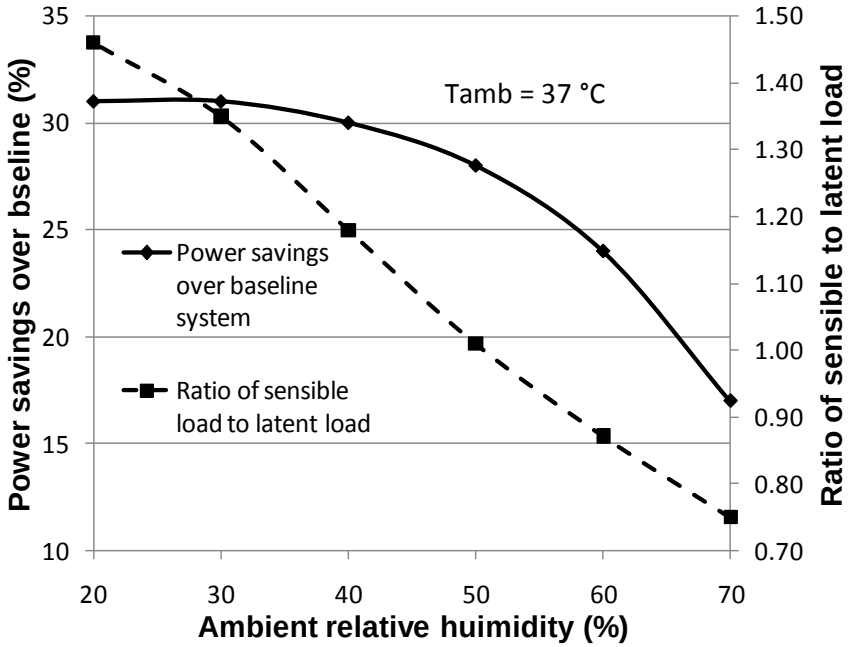

Figure 22: Power savings and ratio of sensible to latent load under different ambient relative humidities

Figure 22 demonstrates the SSLC system's power savings over the baseline under different ambient relative humidities. While the ambient temperature was set to be 37°C, the relative humidity varied from 15% to 75%. The result demonstrates the feature of distributing the sensible and latent cooling load depending on the ambient condition. While the sensible load of the system was kept constant at 66 kW, the latent load varied from 38 kW to 88 kW. Therefore, the ratio of sensible load to latent load decreases with the increase of relative humidity, which is shown on the secondary y-axis. It is also observed that the power savings decreases when the ambient relative humidity increases. This is because more power is required from the latent cycle, which makes the savings from the sensible cycle less significant. However, even under the highest relative humidity condition, the power savings is over 15% as compared to the baseline system.

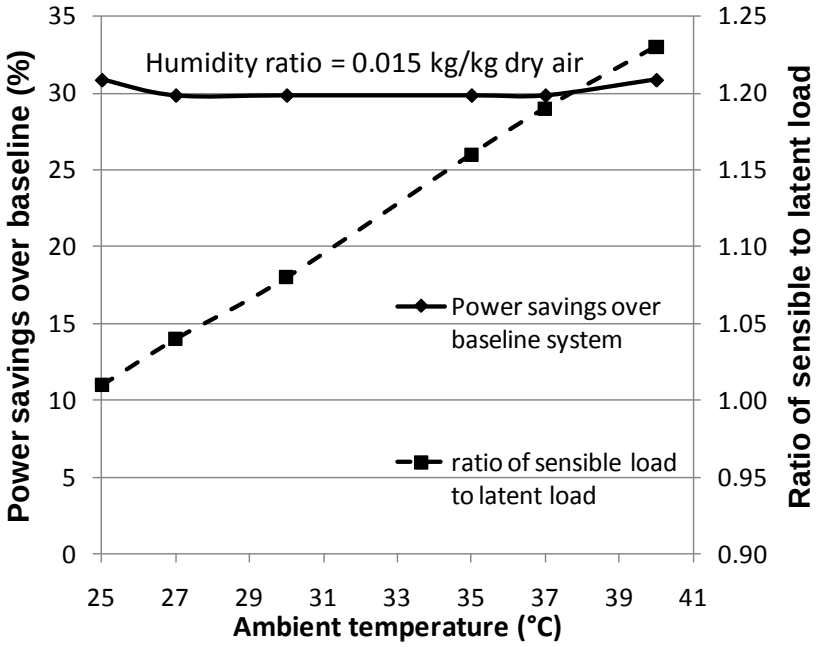

Figure 23: Power savings and ratio of sensible to latent load under different ambient temperatures

Figure 23 shows the power savings under different ambient temperatures. The ambient humidity ratio was set to be constant at 15 gkg^{-1} dry air, while the temperature varied from 25°C to 40°C. As shown in Figure 23, the ratio of the sensible to latent cooling load increases with the ambient temperature. Meanwhile, the power savings remains almost constant. This trend indicates that the power savings of the system is greatly affected by the latent load of the system but is not much affected by the sensible load. Detailed discussion is provided in the later chapter.

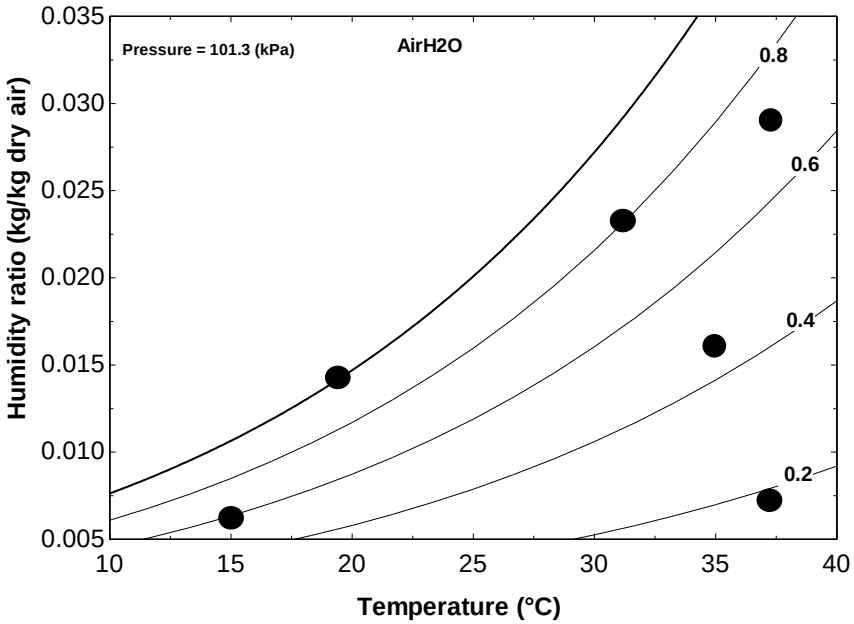

Figure 24: Six different climate conditions plotted on the psychrometric chart

(Clockwise from the top right: hot and humid; standard; hot and dry; mild and dry; mild and humid; humid)

To evaluate the performance of the SSLC system over a wide envelope of ambient conditions, the system performance was modeled under six different climatic conditions as shown on the psychrometric chart in Figure 24. The power savings over the baseline system was calculated for different climate conditions. The results are summarized in Table 4. The maximum power savings is achieved in cool and dry conditions, and the minimum in hot and humid conditions. It has been observed that under hot and humid conditions the power of the latent cycle accounts for 70% of the total power consumption and affects the total power savings of the SSLC system.

Table 4: Power savings under different climate conditions

Zone	Standard	Mild and dry	Mild and humid	Hot and dry	Hot and humid	Humid
Condition	35°C/44% RH	15°C/55% RH	20°C/100% RH	37°C/15% RH	37°C/70% RH	32°C/80% RH
Power savings	30%	50%	33%	32%	17%	22%

2.1.5 Air Distribution Methods

The duct design and fan power consumption calculation were compared for the baseline system and the SSLC system. In the baseline system, the total air side pressure loss in the system is around 285 Pa, including 100 Pa from the evaporator coil (calculated from the model below), 160 Pa from the duct and fittings and 25 Pa from the filters, etc. (ASHRAE, 2005). Therefore, the fan motor was chosen based on the necessary pressure lift of 285 Pa, and the volume flow rate was of 5 m^3s^{-1}. Compared with the baseline system, the SSLC system has several times higher air flow rate through the sensible heat exchanger depending on the choice of exit air temperature. A high air flow rate causes large pressure drop in the conventional multi-bank heat exchanger, which leads to high power consumption of the fan motor. The fan power requirement would partly offset the energy savings of the SSLC's vapor compression cycle. Thus, the duct-fan arrangement used for the baseline air distribution is not suitable for an SSLC system. In order to maintain the fan power consumption as low as possible while providing a high air flow rate through the system (to keep the COP high), one possible solution is to minimize the pressure lift of the fan motor.

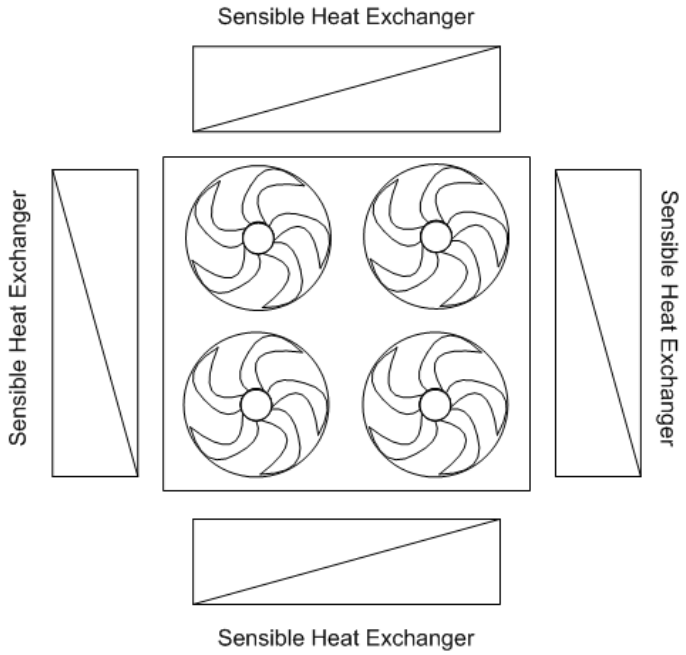

Figure 25: Air distribution method for the SSLC system

Kopko (2002) presented a concept using an entire drop ceiling as the plenum to distribute a large air flow rate. The air in the plenum is transported slowly so that there is much smaller pressure drop than the typical duct design. In light of this, a propeller fan, which produces relatively high air flow rate at low pressure head, can be utilized. A new air distribution method consisting of the sensible heat exchanger(s) and the plenum is proposed for the SSLC system as shown in Figure 25. Detailed discussion on the heat exchanger design is provided in the later chapter. The sensible heat exchangers are arranged around the fans in the plenum. Air is taken from the bottom by propeller fans, flows through the heat exchangers and is distributed to the space through openings placed along the entire plenum. The sensible heat exchanger is designed to be one bank, increasing HX frontal area to minimize the frontal velocity. According to this new design, the fan can be chosen to provide high air flow rate, which is 15.9 m^3s^{-1} (corresponding to 24°C exit temperature) and low pressure

lift of 62.5 Pa for the SSLC system. The pressure lift is determined by assuming 50 Pa pressure drop from the evaporator and 12.5 Pa from the other parts in the system. Fan laws (ASHRAE, 2008) were used to compare the fan motor power consumptions of the two systems. The requirements of the two fans are listed in Table 5.

Table 5: Pressure lift and air flow rate requirements for fans used in the baseline and SSLC systems

System configuration	Pressure lift (Pa)	Air flow rate at the given pressure lift (m^3s^{-1})
Baseline system	$P_2 = 285.0$	$Q_2 = 5.0$
SSLC system	$P_1 = 62.5$	$Q_1 = 15.9$

Eq. (29) shows the effect of changing fan size, pressure and density on volume airflow rate:

$$Q_1=Q_2\left(\frac{D_1}{D_2}\right)^2\left(\frac{P_1}{P_2}\right)^{\frac{1}{2}}\left(\frac{\rho_2}{\rho_1}\right)^{\frac{1}{2}} \quad (29)$$

Eq. (30) shows the effect of changing fan size, pressure and density on rotation speed:

$$N_1=N_2\left(\frac{D_2}{D_1}\right)\left(\frac{P_1}{P_2}\right)^{\frac{1}{2}}\left(\frac{\rho_2}{\rho_1}\right)^{\frac{1}{2}} \quad (30)$$

Eq. (31) shows the effect of changing fan size, pressure and density on power consumption:

$$W_1=W_2\left(\frac{D_1}{D_2}\right)^2\left(\frac{P_1}{P_2}\right)^{\frac{3}{2}}\left(\frac{\rho_2}{\rho_1}\right)^{\frac{1}{2}} \quad (31)$$

By substituting Eq. (29) into Eq. (30) to cancel out the ratio of diameters, using the data in Table 5, and neglecting the density difference, the ratio of RPMs becomes Eq. (32):

$$\frac{N_1}{N_2}=\left(\frac{Q_2}{Q_1}\right)^{\frac{1}{2}}\left(\frac{P_1}{P_2}\right)^{\frac{3}{4}}=0.18 \tag{32}$$

By substitute Eq. (29) and Eq. (32) to Eq. (31) and using the data in Table 5, we obtain the ratio of power consumptions:

$$\frac{W_1}{W_2}=\left(\frac{N_1}{N_2}\right)^{\frac{4}{3}}\left(\frac{Q_1}{Q_2}\right)^{\frac{5}{3}}=0.70 \tag{33}$$

Eq. (33) shows that it is theoretically possible for a SSLC system to save 30% in fan motor power consumption from the baseline. The reason is that the rotation speed of the fan motor could be reduced in the SSLC system to only 18% of the one in baseline. By plugging in the data from Table 5 into Eq. (29), it was found that the fan diameter in the SSLC system was 2.6 times larger than that in the baseline system.

2.2 SSLC Systems Using One Vapor Compression Cycle and One Desiccant Wheel

2.2.1 Experimental Setup

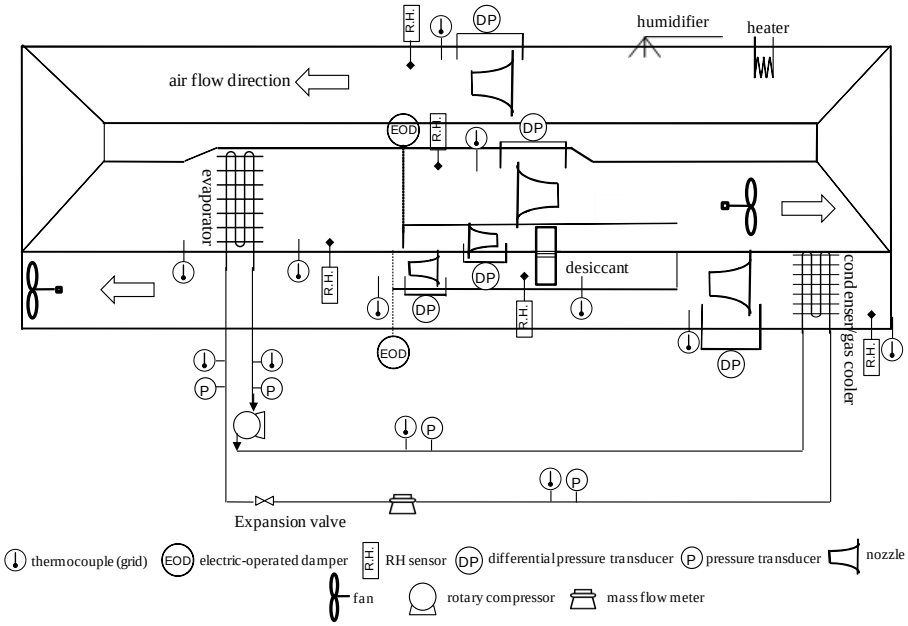

Figure 26: Schematic diagram of the experimental setup for SSLC system test

Figure 26 shows the schematic diagram of the experimental setup. The experimental setup consisted of a vapor compression system and two wind tunnels. In the vapor compression system, two pairs of compressors, evaporators, a condenser and a gas cooler were prepared for the R-410A and CO_2 tests. The two variable-speed rotary compressors provided the same cooling capacity, which was set to be 3.5 kW. The two evaporators and condenser (gas cooler) were almost identical to each other, except that the tube thickness of the R-410A heat exchangers was much thinner than that of the CO_2 heat exchangers (0.3 mm versus 1.0 mm). All the heat exchangers were made of copper tubes and aluminum fins. An electronic expansion valve was used to control the pressure ratio and mass flow rate of the refrigerants. The two wind tunnels were constructed by polypropylene boards in order to simulate an indoor

condition and an outdoor condition, respectively. The two operating conditions were chosen based on the AHRI standard 210/240 test condition (AHRI, 2008), which are 27°C, 50% RH for the indoor condition and 35°C, 44% RH for the outdoor condition. The indoor tunnel was built in a closed loop, as no ventilation air was added to the inside air stream. The outdoor tunnel was a straight both-ends-open duct and built adjacently to the aforementioned closed loop. A 305 mm × 102 mm gap was cut between the two tunnels so that a 300 mm × 100 mm DW could fit inside of it. The DW, which was a cylindrical shape with honeycomb-shaped cells, slowly rotated as it continuously dehumidified the incoming process air-flow. Both the indoor and outdoor tunnels were separated into two sub-tunnels in the vicinity of the DW. The cooled air from the evaporator was divided into two parts. A large portion of it bypassed the DW, and assumed to be directly supplied to a space, while the rest moved through the DW. The distribution of the two air flows was decided based on the required latent capacity (0.7 kW). For the open duct, the same amount of airflow as used in the process duct was sent to regenerate the DW while the rest was directly exhausted out of the system.

Table 6: Specifications of experimental components and instruments used in the SSLC test

Component / instrument	**Specification**
closed loop air flow range	up to 2,100 kg h^{-1}, inverter controlled
open duct air flow range	up to 1,000 kg h^{-1}, inverter controlled
DW	diameter: 300 mm, axial width: 100 mm rotation speed: 10-25 revolutions per hour (RPH)
compressors	(CO_2) rotary compressor: 3.9 cm^3 (displacement/revolution) (R-410A) rotary compressor: 13.2 cm^3
evaporators	frontal area: 704 mm (H) x 699 mm (W) 4 banks, 32 tubes/bank, 4 parallel circuitry fin pitch: 2.0 mm, fin thickness: 0.2mm

	(CO_2) tube outer diameter: 7.94 mm, thickness 0.80 mm, bare tube (R-410A) tube outer diameter: 7.94 mm, thickness 0.31 mm, bare tube
condensers/gas coolers	frontal area: 484 mm (H) x 622 mm (W) 4 banks, 22 tubes/bank, 2 parallel circuitry fin pitch: 2.0 mm, fin thickness: 0.2 mm (CO_2) tube diameter: 7.94 mm, thickness 0.80 mm, bare tube (R-410A) tube diameter: 7.94 mm, thickness 0.31 mm, bare tube
nozzles	DW, size: 7.6 cm diameter, range: 280-660 kg h^{-1} condenser/gas cooler, size: 12.7 cm diameter, range: 790-1,800 kg h^{-1} evaporator, size: 17.8 cm diameter, range: 1,500-3,600 kg/h
relative humidity sensors	Duct mount-type (uncertainty: ±2% RH, range: 0-100% RH）
thermocouples	Type T (uncertainty: 0.5 K, range: -200 to 350 °C)
pressure transducers	Capacitive pressure transducer (uncertainty: ±0.11 % FS, FS: 7 MPa and 21 MPa
differential pressure transducer	Capacitive differential pressure transducer (uncertainty: 1% FS, range: 0-250 Pa & 0-1,250 Pa)
refrigerant mass flow meter	Coriolis flow meter (uncertainty: 0.05%, reset range: 0-60 g s^{-1})
power transducer	AC watt transducer (uncertainty: 0.2% FS, range: 0-4 kWe)

Table 6 lists the specifications of measure instruments and components used in the experiment.

As described above, the temperature and humidity ratio of the indoor and outdoor conditions were decided based on the AHRI standard 210/240. The outdoor condition was controlled by an environmental chamber, where the experimental setup including the outdoor unit, indoor loop and desiccant was installed. The indoor condition was controlled by the heater and humidifier listed in Figure 26. The sensible cooling capacity, latent capacity (which was provided by the DW) and the compressor power consumption were measured. The airflow rate passing through the DW was set to be 300 kg h^{-1} and 350 kg h^{-1} for the different regeneration temperatures of 55°C and 50 °C, respectively. The EOD dampers listed in Figure 26 were used to control the distribution of air flows into sub-tunnels. The regeneration

temperature was set to be in the range of 45°C to 55°C, and the condenser (gas cooler) was the only heat source. The cooling capacity of the vapor compression system was set to be 3.5 kW, and the required latent capacity was 0.7 kW.

Charge optimizations were conducted for both refrigerants at the condition of maintaining air leaving the condenser (gas cooler) at 50°C and air leaving the evaporator at 20°C. Table 6 lists the specifications including the uncertainties of components and instruments in the tests. The detailed information of test conditions is included in Table 7.

Table 7: Detailed test condition settings in the SSLC test

Parameter	**Setting**	**Description**
space cooling capacity	3.5 kW	effective cooling capacity delivered by evaporator to space
latent capacity	0.7 kW	sensible heat factor (SHF)=0.8
indoor condition	27°C, 50% RH	fixed at the inlet of evaporator
evaporator outlet temperature	18°C, 20°C, 22°C	DW process side inlet temperature
outdoor condition	35°C, 44% RH	fixed at the inlet of condenser/gas cooler
condenser/gas cooler outlet temperature	45°C, 50°C, 55°C	DW regeneration side air temperature
air flow rate through the DW	300 kg/h, 350 kg/h	same air flow rate for both dehumidification and regeneration
DW rotation speed	0 rph, 10 rph – 25 rph	

2.2.2 Test Results

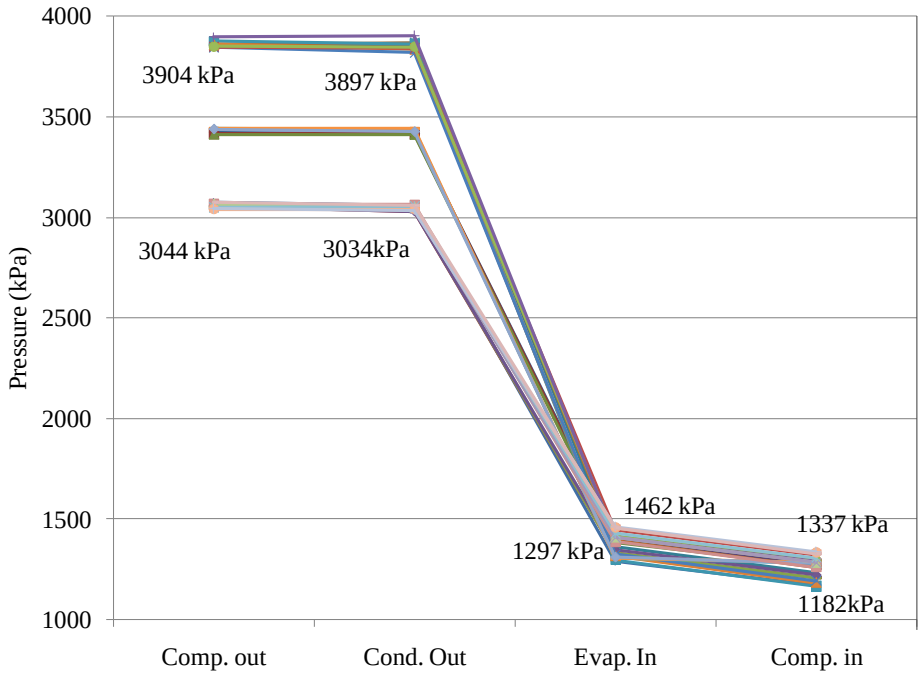

Figure 27: Pressure range of R-410A SSLC test

(Different line colors represent different test conditions)

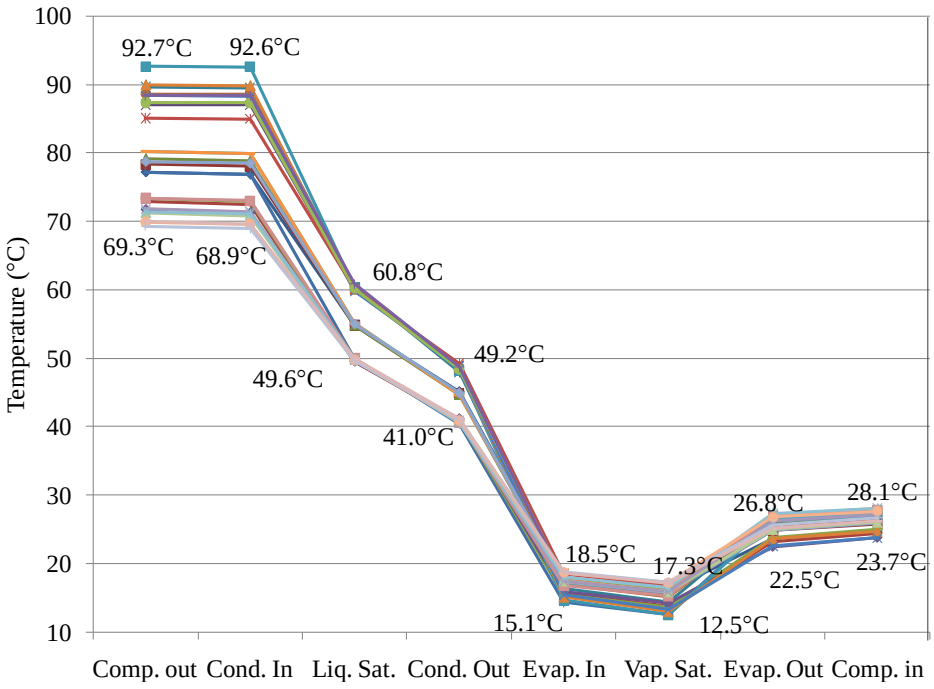

Figure 28: Temperature range of R-410A SSLC test

(Different line colors represent different test conditions)

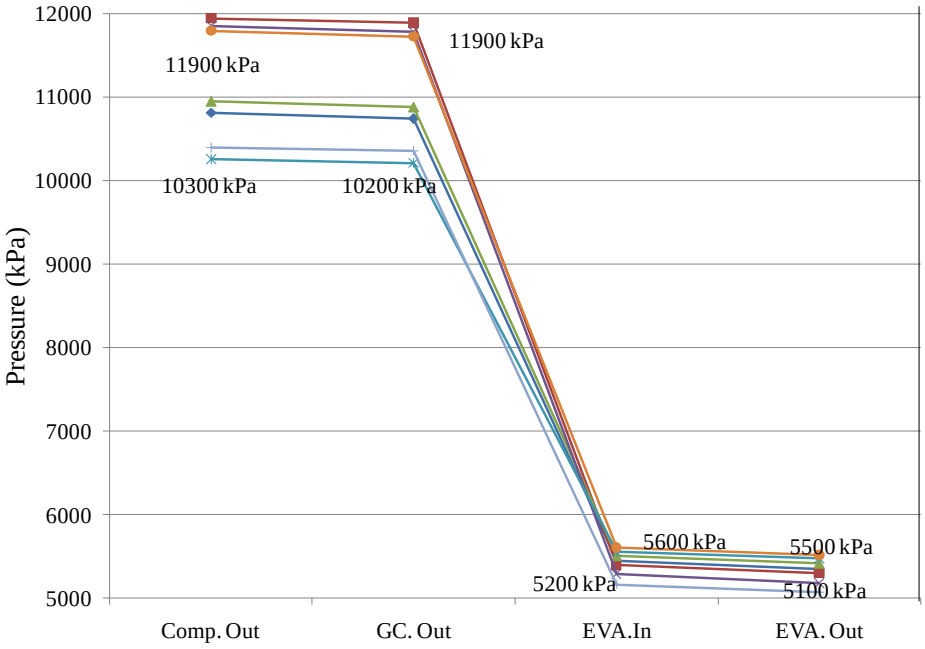

Figure 29: Pressure range of CO_2 SSLC test

(Different line colors represent different test conditions)

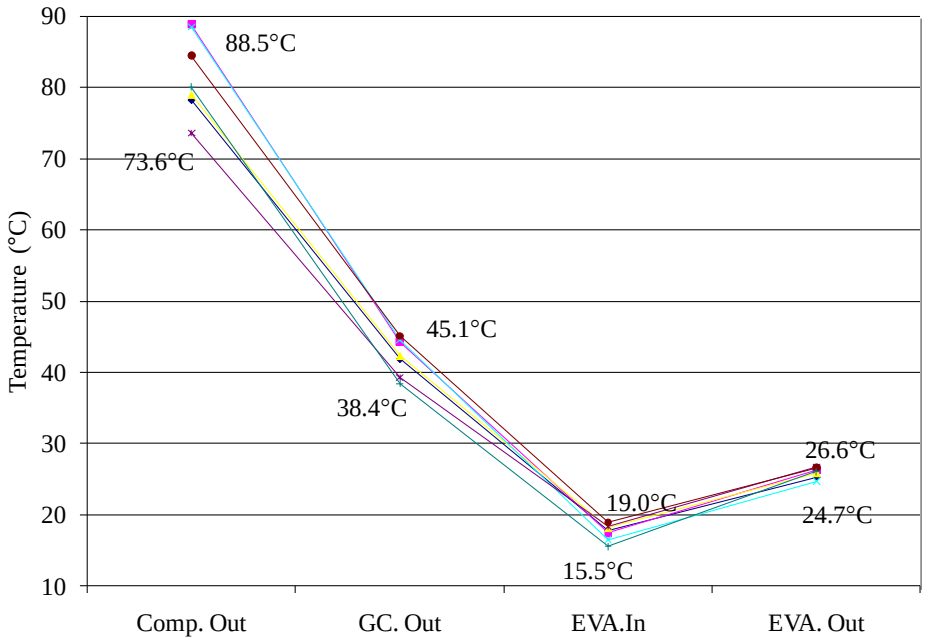

Figure 30: Temperature range of CO_2 SSLC test

(Different line colors represent different test conditions)

The refrigerants' pressure and temperature profiles in the tests were plotted from Figure 27 to Figure 30. The evaporating pressure and temperature changed with different supply air temperatures, which varied between 18°C and 22°C. At the same supply air temperature, several different vapor compression cycle conditions which delivered the same of amount of cooling were created by simultaneously adjusting the opening of the electronic expansion valve (EXV) and frequency of the variable speed compressor. The purpose of such adjustment was to find the maximum COP at the given condition. Such adjustment also affected the high side pressure and temperature. The other factors causing the different high side conditions were the different regeneration air temperature requirements, which varied between 45°C and 55°C. The numbers listed in the graph represent the upper and lower boundaries of

the aforementioned ranges. Uncertainties of measured data were calculated based on instruments' system error, which was listed in Table 6, and random error was taken from a standard deviation of a set of measured data.

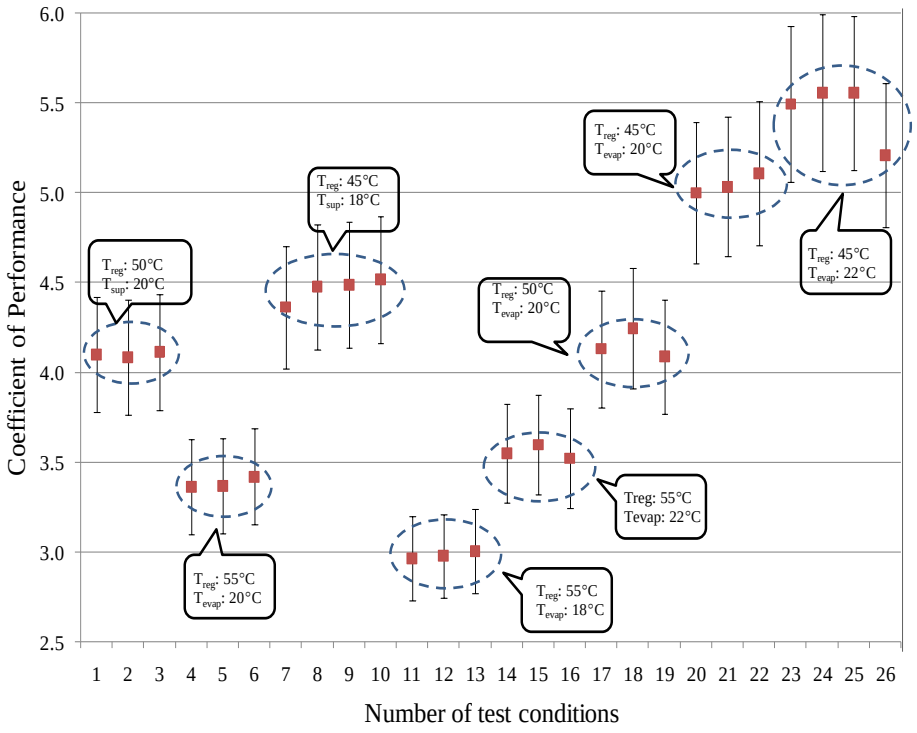

Figure 31: COP profile of R-410A SSLC tests with error bars (different clusters represent different test conditions)

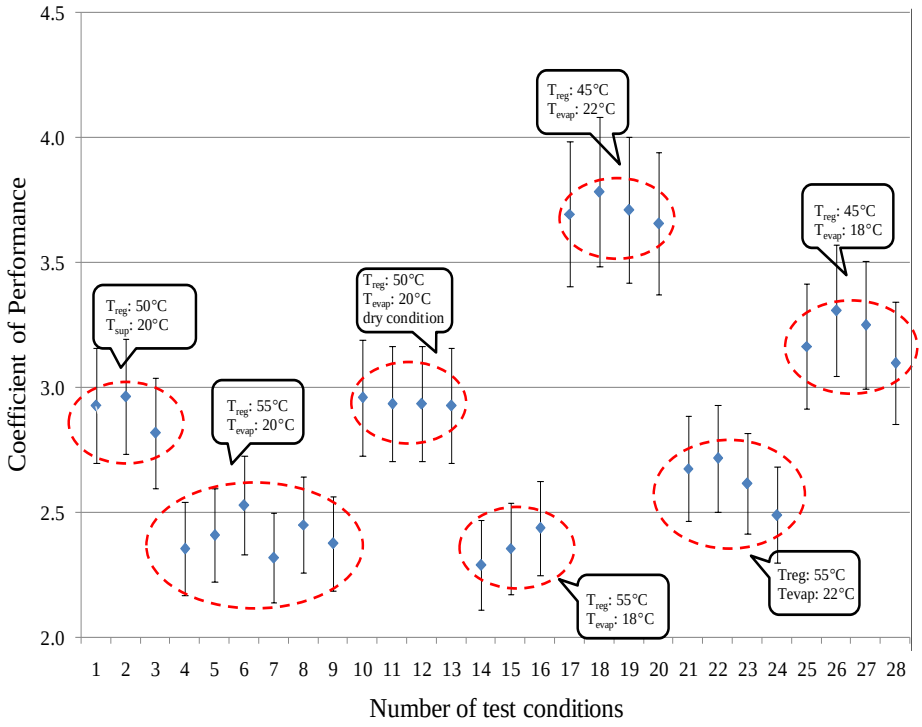

Figure 32: COP profile of CO_2 tests with error bars (different clusters represent different test conditions)

The COP profiles of both refrigerants' SSLC tests were summarized in Figure 31 and Figure 32. Each test condition, which is defined by one supply air temperature (T_{sup}) and one regeneration air temperature (T_{reg}), is represented by a cluster of points, which were created by different compressor frequencies and different EXV openings. For the condition of T_{reg} = 50°C and T_{sup} = 20°C, an additional dry condition was tested. When conducting the test at low-humidity ambient condition, the environmental chamber's humidifier was off, which made the humidity ratio inside the chamber less than 5gkg^{-1} dry air. The purpose of creating such condition is to test the performance of the DW. It was found that the DW performed better in the dry ambient condition than in the standard condition, but basically, it had no effect on improving the vapor compression cycle's COP. It is because the role of DW in the

entire system was found to be independent from the vapor compression cycle, which is discussed in the following chapter.

The general role of a DW in an SSLC system is to remove the latent load by absorbing water vapor from the process air and dumping it to regeneration air. The dehumidification performance of a DW is mostly affected by air frontal velocity, regeneration temperature and DW rotation speed (ASHRAE, 2008). To be more specifically, a high regeneration temperature, a low air frontal velocity and a fast-rotating DW have a positive effect on dehumidifying a unit rate of air flow. In the tests, in order to maintain the same latent capacity, which was 0.7 kW, at different regeneration temperatures, different amounts of air were sent to the DW and the rotation speed of the DW were carefully adjusted. Based on these characteristics, it was concluded that, in an SSLC system, a DW can independently control latent load from a vapor compressor cycle. An improved dehumidification performance over a unit rate of air under a fixed latent capacity only brings the benefit of a reduced amount of air required by the DW. Alternatively, a reduced dehumidification performance can be compensated through providing a larger amount of air. Furthermore, operation of DWs has only a limited effect (heat of adsorption) on a vapor compression cycle. Most DW operates closely along an isenthalpic line, which makes such operation basically convert the same amount of latent cooling to sensible cooling. This means that as long as the latent capacity is fixed, no matter how the DW operates, for example, at different regeneration temperatures, the vapor compression cycle deals almost the same amount of sensible cooling. This made the further study of SSLC systems focus on comparing the performance of vapor compression cycle

only. The current DW, which had a diameter of 300 mm and an axial width of 100 mm, was not able to deliver the required latent capacity at 45°C regeneration temperature. A larger diameter rotor is required so that a larger amount of air flow can be dried at the same unit rate of dehumidification performance. However, since the independent role of DW in the SSLC system, the vapor compression cycle was still tested in the condition of delivering 45°C regeneration temperature with the assumption that a larger diameter rotor had removed the required amount of latent capacity.

Table 8: Operating conditions tested in the DW experiments

T_{reg} (°C)	$V_{frontal}$ (m/s)	ω (rph)	Q_{lat} (kW)
55	2.11	15	0.7
50	2.46	25	0.7
45	N/A	N/A	N/A

Table 8 provides the DW's rotation speed and air frontal velocity under different regeneration temperatures.

From Figure 31 and Figure 32, it was found that the regeneration temperature and supply air temperature significantly affected the COP. The higher the regeneration temperature, the lower the COP; and the higher the supply air temperature, the higher the COP. Such a trend could be explained by the following: in order to obtain high regeneration temperature, the condensing pressure (high side pressure) of refrigerant had to rise. Such a rise led to two effects: an increased pressure ratio across the compressor and an increased temperature of refrigerant leaving the condenser (gas cooler). Both effects resulted in an increase in compressor power input. On the other hand, an increased air supply temperature raised the

evaporating pressure of refrigerant, which reduced the pressure ratio across the compressor, and led to a reduction in compressor power input. The pressure and temperature profiles in Figure 27 through Figure 30 support the aforementioned statements by demonstrating wide ranges of high side pressure and evaporating pressure.

A computer model was written in an EES platform to simulate the performance of vapor compression cycle using parameters such as compressor efficiency, DW dehumidification capacity, and UA values of heat exchangers. The compressor module was written based on a three-efficiency method, and the three efficiencies were obtained from the tests. The heat exchanger modules were written in a multi-segment UA-LMTD method, with the UA values adjusted so that the refrigerant inlet and outlet conditions calculated from the model matched the experimental results. Performance of the baseline systems, which represented conventional air conditioning systems using evaporators to remove both latent and sensible loads, was calculated by the model based on the same UA values as the SSLC systems, which was used later for the COP comparison on the basis of the same sizes of heat exchangers. The compressors in the baseline systems had the same displacement volumes as those in the SSLC systems. The air flow rate through the evaporator and the evaporator outlet air temperature were calculated to meet the sensible and the latent capacities of the evaporator with the SSLC system capacity. Table 4 shows the comparison results calculated by the model. Since the experimental results demonstrated the low COP performance of vapor compression cycle at 55°C

regeneration temperature, the comparison focused only on the conditions of 50°C and 45°C.

Table 9: COP Comparison between Baseline and SSLC Systems

refrigerant	system	evaporating temperature (°C)	high side pressure (MPa)	regeneration temperature (°C)	COP (improvement)
CO_2	Baseline	13.9	10.37	47.3	2.58 (100%)
	SSLC	17.6	10.91	51.0	2.76 (107%)
		17.7	10.26	45.5	3.40 (132%)
R-410A	Baseline	14.3	3.16	47.3	3.64 (100%)
	SSLC	18.3	3.42	50.7	3.89 (107%)
		18.5	3.03	45.7	4.89 (134%)

Several observations can be made from Table 9. First of all, the baseline COP of the R-410A system was 41% higher than that of the CO_2 baseline system, which again highlighted the low COP behavior of CO_2 systems. Regarding the improvement from the application of SSLC technology, two refrigerants behave very similar to each other. When the regeneration temperature was around 50°C, the COP improvements of both refrigerants were 7%. When the regeneration temperature was around 45°C, the COP improvements were 32% for CO_2 and 34% for R-410A, respectively. Although 45°C regeneration temperature would still be feasible to provide 0.7 kW latent capacity, if a larger DW was used, such improvement should rather be viewed as the best case scenario. The improvement of 50°C regeneration temperature was disappointingly low. While considering the fact that the error bar of COP was around 5%, the worst scenario of improvement would be only 2%. A further study is required to explore larger COP improvement potential of SSLC systems.

2.2.3 Exploration of Better SSLC Systems

The previous chapter brought out the issue that the current SSLC system could not provide as much COP improvement over the baseline system as expected. Two factors have been identified to have a negative effect on the COP of SSLC systems. First, operation of a DW generates heat of adsorption (> 2,500 $kJkg^{-1}$, Gao et al. 2005), which varies according to desiccant material, but is usually higher than the heat of evaporation of water vapor (~ 2,500 $kJkg^{-1}$). The difference of these two forms of heat added an additional heat load to the vapor compression cycle, which reduced the effective cooling from the vapor compression cycles. Test data indicated that the extra heat load was around 300 W, with the resulting effective cooling at 3.2 kW and the COP of SSLC systems reduced by 8%. Second, in order to provide the regeneration temperature of 50°C, the airflow rate through the condenser (or gas cooler) needs to be reduced from 0.37 m^3s^{-1} (baseline system) to 0.25 m^3s^{-1}. Such a reduction raised the condensing pressure (high side pressure) of both refrigerants. As described in Table 4, the high side pressure of CO_2 increases from 10.37 MPa to 10.91 MPa, and the condensing pressure of R-410A increases from 3.16 MPa to 3.42 MPa. Excessive high side pressure increases the compressor input and in turn decreases the COP.

The first negative factor is difficult to eliminate because it results from the inherent characteristic of desiccant material. However, the impact of the second factor could be minimized. We hereby propose the application of divided condensers (or gas coolers). Instead of heating the entire amount of air through a heat exchanger, (referred to in this dissertation as a condenser or gas cooler) to a required regeneration

temperature, divided heat exchangers use only one section (the first section) to provide hot air for DW regeneration, while the other sections (second section or third section) are used for heat rejection only, without meeting the temperature requirement for regeneration. Therefore, the refrigerant high side pressure is restrained while the system is still able to effectively regenerate the DW. Furthermore, as a common practice to improve the performance of the CO_2 cycle, the addition of a suction line heat exchanger helps reduce the refrigerant temperature at the gas cooler outlet. Therefore, its integration with the SSLC system was also investigated.

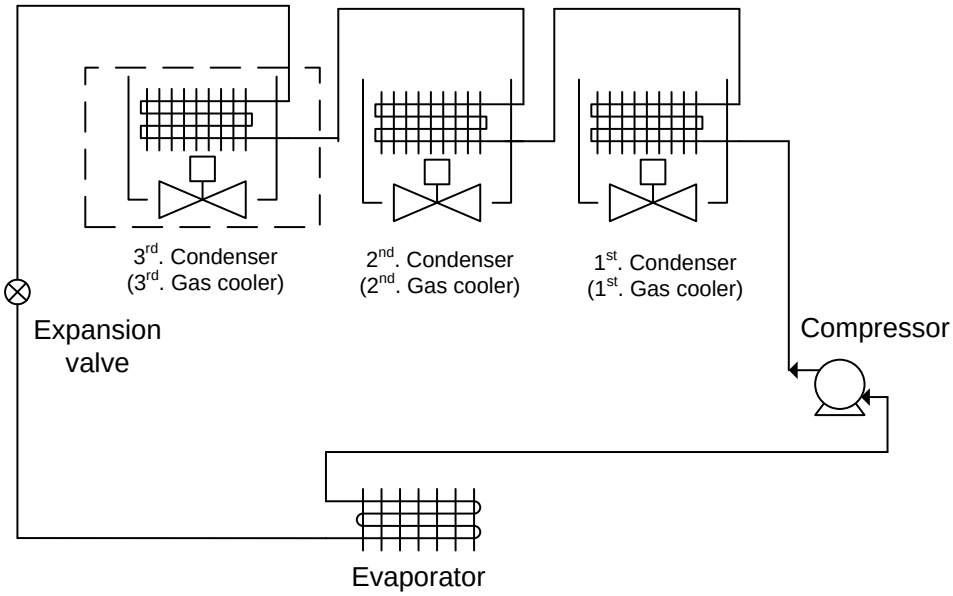

Figure 33: The refrigeration cycle of the DW-assisted SSLC system with divided HXs

Figure 33 describes the refrigeration cycle of the new SSLC system with divided heat exchangers (HXs). The condenser (gas cooler) in the vapor compression cycle was divided into two or three sections. The refrigerant that discharged from the compressor entered the first part of the condenser (or gas cooler), and then entered the second and third parts in sequence. The ambient air flowing to the first part of the heat exchanger was sent directly to the DW for regeneration. The ambient air or

exhaust air from the space served as a heat sink for the refrigerant in the second and third parts of the heat exchanger, after passing through the evaporative cooling process. The refrigerant leaving from the third part was sent to the expansion device. Some of the options listed below do not have the third part heat exchanger, which is shown in dashed rectangular box, so the refrigerant leaving the second part heat exchanger was sent to the expansion valve directly.

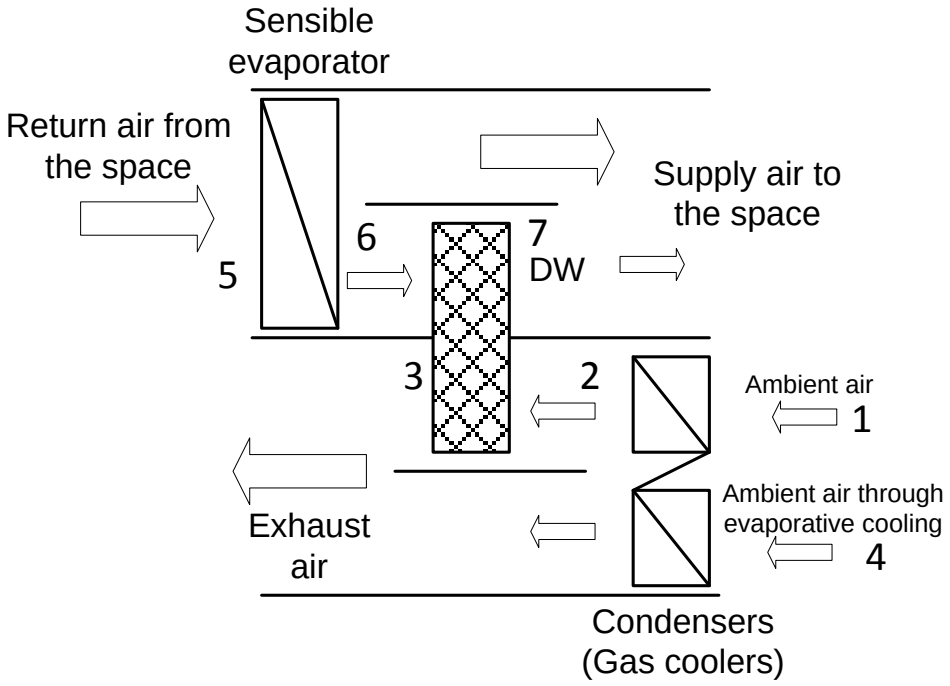

Figure 34: New DW-assisted SSLC system option 1: evaporative cooling

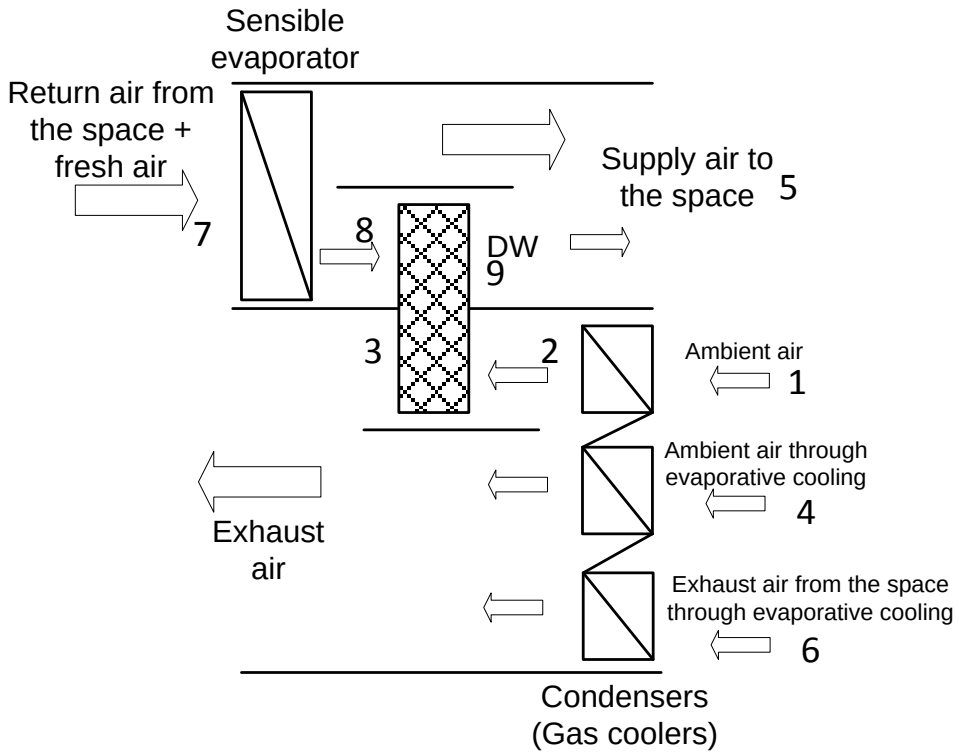

Figure 35: New DW-assisted SSLC system option 2: evaporative cooling + fresh air

Both Figure 34 and Figure 35 describe the DW-assisted SSLC systems. Option 1 is a zero-ventilation system, and the condensers (or gas coolers) was divided into two parts. Option 2 has the required amount of fresh air for the capacity, and the condensers (or gas coolers) were divided into 3 parts. Each part faced different air conditions, which varied from the ambient condition (35°C, 44% RH), ambient air condition after the evaporative cooling process (24.8°C, 100% RH) to the exhaust air from the space after the evaporative cooling process (19.5°C, 100% RH).

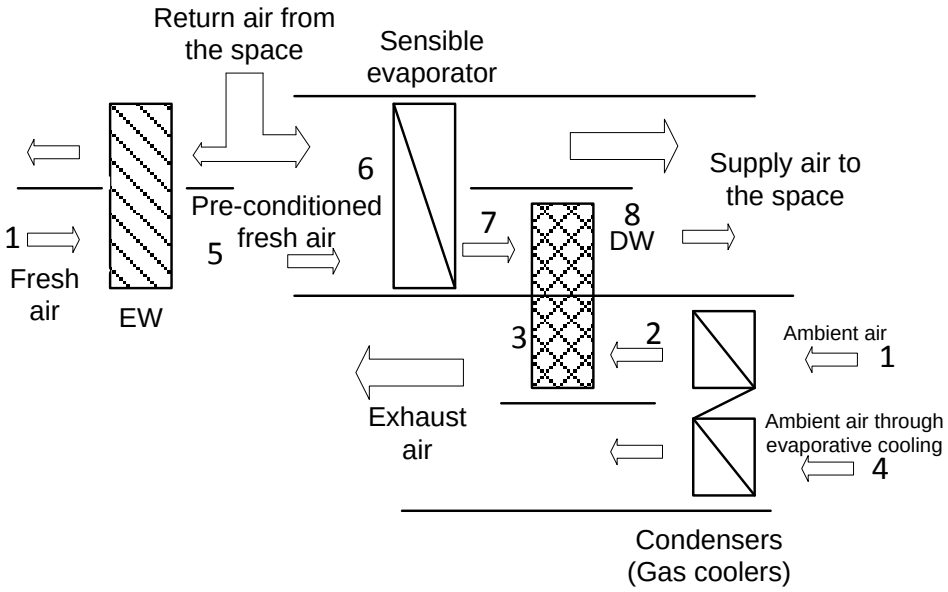

Figure 36: New DW-assisted SSLC system option 3: EW + evaporative cooling + fresh air

Figure 36 shows the option with an added enthalpy wheel (EW) into the system. The heat and mass transfer between hot-and-humid ambient air and cool-and-dry indoor exhaust air helped recover both the sensible and latent cooling from the space.

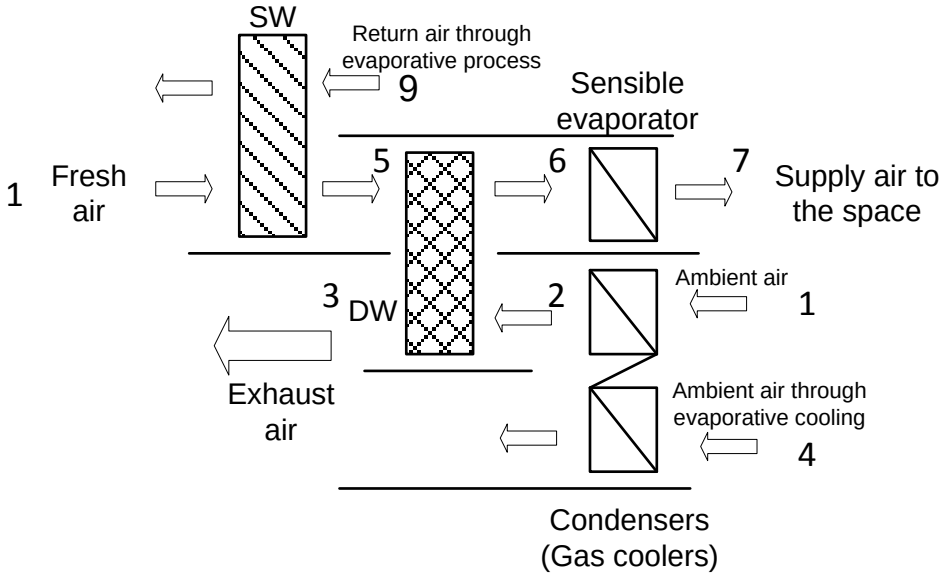

Figure 37: New DW-assisted SSLC system option 4: SW + evaporative cooling + DOS application

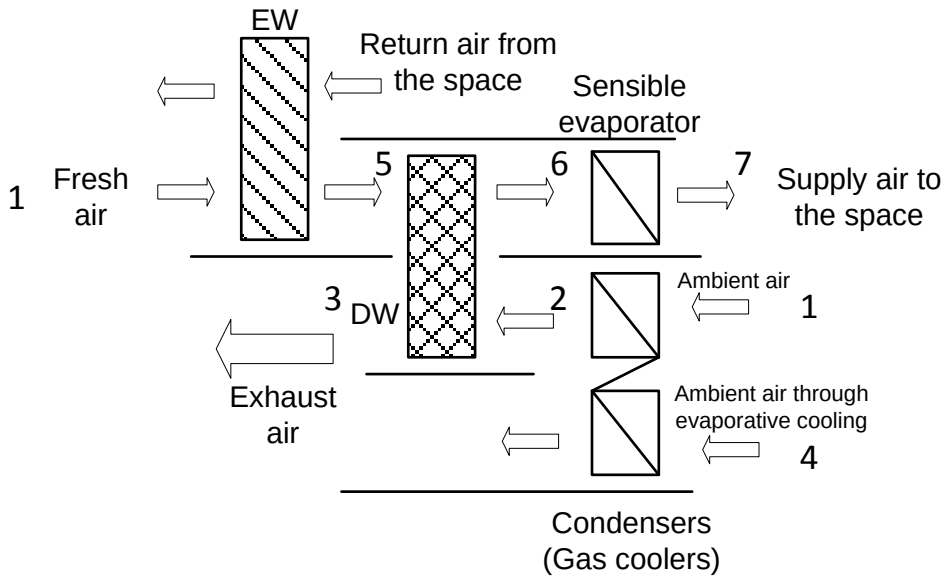

Figure 38: New DW-assisted SSLC system option 5: EW + evaporative cooling + DOS application

Figure 37 and Figure 38 describe two new applications for such a configuration on a dedicated outdoor system (DOS). In the DOS, only fresh air is pre-conditioned to such a level that the temperature and humidity ratio are the same as those of the indoor air. Moreover, the application of the enthalpy wheel (EW) and the sensible wheel (SW) were compared to each other in order to find out which component is more suitable for the DOS. In the configuration of SW, one of the air streams was outside fresh air and the other was return air after the evaporative cooling process. Since there was only sensible heat transfer through the wheel, the evaporative cooling provided a large heat recovery potential without adding any water vapor to the fresh air stream. On the other hand, in the configuration of EW, no evaporative cooling process was added.

2.2.4 Improved System Modeling Approach

EES was again used to model the vapor compression cycle and the DW. CoilDesigner (Jiang, 2006), an in-house heat exchanger simulation software package, replaced the previous multi-segment UA-LMTD method to model all the heat exchangers in the vapor compression cycle. The built-in optimization tool in EES was utilized to optimize the system COP. The detailed assumptions adopted for calculating the vapor compression cycle are listed as follows:

The integration between EES and CoilDesigner: For each heat exchanger calculation, a database was created by a multiple-variable parametric study in the CoilDesigner. Specifically, the database of evaporator (evaporating pressure, inlet quality and mass flow rate) were selected as variables, and for the database of condenser (gas cooler) (condensing pressure (gas cooling pressure), inlet temperature, and mass flow rate) were selected as variables. Each database had 1,000 records. EES imported all the records and saved them in 3-dimension arrays. Linear interpolation method was applied to calculate the results from the database records.

Optimization approach: The EES built-in optimization tool was used to maximize the system COP. Because of the nature of the system model, which was non-linear and the possible existence of multiple local maximums, the genetic method was applied for the optimization. The optimization function was defined as,

$$\text{Min } f = -(\text{COP of the system}) \tag{34}$$

s.t. :

system capacity≥3,800 W (SSLC system) or 1,820 W (DOS system)

Air discharge temperature off the 1st condenser (GC) ≥50°C

The normalized objective function with penalty factor was demonstrated below,

$$f=-\frac{COP}{\text{baseline COP}}+rp*\left(\max\left(\frac{-Qeva+3800(1820)}{3800(1820)},0\right)+\max\left(\frac{-t_{airoff}+50}{50},0\right)\right) \quad (35)$$

where: *Baseline COP* = 3, *rp*(penalty factor) = 1,000

The following assumptions were made for modeling the vapor compression cycle:

- System capacity: 3.5 kW (SSLC), 1.82 kW (DOS) (smaller capacity because it only conditions ventilation air flow)
- Sensible heat factor: 0.7
- Latent capacity: 1.0 kW
- Outdoor/indoor air conditions: 35°C, 44% RH / 27°C, 50% RH
- Refrigerant: R-410A and CO_2
- Regeneration temperature: 50°C
- Regeneration air flow rate: 0.15 m^3/s
- Indoor air flow rate: 0.41 m^3/s
- Ventilation air flow rate or air flow rate of DOS system: 0.082 m^3/s
- Total air flow rate of condensers (gas coolers): 0.42 kg/s (volume flow rate varied in the condition with or without evaporative cooling)

Compressor modeling: The compressor's discharge temperature and power input were calculated from isentropic efficiency, compressor efficiency and volumetric efficiency. The three efficiencies were functions of pressure ratio, degree of superheating, and compressor frequency. Theoretical work input and the functions were obtained by regression analysis on experimental data.

$$\eta_{ise}=f_1(PR, T_{sup})=\frac{h_{dis,ise}-h_{suc}}{h_{dis}-h_{suc}} \quad (36)$$

$$\eta_{vol}=f_2(PR,T_{sup},compfreq)=\frac{\dot{m}}{RPM*disp*\rho_{ref}} \quad (37)$$

$$\eta_{comp}=f_3(\text{theoretic work input})=\frac{\text{theoretic work}}{\text{real work}} \quad (38)$$

HX modeling: all the heat exchanger calculations were conducted in CoilDesigner.

Expansion device modeling: The expansion process in the vapor compression cycle was treated as isenthalpic.

$$h_{in}=h_{out} \quad (39)$$

DW modeling: The DW was also modeled in the EES. The dehumidification performance was assumed to be a function of DW rotation speed, regeneration temperature, air velocity through the wheel and inlet humidity ratio in the regeneration side. The enthalpy of air in the process side off the DW was calculated as a function of DW rotation speed, regeneration temperature and air velocity. All the input data described above were from experimental data.

$$WVR=f_4(T_{reg},RPH,V_{air},\omega_{regin}) \quad (40)$$

$$h_{gain}=f_5(T_{reg},RPH, V_{air}) \quad (41)$$

SW and EW modeling: both of them were treated as counter-flow heat exchangers in modeling. A free heat exchanger software package (Heatex Select, 2009) was used to calculate the efficiencies of both wheels. For the SW, since the sensible heat was

transferred between two air streams, the sensible heat transfer efficiency was defined to be 0.85. For the EW, both sensible and latent heat were transferred between two air streams, and the efficiencies of temperature (sensible heat) transfer and humidity (water vapor) transfer were defined to be 0.82 and 0.65, respectively.

2.2.5 Modeling Results and Discussion

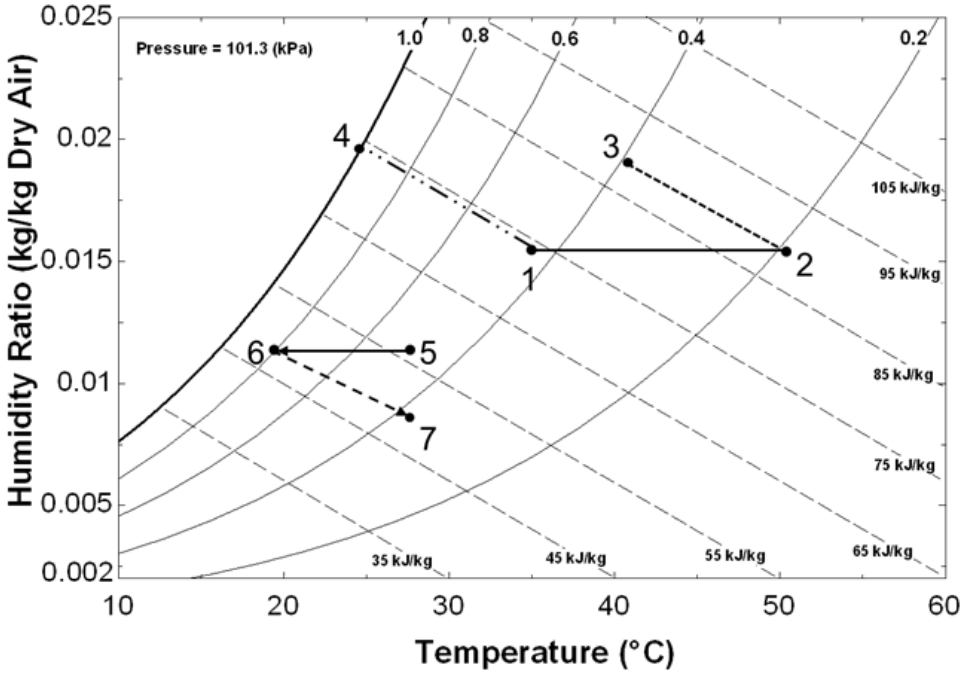

Figure 39: Psychrometric process of new SSLC system option 1

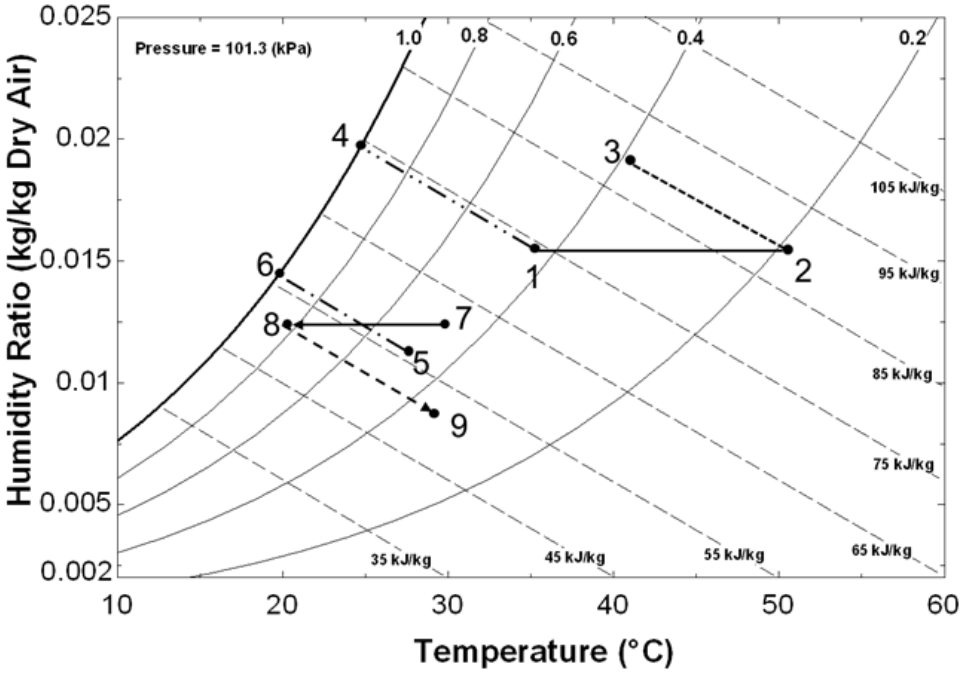

Figure 40: Psychrometric process of new SSLC system option 2

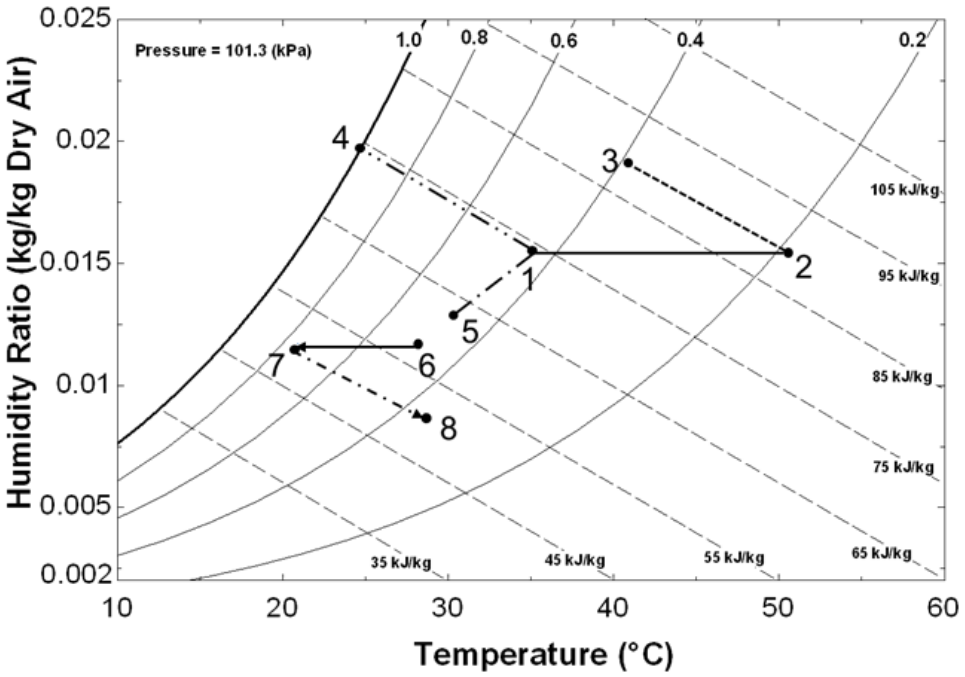

Figure 41: Psychrometric process of DW-EW-assisted SSLC system (option 3)

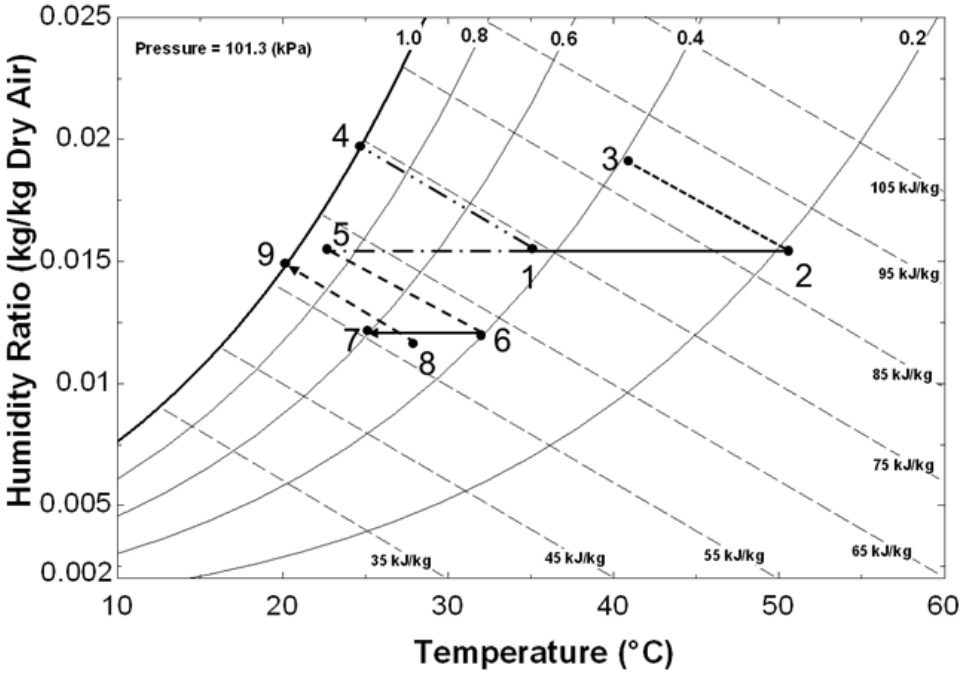

Figure 42: Psychrometric process of DW-SW-assisted DOS system (option 4)

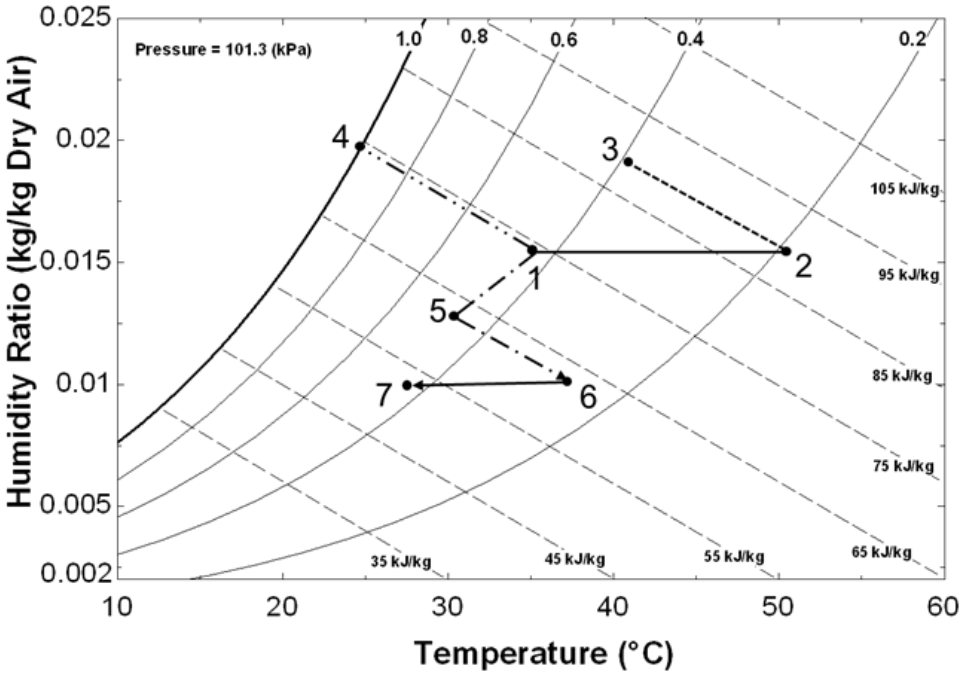

Figure 43: Psychrometric process of DW-EW-assisted DOS system (option 5)

Figure 39 through Figure 43 demonstrate the psychrometric processes of the aforementioned options. Different line styles represent different air processes. In those figures, the bold numbers represent each air state point corresponding to ones in their respective schematic drawings.

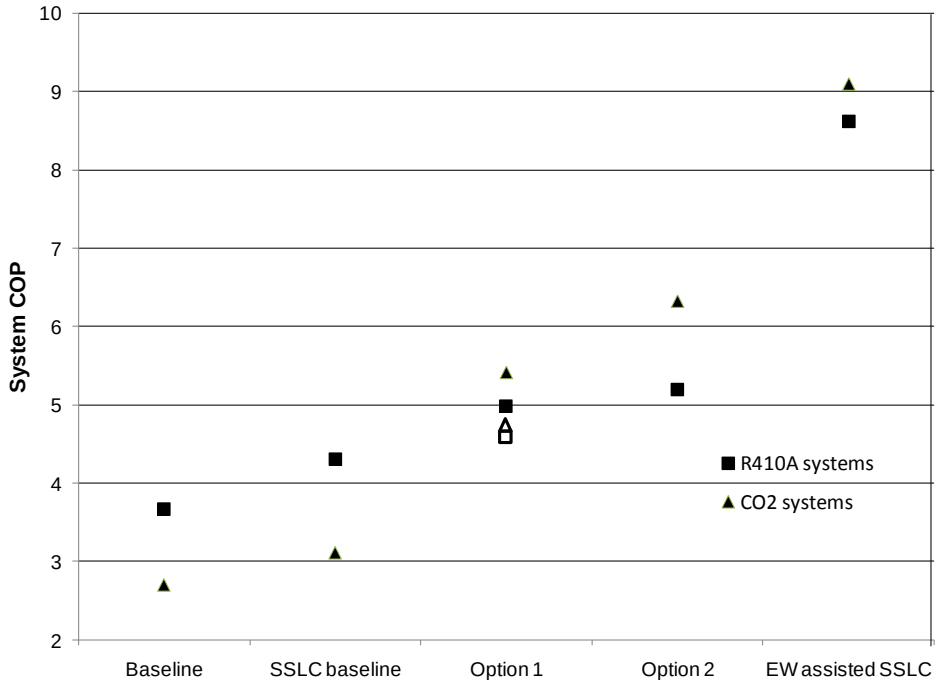

Figure 44: The system COP comparison of different SSLC options and baseline system

In Figure 44, the system COPs of different options were compared with the convectional systems and DW-assisted SSLC system with single condenser (gas cooler). The system COP was defined as the ratio of the space cooling capacity (3.5 kW) to the compressor input. For conventional systems, the system COP could be considered same as the vapor compression cycle COP when neglecting heat load of fans, which is defined as the ratio of the evaporator air-side capacity to the compressor input. However, for the DW-assisted SSLC system, the vapor compression cycle provided an extra 300 W cooling to compensate for the difference

of heat of adsorption and heat of evaporation. After conducting the optimization, both the previous conventional systems and DW-assisted SSLC systems had slight improvements. In the conventional systems, the system COP of R-410A system improved from 3.6 to 3.7 and the system COP of CO_2 system improved from 2.6 to 2.7. For the SSLC systems with single condenser (gas cooler), R-410A system improved from 3.9 to 4.1 and CO_2 system improved from 2.8 to 2.9.

All these system COP results were plotted in Figure 44. In order to demonstrate the effect of the application of divided heat exchangers, the CO_2 vapor compression cycles were plotted in the P-h diagram as shown in Figure 45.

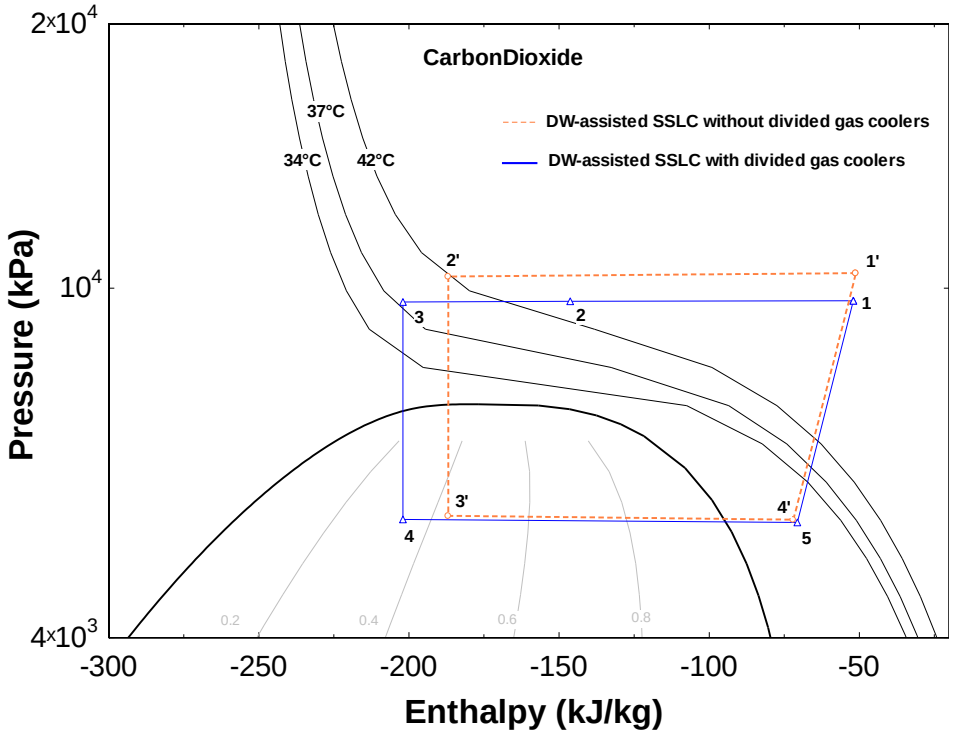

Figure 45: P-h diagram of CO_2 DW-assisted SSLC systems

(1': compressor outlet, 2': gas cooler outlet, 3': expansion device outlet, 4': evaporator outlet
1: compressor outlet, 2: 1st gas cooler outlet, 3: 2nd gas cooler outlet, 4: expansion device outlet, 5: evaporator outlet)

The dotted cycle represents the DW-assisted SSLC system without gas cooler being divided, and the solid cycle represents the one with divided gas coolers. It clearly shows that the application of divided heat exchangers reduce the high side pressure and also reduce the approach temperature. In more detail, the divided gas coolers reduce the high side pressure from 10.4 MPa to 9.7 MPa, and the refrigerant temperature off the gas cooler is reduced from 42°C to 38°C. For the R-410A system, the pressure reduction is insignificant (3.46 MPa to 3.45 MPa); however, the condenser outlet temperature reduction is significant (from 40°C to 36 °C). The hollow legends in Figure 44 represent the case of option 1 without evaporative cooling in the second HX. It was found that the COP improved by 20% for the R-410A system and 44% for the CO_2 system. It is also interesting to notice that when the evaporative cooling is applied to the second gas cooler (solid legends); the CO_2 system had a better COP than the R-410A system. The COP of the CO_2 systems tends to decrease quickly under high ambient temperature conditions; however, the application of the evaporative cooling lowered the actual operating conditions of the system. Therefore, the COP improvements of the CO_2 systems were larger than those of the R-410A systems. Option 2 divides the condensers (gas coolers) into three parts, and the evaporative cooling of return air provides the lowest possible temperature to further cool down the refrigerants. The COP had an extra 4.8% and 16.8% improvement for the R-410A and CO_2 systems, respectively. Again, the CO_2 system outperformed the R-410A system because the same reason explained above. The EW-assisted SSLC system had the highest COP as shown in Figure 44. Application of the EW provided “free” sensible and latent cooling, and reduced the sensible cooling

requirement of the vapor compression cycle from 3.8 kW to 2.7 kW. The heat exchangers were modeled in reduced sizes in proportion to the reduced capacity. The compressor power input was reduced to a minimum with this option. The system COP improvements were 68% and 73% for the CO_2 and R-410A systems, respectively.

Table 10: Optimization results of SW-DW-assisted SSLC system

Refrigerant	R-410A	CO_2
Vapor compression cycle COP	5.09	3.64
Cooling capacity of VCC (kW)	1.25	1.25
Power input (kW)	0.24	0.34
Regeneration temperature (°C)	48.21	48.19
The ratio of heating to cooling	1.12	1.12
Sensible wheel capacity (kW)	1.27	1.27
System cooling capacity (kW)	1.82	1.82

Table 10 lists the optimization results of the SW-DW-assisted DOS system. The vapor compression cycle COP is defined as the ratio of cooling provided by the VCC over the VCC power input. Unlike aforementioned system COP which adds the cooling effect from cooling recovery device, like EW or SW, the VCC COP only considers the cooling from VCC system. For both refrigerant systems, the most important information was that they could not provide enough heat (to reach 50°C) to regenerate the DW. The table shows the maximum regeneration temperatures are only around 48°C for the two systems. Since the SW did not provide any latent cooling, the DW had to deal with the entire latent load (1 kW). However, the vapor compression cycle had a reduced cooling capacity (from 1.8 kW to 1.25 kW), enhanced by the fact that the SW provided a sensible cooling. Compared with the required amount of heat to regenerate the DW (1.4 kW), the reduced cooling capacity

output from the vapor compression cycle was too small to maintain the COP at a high level while still rejecting enough heat to the ambient air. If the system was forced to deliver the required amount of heat to the DW, the system COP would be lower than the conventional system, rendering ineffective the point of using the separate sensible and latent cooling technology. The EW-DW-assisted system, on the other hand, worked well.

Table 11: Optimization results of EW-DW-assisted SSLC system

Refrigerant	R-410A	CO_2
Vapor compression cycle COP	5.80	4.54
Cooling capacity of VCC (kW)	0.80	0.81
Power input (kWe)	0.14	0.18
Regeneration temperature (°C)	50.06	50.01
The ratio of heating to cooling	0.95	0.95
Enthalpy wheel capacity (kW)	1.32	1.32
Latent capacity of EW (kW)	0.65	0.65
System cooling capacity (kW)	1.82	1.82

Table 11 lists the optimization results of such a system. The EW provided both the sensible and latent cooling to the system, helping to reduce both the cooling load of the vapor compression cycle and the amount of heat required to regenerate the DW. When comparing the cases of using an EW against using a SW, it was found that the ratio of heating to cooling could serve as a measure to determine whether or not the configuration was suitable for the DW-assisted SSLC system. If the ratio was greater than 1, meaning the heat requirement of the regeneration is greater than the

cooling output of the vapor compression cycle; such a configuration would not be suitable because the regeneration heat from the cooling system is not large enough.

Chapter 3: Experimental Assessment for the Low ΔT Heat Exchangers

3.1 Chilled Ceiling Panels, Heated Floor Systems and the Low ΔT Heat Exchanger

In order to assess the thermal comfort provided by the SSLC system, it is necessary to focus the study onto its indoor heat exchanger. The previous study shows that one of the major design challenges for the indoor heat exchangers is larger air-side pressure drop than that of conventional ones. It is because the air flow rate through the sensible heat exchangers has to be typically 3 to 4 times higher than that that through conventional systems in order to compensate the reduced air enthalpy difference across the heat exchanger. As a solution to this challenge, the indoor heat exchangers are designed to have a larger frontal area; so that the air velocity can be reduced. The larger frontal area has another advantage. It makes the radiative heat transfer between the heat exchanger and occupants more significant than that of conventional systems. Such heat transfer helps to adjust the mean radiant temperature (MRT), and hence provides better thermal comfort. In some European and Asian countries, the idea has been applied to products like chilled ceiling panels (cooling) and heated floor systems (heating).

Chilled ceiling panels are typically suspended on the ceiling or plenum which refers to a drop ceiling. The panels consist of one or multiple serpentine-shaped tubes fixed on metal sheets. The tubes can be made of copper because of a better heat conductance so that the heat from the tube can be better transferred to the sheet. However they are more often made of PEX, cross-linked polyethylene**,** for the easy

handling and lower cost. The metal sheet is typically made of aluminum. Paint may be applied on the surface for a better emissivity. The working fluid flowing inside the tubes is water which is in the temperature range from 14°C to 18°C. Since condensation should be avoided, the fluid temperature has to be 1 or 2 K higher than the dew point. Therefore, for the entire air-conditioning application, certain latent load removal system has to be installed such as desiccant wheels. Riffat et. al. (2004) provides a detailed review on the origination, development and current state of the chilled ceiling panels.

The heated floor system instead provides hot water inside the tubes which are embedded under floors. The two papers from Bean et al. (2010a, 2010b) offer a review of the development of heated floor systems in both Asia and Europe. It is widely accepted that both the chilled ceiling panels and heated floor systems have the benefits of low energy consumption and better thermal comfort.

However, there are drawbacks to these two systems. First of all, as restricted by the motion of buoyancy airflow, chilled ceiling panel cannot effectively provide heating while heated floor system cannot effectively provide cooling. Therefore, each system cannot replace the other with the same function. Second, especially for the heated floor systems, the installation requires an entire overhaul of the floor in order to embed the system. Such overhaul work is almost impossible without affecting the residents. Therefore, the systems are generally limited to be installed for new houses. However, considering the fact that in the US, the number of retrofitting old houses is

at least three times more than that of building new homes, it is obvious that the market for these two systems are low.

The idea of low ΔT heat exchanger is proposed hereby in order to address the above two drawbacks. The low ΔT refers to the small temperature difference between indoor air and refrigerant, i.e., in winter the low ΔT heat exchanger uses hot fluid of temperature just several degrees higher than room air temperature to provide heating; and in summer it uses cold fluid of temperature just several degrees lower than room air temperature to provide cooling. The structure of the heat exchanger is similar to chilled ceiling panels. It consists of serpentine tubes and metal sheets. However, unlike the installation of a chilled ceiling panel which has to be suspended on the ceiling, the low ΔT heat exchanger can be hung on the wall. It also has a large frontal area that can cover as much as the entire wall or even multiple walls so it can effectively provide radiative heat transfer as well as convective heat transfer. Since the heat exchanger can be installed on the wall, the temperature difference between the heat exchanger wall and the opposite wall will drive a ring-shape air motion due to natural convection. Hence, there is no restriction for it to provide both heating and cooling. Moreover, the installation of heat exchanger against the wall is much more convenient. It does not require any overhaul to the existing structure of the house. The convenience makes it possible to apply the low ΔT heat exchangers and low temperature lift heat pump systems onto retrofit market.

In order to test the performance of the low ΔT heat exchangers and to prove the potential for better thermal comfort, a series of experiments have been conducted.

The experiments started with the fabrication of operative temperature sensor, followed by a baseline system test, and finally the test of low ΔT heat exchangers.

3.2 Sensors for Operative Temperature Measurement

3.2.1 A Simplified Operative Temperature Calculation

According to Eq. (1), the operative temperature is defined as the heat transfer coefficient - weighted arithmetic mean between air temperature and (MRT). However, the direct measurement of either radiative heat transfer coefficient or convective heat transfer coefficient is cumbersome; hence proper simplifications to the equation have to be made. Table 12 lists a simplified calculation method by ASHRAE standards 55 (ASHRAE 2004). It is assumed that (1) convective heat transfer coefficient depends on air velocity; (2) when the velocity is small, the convective heat transfer coefficient is comparable to the radiative heat transfer coefficient.

Table 12: Operative temperature calculation (based on ASHRAE 2004)

Air speed	$v < 0.2$ m/s	$0.2 \leq v \leq 0.6$ m/s	$v > 0.6$ m/s
Correlation	$t_{op}=0.5T_{air}+0.5MRT$	$t_{op}=0.6T_{air}+0.4MRT$	$t_{op}=0.7T_{air}+0.3MRT$

3.2.2 Operative Temperature Sensors

The operative temperature (OT) is measured with self-built sensors. The sensors are designed according to the ISO standard 7726 (ISO 7726:1998), which provides a guideline for OT sensor's design. Each one consists of a resistive temperature sensor (RTD), which has an uncertainty of ± 0.15 K, inserted into the center of a hollow aluminum sphere. The sphere of 0.152 m in diameter was welded from two halves and polished on the outer surface. Multiple layers of black paint having an emissivity of 0.95 were then uniformly applied on the polished surface. The emissivity of 0.95 is selected because it is close to the emissivity of a human body. Figure 46 and Figure 47 are the pictures of the RTD sensor and the assembled operative temperature sensor, respectively.

Figure 46: Picture of RTD sensor

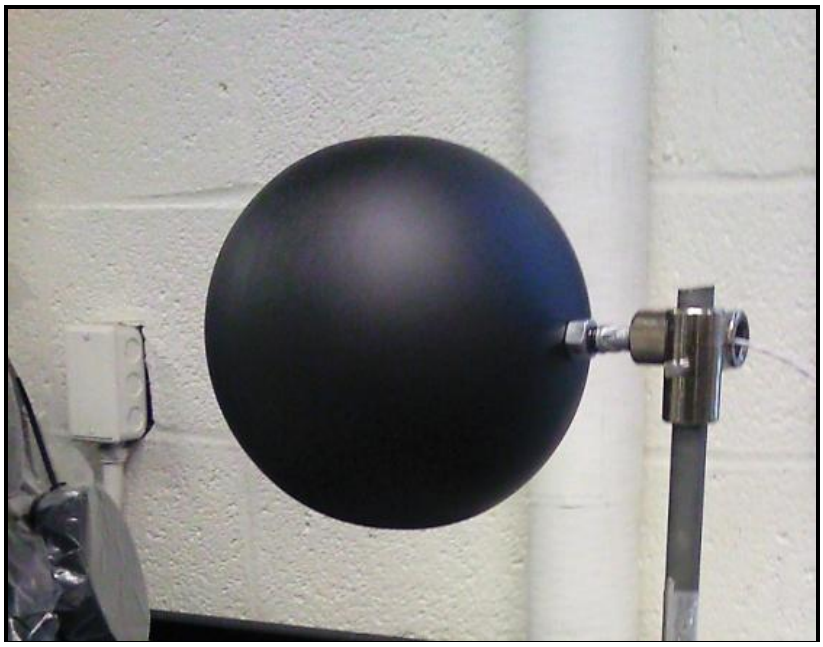

Figure 47: Picture of assembled operative temperature sensor

The four assembled operative temperature sensors were later attached to a vertically-placed pole at different heights. Figure 48 provides detailed positions of the four sensors. The selection of the different positions is based on the height of an ordinary person so that different sensors can record the operative temperature from the feet to the head. The RTD sensors are calibrated at both 0°C and 100°C. Figure 49 plots the operative temperature readings of four sensors in one day. OT 1 is located at 1.7 m, OT 2 is located at 1.1 m, and OT 3 and OT 4 are located at 0.6 m and 0.1 m, respectively. Because the average temperatures of exterior wall (21.9°C) and floor (23.6°C) is much colder than air temperature in the room (25.1°C), it resulted in lower MRT. Therefore, the OT sensor readings are lower than air temperature. Since OT 1 has the largest view factor to the exterior wall, followed by OT 2, consequently, the OT sensors readings are low. OT 3 has the least view factors to the exterior wall and floor, therefore the reading is highest. In Figure 50, the uncertainties of the sensors (error bars) are applied to the average values of data in Figure 49. Both

systematic error and random error were considered in the uncertainty analysis. The highest uncertainty, ±0.36 K, came from OT 1, and the lowest uncertainty, ±0.30 K, came from OT 3.

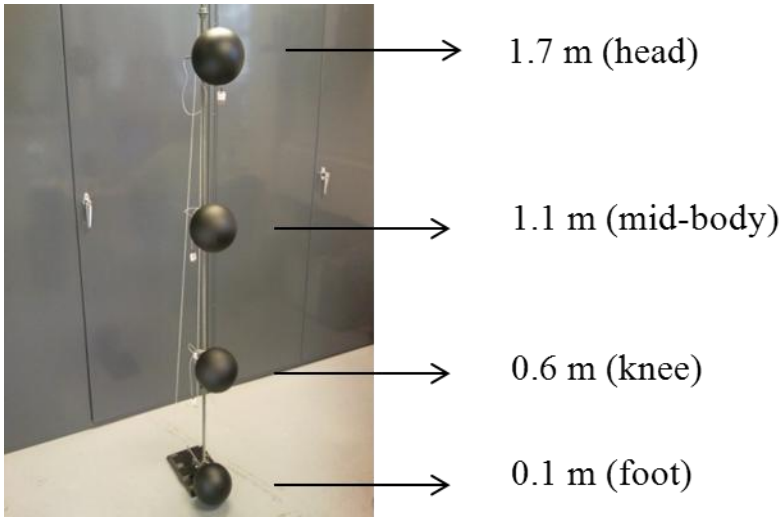

Figure 48: Positions of four operative temperature sensors

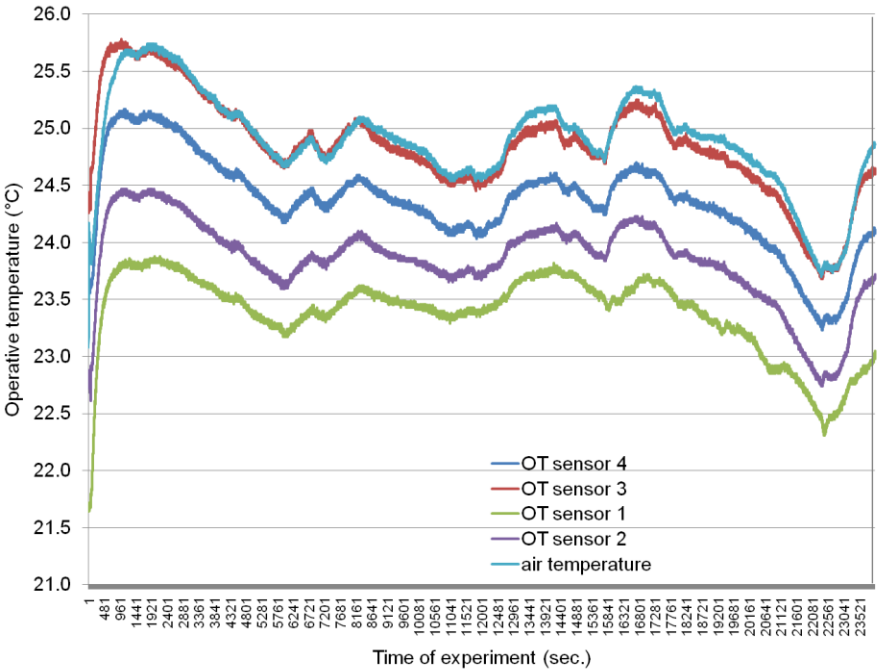

Figure 49: OT sensors readings in one day

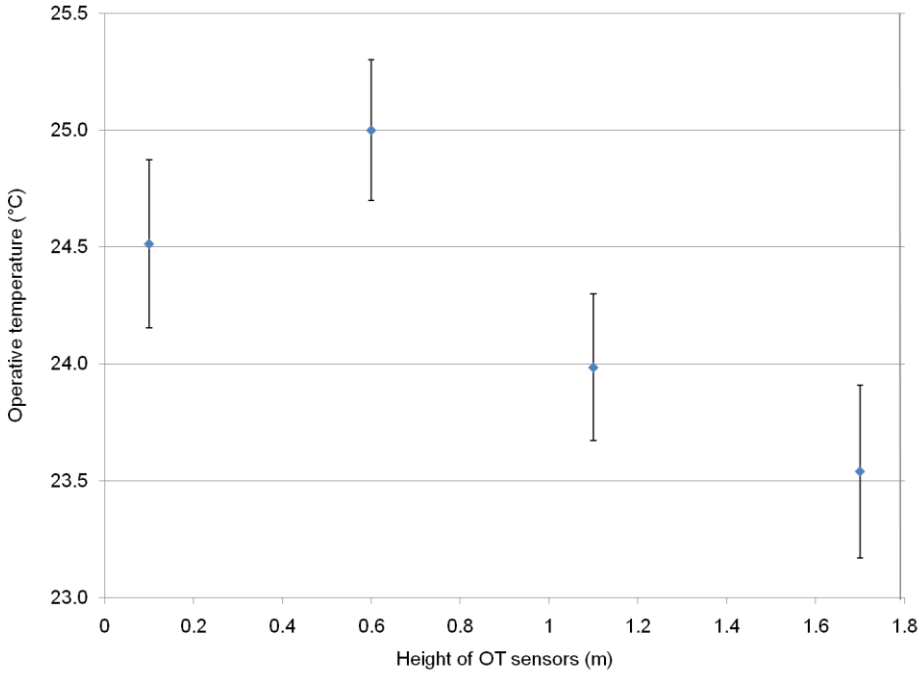

Figure 50: Uncertainty analysis of operative temperature sensors

3.3 Low ΔT Heat Exchanger Test Facility

3.3.1 The Hot Water Supply Loop

Figure 51 describes the hot water supply loop for the low ΔT HX test facility. A tank made of polypropylene panels is used as a reservoir for hot water. The water inside the loop is circulated by a Grundfos® circulator pump. The pump, having a 205 W power input, is capable of delivering 1.77 l s^{-1} water flow rate at zero pressure lift or 90 kPa pressure lift at zero flow rate. A 1,500 W electric heater was installed in the loop to reheat the water. The heater came with an analog manual temperature control dial but was later replaced with a solid state relay to achieve a better on and off control. The relay itself is controlled by the PID module of the data acquisition system. The components were connected together by PEX tubes.

Three T-type thermocouples (systematic error of ± 0.5 K) were installed at different locations to obtain an energy balance between the heater output and the heating capacity of the low ΔT heat exchangers. The detailed positions of these thermocouples are marked in the Figure 51. The water mass flow rate in the loop was measured by a MicroMotion® Coriolis mass flow meter. The mass flow meter was re-calibrated to a range of 25 to 100 g/s for a better accuracy of 2.5% reading. Finally, the water flow rate was adjusted through a needle valve to achieve the capacity control of the heat exchangers.

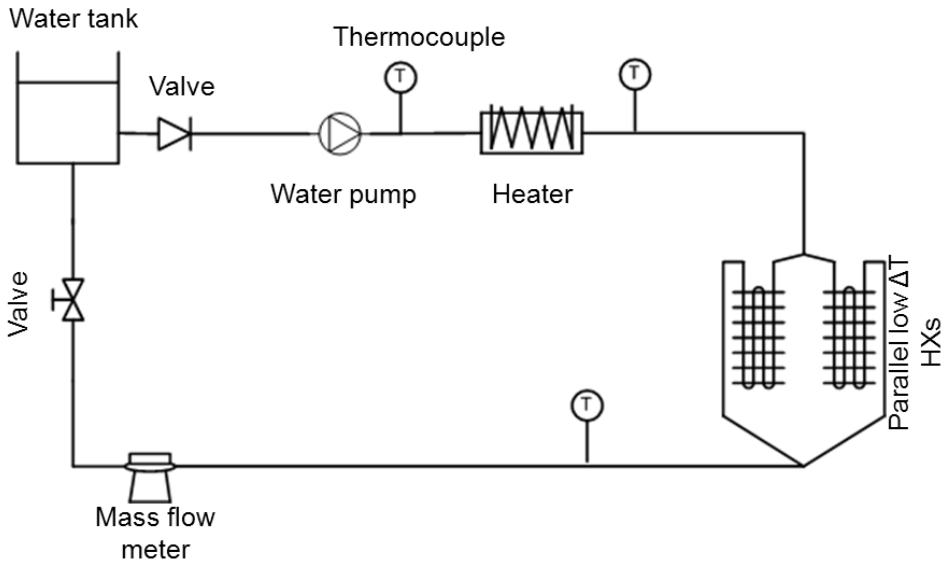

Figure 51: Schematic diagram of low ΔT HX test facility

3.3.2 The Assembly of Low ΔT Heat Exchanger Panels

Two low ΔT heat exchanger panels (which are called comfort panels in the catalog) were purchased from Uponor®. The heat exchangers consist of 60 aluminum sheets and PEX tubes of a total length of 75 m. Each sheet has a smooth back-side, but its front-side is divided into small channels so that the PEX tube can be clipped into channels in a serpentine shape. The dimension of each sheet is 1.22 m by 0.089 m. 34 sheets were combined together to make one heat exchanger, while the rest 26 sheets were combined together to form another one. Insulation foams were taped to fill the gaps between channels in order to prevent conduction loss (see Figure 52). The total frontal area of the two heat exchangers is 6.52 m^2. According to the Uponor® catalog (Uponor, 2010), it should be able to provide up to 658 W cooling/heating. The capacity was determined by a maximum capacity output of 101

W/m^2 at 11 K temperature difference. The amount of cooling/ heating is sufficient to cover the heating/cooling load in the test office (Koepke 2011).

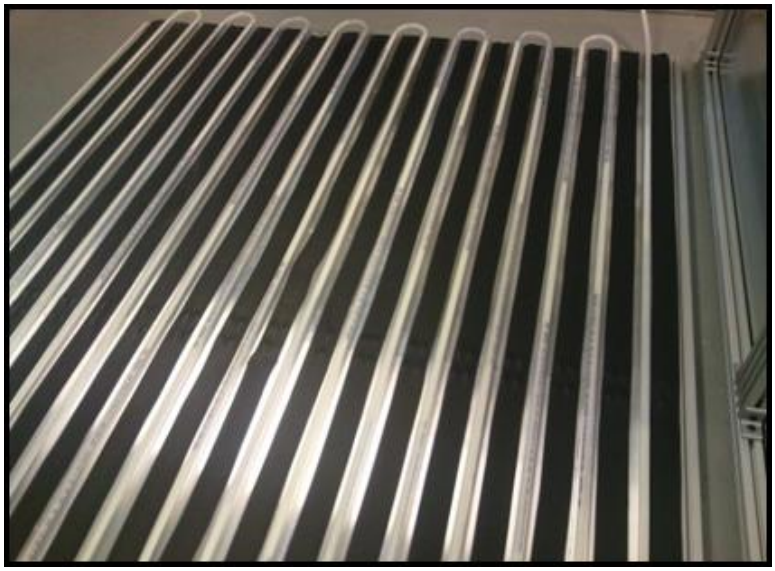

Figure 52: Low ΔT HX's sheet and tube

To minimize the heat loss from the back, insulation foams of fiberglass were applied to the backside of the sheet. The applied foam has a thickness of 3.8 cm and a thermal conductivity of 0.042 $W(m \cdot K)^{-1}$ (see Figure 53).

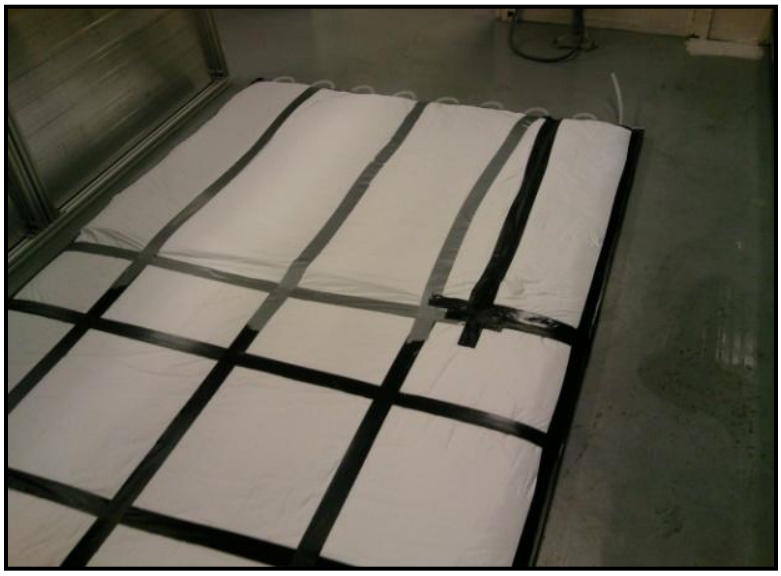

Figure 53: Insulation for the backside panel of low ΔT HX

Due to the restriction of office layout, the heat exchanger can only be installed on the north wall opposite to the window. The heat exchangers were assembled together by aluminum frames. The frame was made of 80/20® aluminum profiles with a side length of the square cross section of 0.0381 m. The total frame size per panel is 1.6 m × 2.44 m. They were connected together by aluminum angles. Figure 54 is the picture of the final installation of low ΔT heat exchangers inside the test office.

Figure 54: Installed panels in the test office

3.3.3 Room Selection

Among various criteria, the most important one for room selection is that its dimension should be as close as possible to that of the CFD model (3 m by 3 m). The CFD modeling will be discussed in detail in the following chapter. Based on this criterion, an office on the first floor of Potomac Building at College Park, MD campus was selected. The office is 2.95 m from north to south, 4.25 m from west to

east and 3.2 m in height. It has one frequent occupant, a desk, a chair, two cabinets, one PC, two monitors and two fluorescent ceiling lights. Table 13 shows the breakdown of components included in the load calculation. Figure 56 and Figure 57 demonstrate the results of load calculation for winter and summer, respectively.

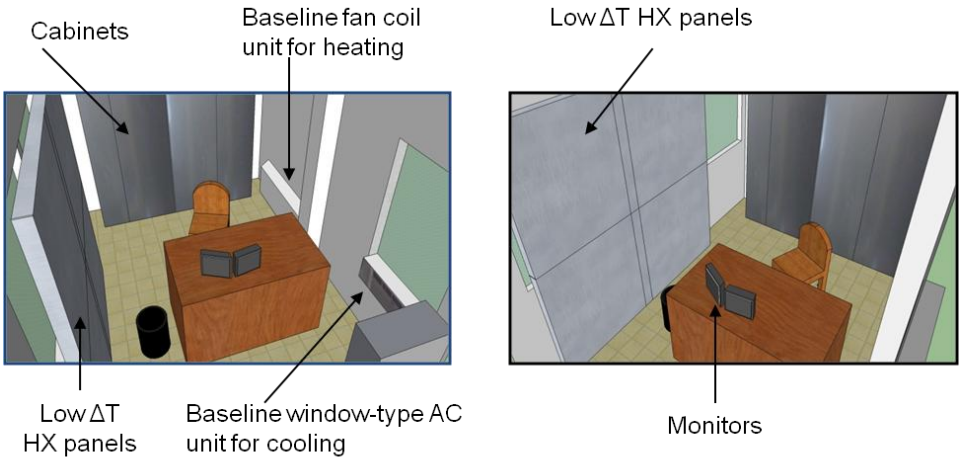

Figure 55: Sketch of the office under low ΔT study

Table 13: Load calculation components

Load Components	Summer	Winter
Exterior walls	Heat gain	Heat loss
Exterior windows	Heat gain	Heat loss
Interior walls	Heat gain	Heat loss
Lighting	Heat gain	Heat gain
Electronic appliances	Heat gain	Heat gain
Occupants	Heat gain	Heat gain
Ventilation	Heat gain	Heat loss

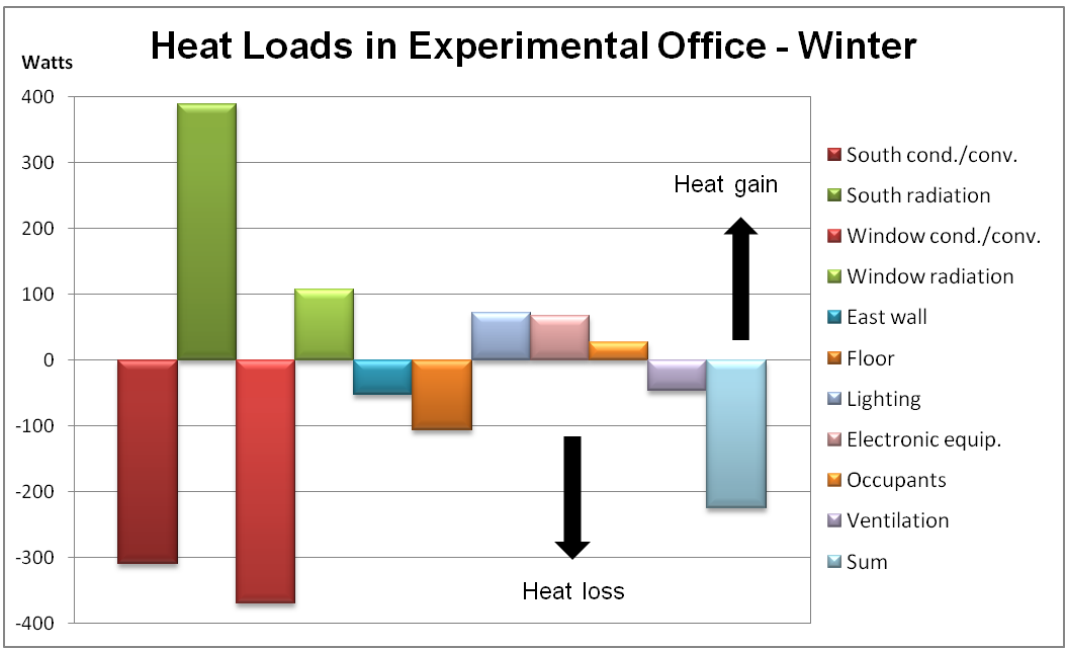

Figure 56: Heating load analysis of the test office

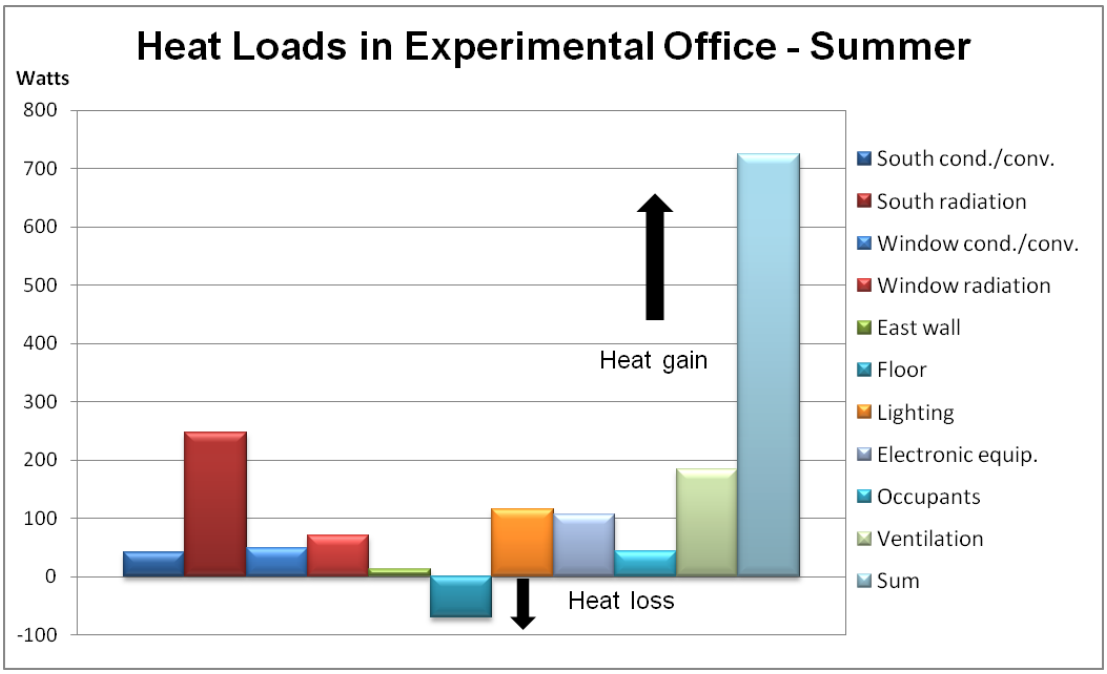

Figure 57: Cooling load analysis of the test office

3.4 Low ΔT Heat Exchanger Experiments Results

3.4.1 Baseline System Experiment Results

The objective of conducting a baseline system test is to evaluate the thermal comfort (in terms of operative temperature) of the space provided by convectional fan-coil unit in winter or window-type AC unit in summer. It is also the purpose of the baseline system to be served as a comparison to the later low ΔT heat exchanger system test. Due to the season restriction, only heating test has been conducted.

One weekend was randomly picked from January and February of 2011 to perform the baseline test. The test lasted for 60 hours. The four OT sensors were placed in the center of the office. A relative humidity sensor was also attached to the pole which holds OT sensors, and it was placed at the height of 0.6 m. Four aluminum tape-shielded thermocouples (accuracy of ±0.5 K) were located at the center of the heater, air outlet of the heater, window and outside of the office. The purpose of shielding the thermocouples is to minimize the impact from direct solar radiation.

Figure 58 demonstrates the operative temperatures recorded by the four OT sensors. It is clear to find that the operative temperature readings are stratified. This is due to the air temperature stratification caused by the buoyancy force. The fluctuation of the readings mainly comes from the change of exterior wall temperature. This statement can be supported by the fact that the trend of fluctuation of each OT sensor

is almost identical to each other. Hence, the fluctuation must have come from the same source.

There are two temperature peaks in Figure 58 (in red circles) worthy of a further investigation. It was found that the two peaks happened approximately at the same time in two consecutive days. The peaks are probably because during one time in a day, the direct solar radiation reaches one or all spheres (depending on the cloudiness) through the window. This assumption was further supported by Figure 59. It is clear that the two peaks of window surface temperature are coincident in time with the peaks in Figure 58.

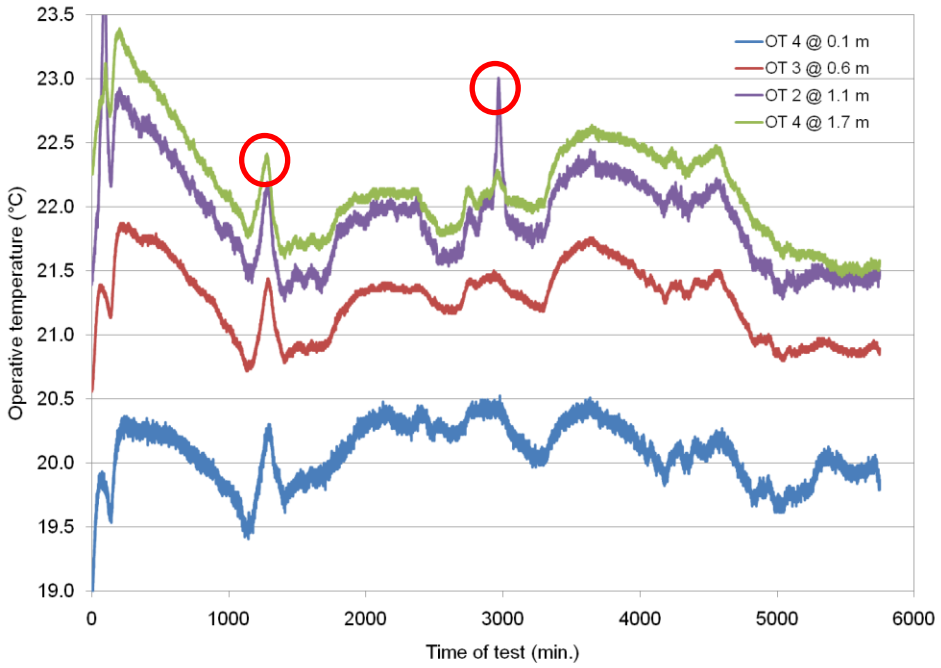

Figure 58: Operative temperature measurement in the baseline test

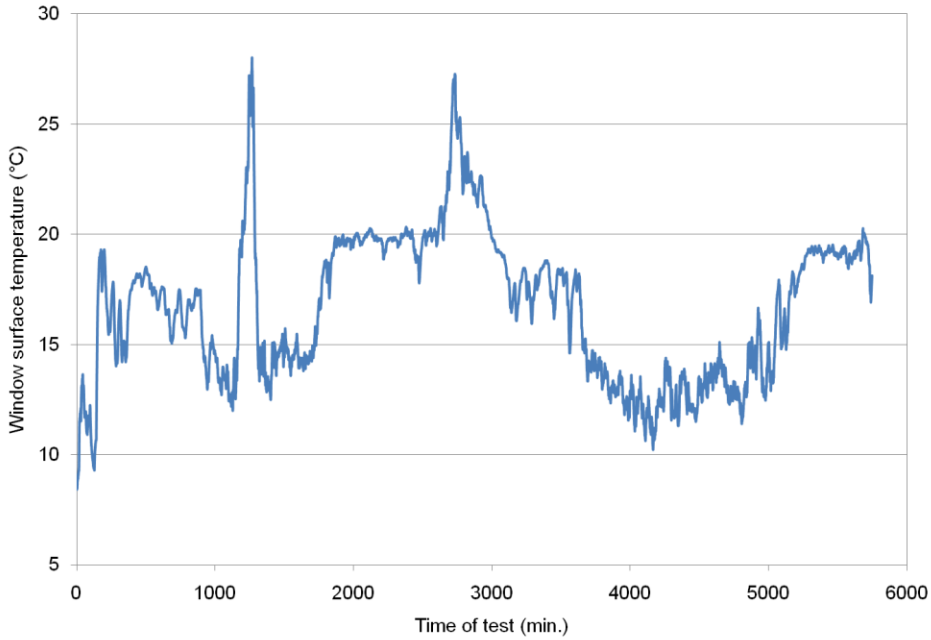

Figure 59: Window surface temperature variation during the baseline test

The hot water to the convectional fan-coil unit comes from the campus central heating system. Its temperature is around 80°C. The heater is located 0.4 m away from the floor. A strong stratification of air temperature was anticipated due to the buoyance force. The strong stratification should also be reflected on the operative temperature measurement. Figure 60 plots the average operative temperature readings of each OT sensor during the test day. The average operative temperatures of OT sensors are 23.0°C, 22.6°C, 21.5°C and 19.9°C, respectively. The maximum temperature difference of 3.24 K is between OT 1 (1.7 m high) and OT 4 (0.1 m). It represents the fact that when using the conventional fan-coil unit, occupants are subject to cold feet and warm head with the temperature difference over 3 K. According to the ASHRAE standard 55, this should be considered as uncomfortable. Generally speaking, people feel thermally comfortable when the feet are warmer than

the head. Moreover, the temperature stratification between the head and the feet should not exceed 3 K.

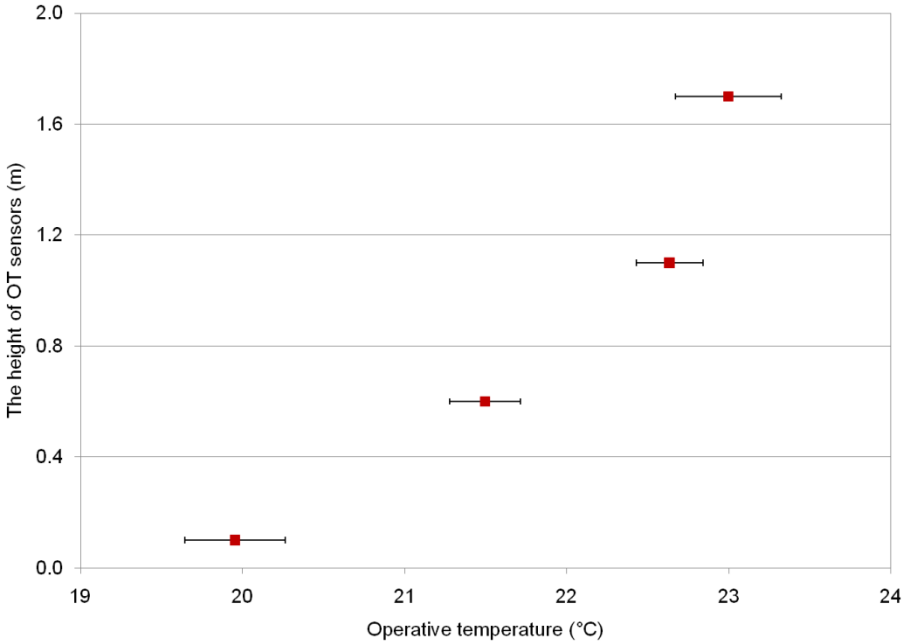

Figure 60: Thermal comfort analysis of the baseline test: operative temperature stratification

The other problem from the use of conventional fan-coil units in winter is the temperature at lower body, especially the feet, can be too low. Figure 61 overlays the 60-hour operative temperature data onto a psychrometric chart. The blue quadrilateral in the psychrometric chart is the simplified ASHRAE thermal comfort zone. Most of the OT 4 data falls out of the comfort zone to its left side. It means that occupants may suffer too low temperature around their feet area, although the other parts of body are subject to comfortable temperatures.

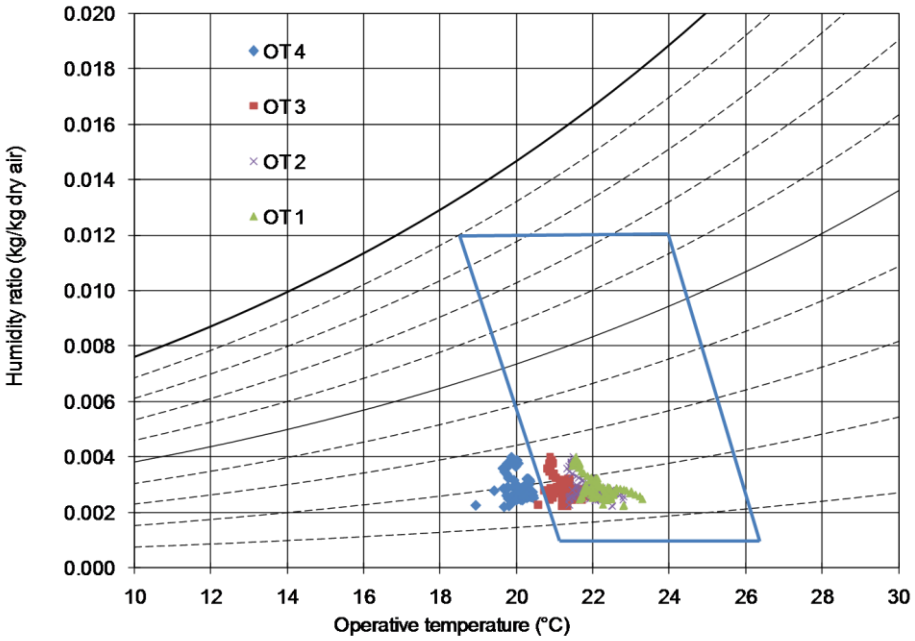

Figure 61: Thermal comfort analysis of the baseline test: operative temperatures in the comfort zone

In summary, the conventional fan-coil unit with hot water temperature of 80°C is able to provide enough heating capacity to cover the office load. However, in terms of thermal comfort, occupants can still suffer from too large temperature difference between the feet and the head, and the feet area temperature is lower than required by ASHRAE comfort zone.

3.4.2 Low ΔT Heat Exchanger Experiment Results

The experiment of low ΔT heat exchanger was conducted after the baseline test. In order to eliminate the effect from the fan-coil unit, both the supply water valve and fan were shut off during the test. The objectives of the experiment are to evaluate the general performance of the low ΔT heat exchangers and its hot water supply loop, to study the thermal comfort created by the low ΔT heat exchanger and to provide experimental data for the future validation of simulation codes.

The experiment started with filling distilled water into the water tank. The usage of distilled water is to reduce the possibility of fouling inside the tubes and HXs. The water pump was then turned on to fill water into the water loop system and the heat exchangers. Since the manufacturer's catalog (Uponor, 2010) suggests a minimum water flow rate to be 62 gs^{-1} (1 GPM), the pump was adjusted for a water flow rate of 78.5 gs^{-1} (1.25 GPM). The water flow rates during the entire test were plotted in Figure 62. The water temperature was set to be 35 °C, which is approximately 10 K above the space air temperature. Compared to the baseline system having a hot water temperature of 80°C, the ΔT between hot fluid and air temperature was reduced by around 45 K. The thermocouples located at the heater inlet and outlet recorded the temperature readings which are plotted in Figure 63. The heater capacity can then be calculated based on the water flow rate and the temperature difference across the heater (see Eq. (42)). Without any heat loss, the heater capacity should be the same as the low ΔT heat exchangers (see Eq. (43) for HX capacity calculation). The two capacities were plotted against each other in

Figure 64. The average capacities of the heater and the HXs are 527 W and 546 W, respectively. It results in an average deviation of only 3.7%. The small deviation reflects good measurement accuracy.

$$Q_{heater}=\dot{m}\cdot c_p\cdot(t_{heater\ out}-t_{heater\ inlet}) \quad (42)$$

$$Q_{heater}=\dot{m}\cdot c_p\cdot(t_{HX\ inlet}-t_{HX\ outlet}) \quad (43)$$

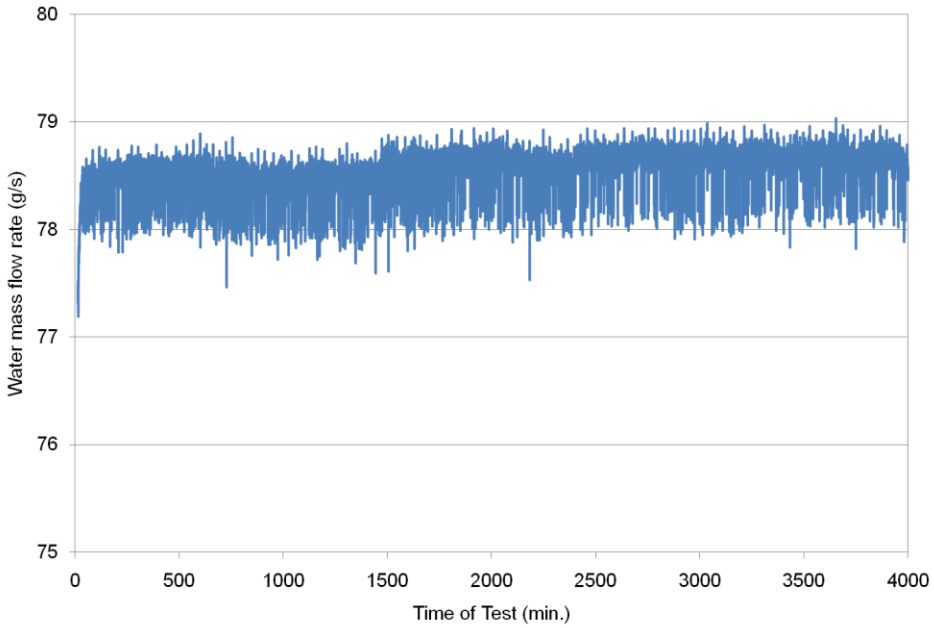

Figure 62: Water flow rate variation during the low ΔT HX

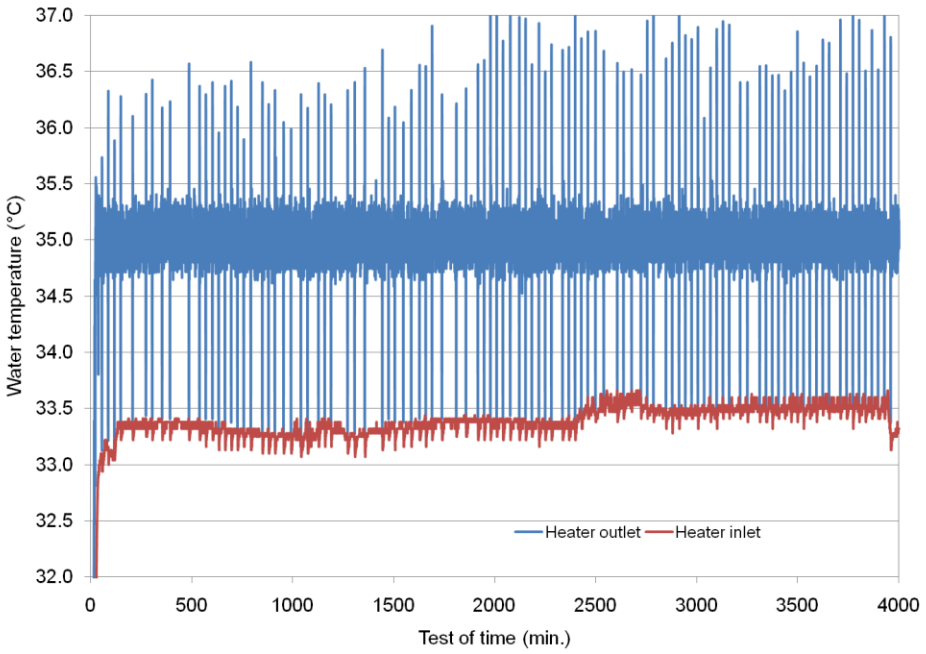

Figure 63: Heater inlet and outlet temperatures' variations

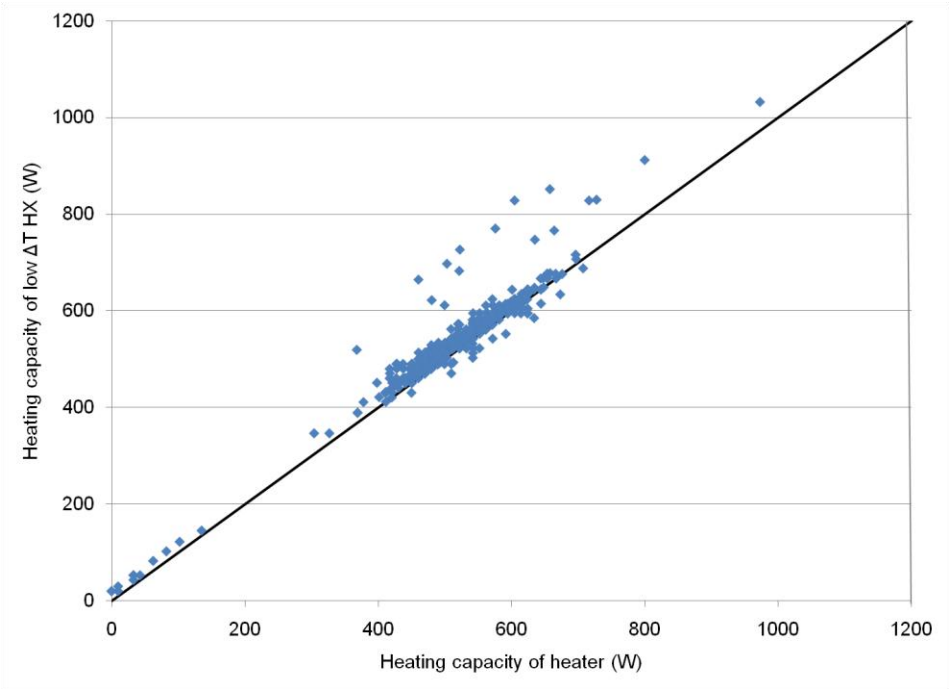

Figure 64: Comparison of measured heating capacities of heater and HX

It is then important to study the thermal comfort created by the low ΔT heat exchangers. In Figure 65, the average operative temperatures of each sensor during the 60-hour test period were plotted against the sensors' heights. The highest sensor (OT 1) has an average temperature of 24.3°C, while the lowest sensor (OT 4) has an average temperature of 22.3°C. Compared with the results of the baseline test, the average operative temperature readings from OT 1 and OT 4 was found to increase by 2.4 K and 1.3 K, respectively. The reason behind the increase is the elevated surface temperature. The north wall of the office had an average surface temperature of 23.2°C during the baseline test, while it increased to 35°C during the low ΔT HX test. The increased surface temperature increased the MRT of all OT sensors; therefore the operative temperature readings were increased. Since OT 4 sensor had the lowest air temperature reading due to the buoyancy force, the increased MRT had the largest effect on its increase of operative temperature. Consequently, the temperature difference between occupants' head (OT 1) and feet (OT 4) was reduced to 2.0 K. This demonstrates a better thermal comfort in terms of a reduced head-to-feet temperature stratification.

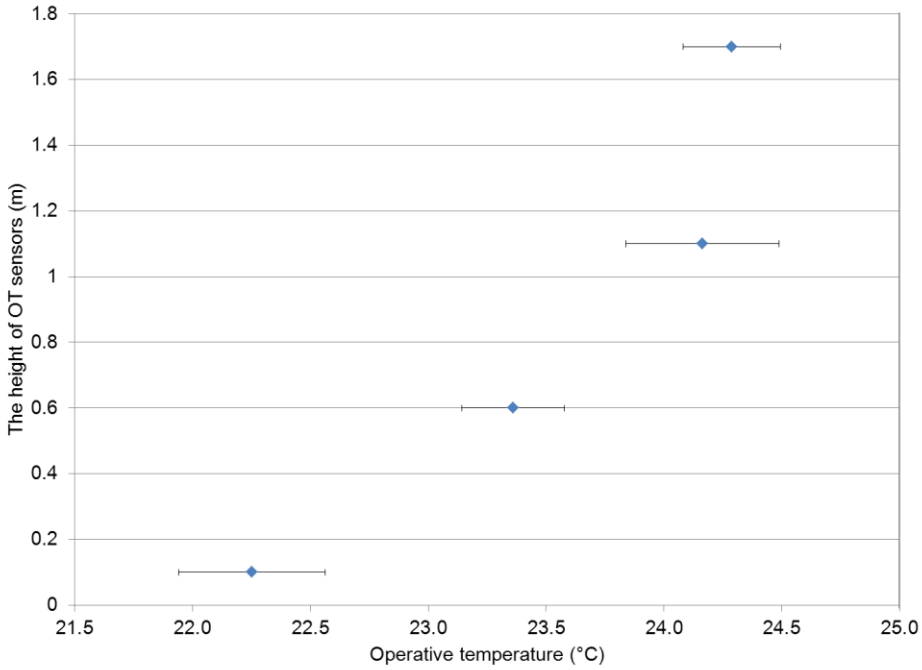

Figure 65: Thermal comfort analysis of the low ΔT HX test: Operative temperature stratification

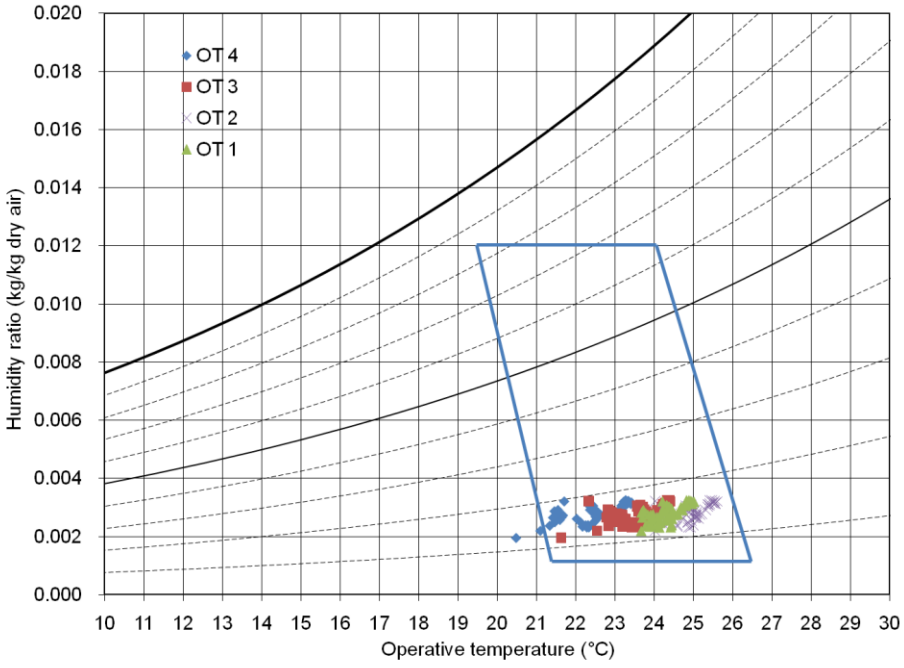

Figure 66: Thermal comfort analysis of low ΔT HXs: operative temperatures in the comfort zone

Figure 66 overlays the entire OT sensors readings on the psychrometric chart. The blue quadrilateral represents a simplified thermal comfort zone according to the ASHRAE standard 55. Almost all measured points fall into the thermal comfort zone. The higher surface temperature of north wall increased the operative temperature reading of the OT 4 from the baseline test. Hence, the second issue of the baseline test, too low temperature of OT4, has been addressed.

Chapter 4: Modeling the Operative Temperature Field in an Office Setting

4.1 The Objectives of Operative Temperature Field Modeling

The experimental test demonstrates encouraging results when using the low ΔT heat exchanger in terms of obtaining better thermal comfort than the baseline fan-coil unit. However, there are several questions still unanswered. First of all, both systems show the temperature stratification with respect to the height. However, the test data provides only several data point. How to get a complete picture of temperature stratification elsewhere inside the room? Second, the operative temperature sensor measures only operative temperature, but how MRT affects the operative temperature in detail? Finally, how to extrapolate the results to other conditions?

In order to answer all the above questions and make further investigation on the low ΔT heat exchangers, the simulation of operative temperature field created by low ΔT heat exchangers must be conducted. It should focus on the simulation of operative temperature and velocity profiles created by the low ΔT heat exchangers in the air-conditioned space.

The objectives of the modeling are to achieve a complete understanding of the thermal comfort zone created by low ΔT heat exchangers from solving the physical governing equations; to expand the database of low ΔT heat exchanger's operation from experimental test.

The OT modeling started from the MRT calculation, followed by the modeling of air temperature and velocity inside a square enclosure and finally the combination of MRT and air temperature to obtain the operative temperature.

4.2 The Calculation of Mean Radiation Temperature (MRT)

To calculate the operative temperature, the MRT has to be obtained besides the air temperature. The MRT can be calculated as:

$$\overline{t_r} = \sum F_{p\text{-}i} t_{si} \tag{44}$$

Where: $F_{p\text{-}i}$ is the angle factor (view factor) from a person to surface i; t_{si} is the surface temperature of surface i. From the above equation, it is clear that in order to get the MRT, we have to calculate the view factor from all solid surfaces, i.e., walls, floor, ceiling, to the person (occupant).

Moreover, from Eq. (44), one can get a better interpretation of MRT as a view factor- weighted average surface temperature. The view factor is mainly affected by the distance between the interested point and the surface, and the size of the surface. The following discussion within the section focuses on the model of the MRT temperature calculation, the view factor calculation and finally the MRT calculation results

4.2.1 Model Description

Figure 67 describes the radiation model adopted in the study. The room is assumed to be 3 m by 3 m by 3 m with four walls (front wall is not shown), a ceiling and a floor. The left wall has an indoor heat exchanger, and it is assumed that the heat exchanger make the entire wall be at a constant temperature. The dimension of the MRT model matches the model of the CFD simulation of air temperature, which will be discussed later in the chapter. The right wall has a window facing south whose area is smaller than the wall. The window has a higher temperature than the rest of the wall because of the solar radiation. The four walls, i.e., the frontal wall, the back wall, the left wall and the right wall, are assumed to have uniform temperatures. It was through the later literature review (Rohan et al., 2010) that an additional surface has to be added to the model. There is a heated-up area on the floor receiving the solar radiation through the window. The temperature of the area can be higher than the rest of the floor, and the size and temperature of the area vary depending on the solar altitude angle and azimuth angle. Figure 68 describes the detail of the sun light area calculation. For simplification, the person in the room is simplified to be a sphere. Dunkle (1963) defined the equivalent sphere radius of both a standing person and a sitting person. However, since the sphere's radius is infinitesimal compared with the room dimension, the radius is neglected in the model. The sphere is free to be moved anywhere inside the room because there are actually no restrictions for occupant's activity inside the room. The most important function of the model is to output the MRT of the sphere inside the room.

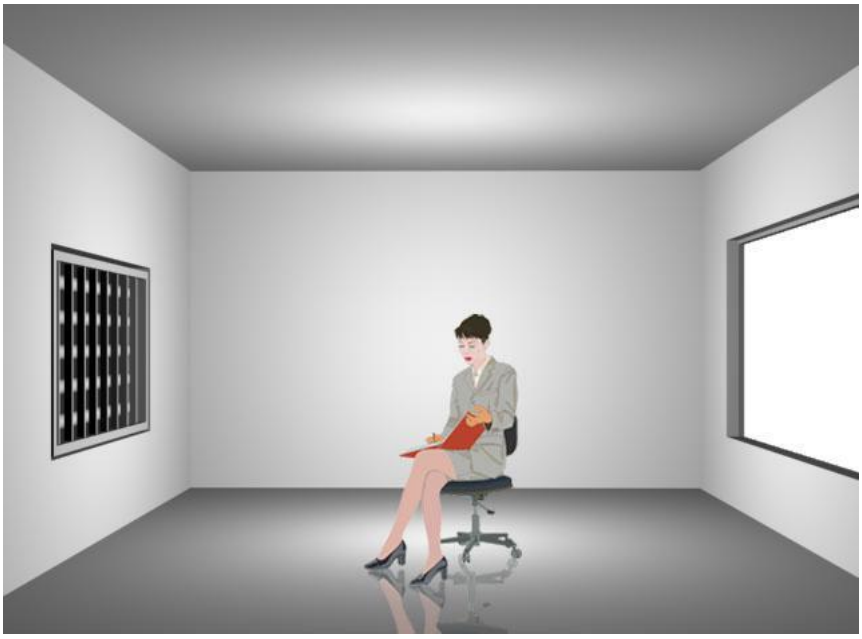

Figure 67: Adopted radiation model setup

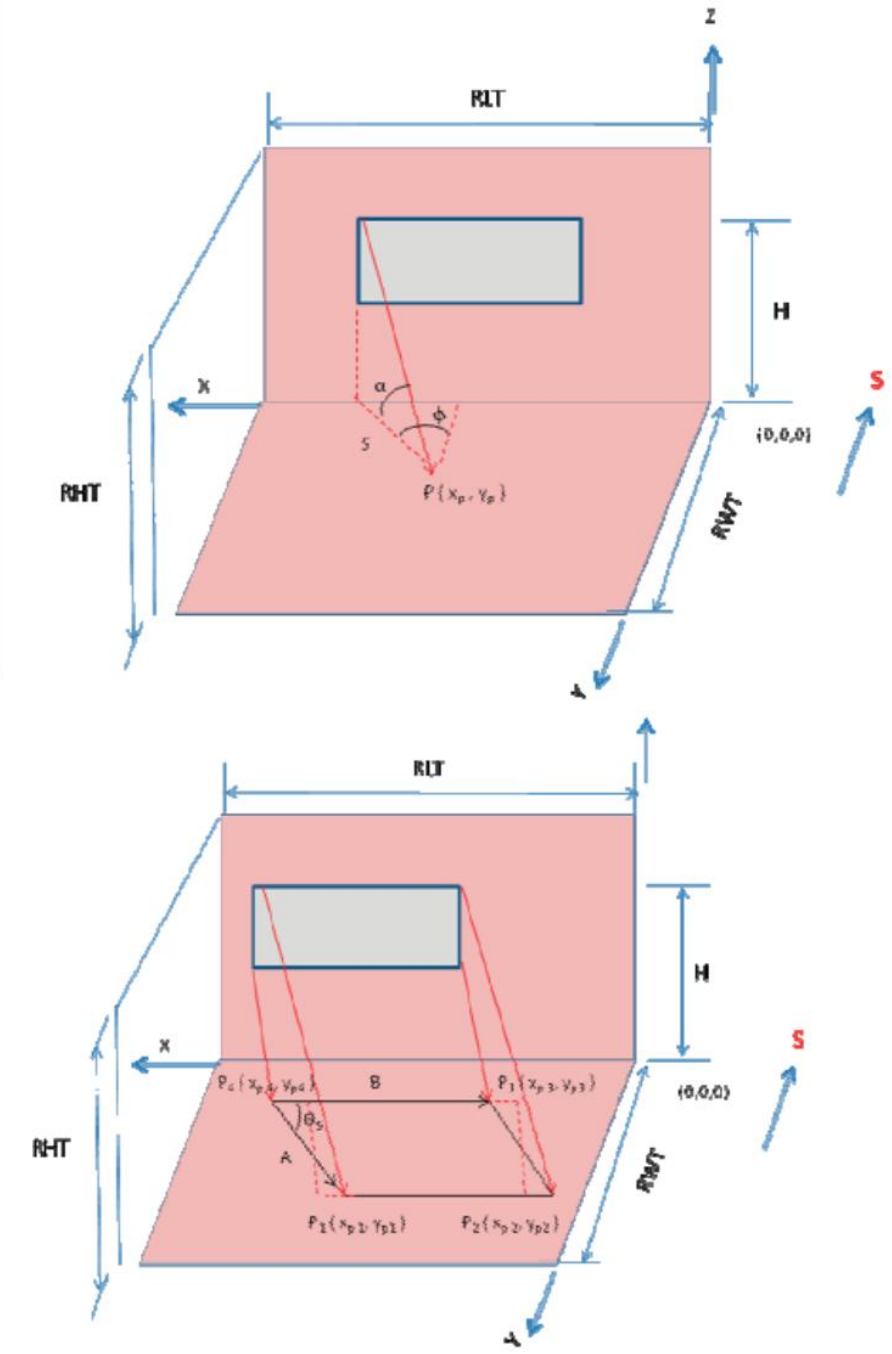

Figure 68: Calculation of sun light area (where α and φ are the solar altitude angle and azimuth angle, respectively) (Source: Rohan et al., 2010)

In order to obtain the mean radiation temperature anywhere in the room, we have to first obtain the view factor between the sphere (representing occupant's activity area) inside the room and all the eight surfaces. The calculation of view factors started with the one between two infinitesimal areas, and then integrated the result to obtain the one between a sphere and a wall surface.

The detailed steps are as follows: first, use Eq. (45) to calculate the view angle between two infinitesimal areas of the sphere and wall (see Figure 69). Then, integrate the two infinitesimal areas to the entire sphere and a quarter of the wall as in Eq. (46) (see Figure 70).

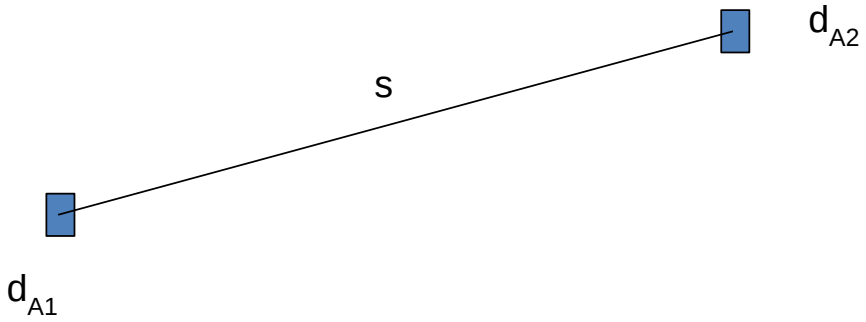

Figure 69: Calculation of view factor between two infinitesimal areas

$$F_{1\text{-}2} = \iint_{A1A2} \frac{\cos\theta_1 \cos\theta_2}{\pi s^2} dA_1 dA_2 \qquad (45)$$

Where θ_1, θ_2 are the angle of line s to surface d_{A1} and d_{A2}, respectively.

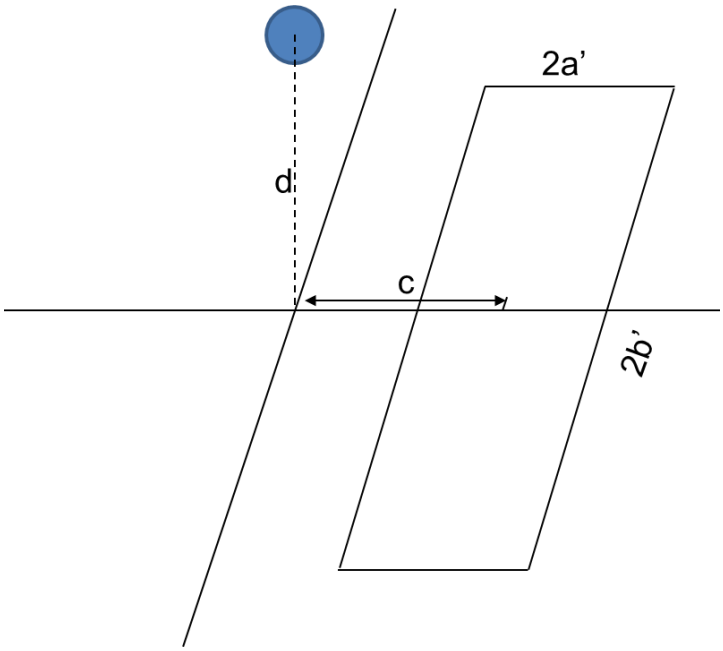

Figure 70: View factor from a sphere to a non-intersected rectangular area

$$F_{1-2} = \int_{Z-B_2}^{Z+B_2} \frac{dX}{(1+X^2)\sqrt{1+X^2+B_1^2}} \tag{46}$$

where.$B_1=\frac{b'}{d}$, $B_2=\frac{q'}{d}$, $Z=\frac{c}{d}$ (Sabet and Chung, 1987)

From Eq. (46), the view factor between a sphere and the entire wall can be calculated by summing up four view factors which are from the sphere to each quarter-wall. With different *d* and rectangular dimensions, one can calculate view factors from anywhere inside the room to all the walls.

4.3 Calculation of Air Temperature inside an Enclosure

4.3.1 Model Description

Based on the literature review and previous radiation model, the enclosure model for natural convection calculation is defined as a square space with the left wall having a uniform temperature of T_c and a right wall having uniform temperature of T_h. Both the floor and ceiling are assumed to be adiabatic. The governing equations, which are Eq. (47) to Eq. (49), and boundary conditions:

Continuity equation:

$$\nabla\cdot\vec{u}=0 \tag{47}$$

Momentum equation:

$$\rho\frac{\partial\vec{u}}{\partial t}+\rho\vec{u}\cdot\nabla\vec{u}=-\nabla P+\rho g\vec{j}\beta\left(T-T_c\right)+\mu\nabla^2\vec{u} \tag{48}$$

Energy equation:

$$\rho c_p\frac{\partial T}{\partial t}+\rho c_p\vec{u}\cdot\nabla T=\kappa\nabla^2 T \tag{49}$$

Boundary conditions:

At the top and bottom walls of the cavity

$$u=v=0$$

$$\frac{\partial T}{\partial\vec{n}}=0$$

At the left wall

$$u=v=0$$

$$T=T_C$$

At the right wall

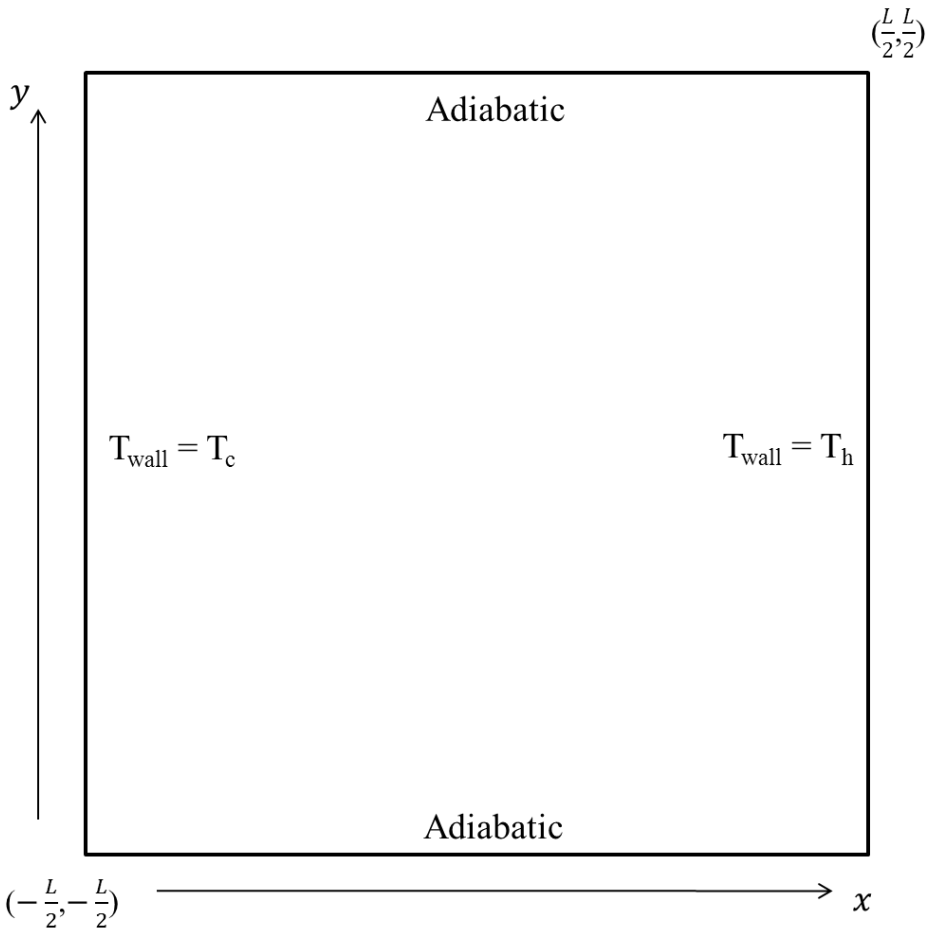

Figure 71: Boundary conditions and dimensions of the adopted natural convection model

In Figure 71, *x* and *y* are used to represent the horizontal and vertical direction, respectively. The side length of the square is *L*. The bottom left corner has the coordinate of $(-\frac{L}{2}, -\frac{L}{2})$, while the top right corner has the coordinate of $(\frac{L}{2}, \frac{L}{2})$.

4.3.2 CFD Simulation

For the airflow inside the square enclosure, its Rayleigh number reaches 10^9 when the dimension of the square is over 1 m by 1 m. Therefore, the flow should be considered as turbulent flow. The previous literature review proves difficult to analytically solve such problem. Hence, a commercial CFD software package, Fluent (ANSYS, Inc., 2006), was chosen to model the natural convection inside square enclosure. Figure 72 shows the mesh generated by Gambit (ANSYS, Inc., 2011). The grid has 150 by 150 quad meshes with enhanced mesh density in the boundary layer to capture the complicated flow characteristics. To be specific, the boundary layer has the first row of 1 mm and the growth of 1.15, i.e., the entire depth of the boundary layer is 20 mm. The mesh is proved to be sufficient to solve the square of 1 m by 1 m case. The turbulence model used in the model is k-ω SST model. Figure 73 is the screenshot of the viscous model GUI in Fluent. The isotherms and streamlines are plotted in Figure 74 and Figure 75. The model was later expanded to be a 3 m by 3 m square space. It is because the new dimension is much closer to the actual size of a room. The original mesh structure did not lead to a convergent solution. The reason is that an increased space dimension increases the size of a cell as well; therefore, the cell cannot capture the characteristics of the boundary layer. As a solution, the mesh was refined (see Figure 76). The new mesh provides a converged solution as plotted in Figure 77 and Figure 78.

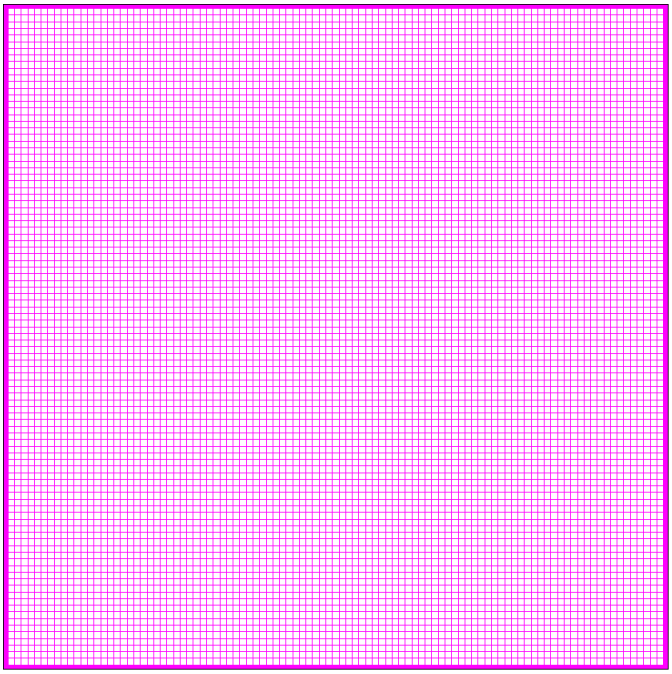

Figure 72: 1st generation of mesh generated by Gambit®

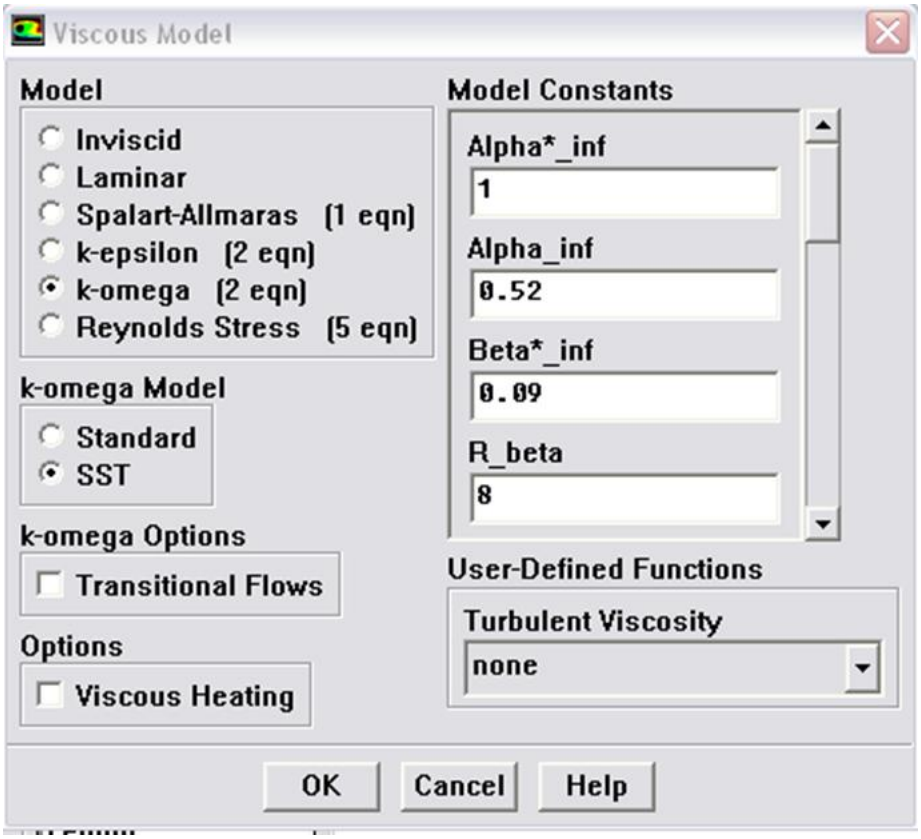

Figure 73: Screenshot of viscous model GUI in Fluent®

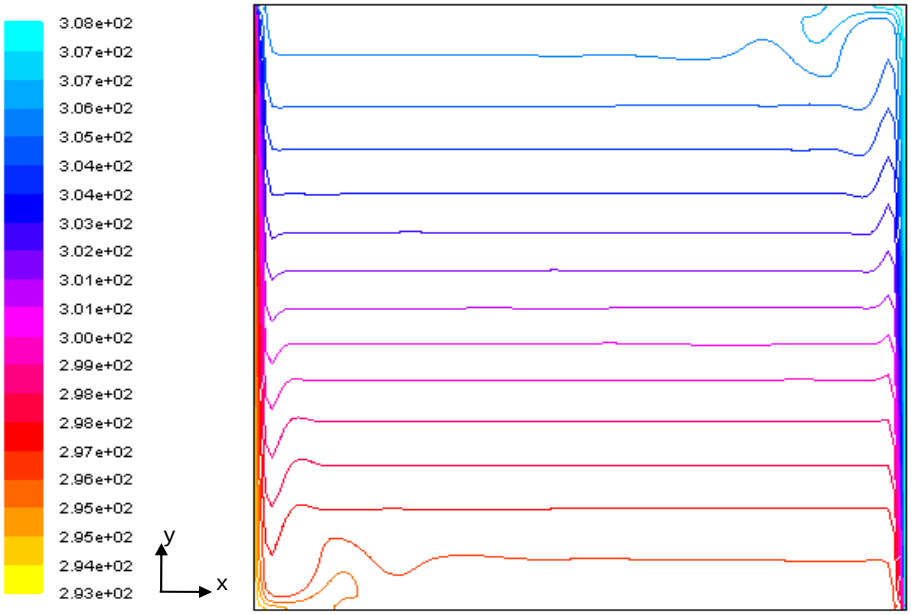

Figure 74: Isotherms of air in the enclosure (1 m by 1 m)

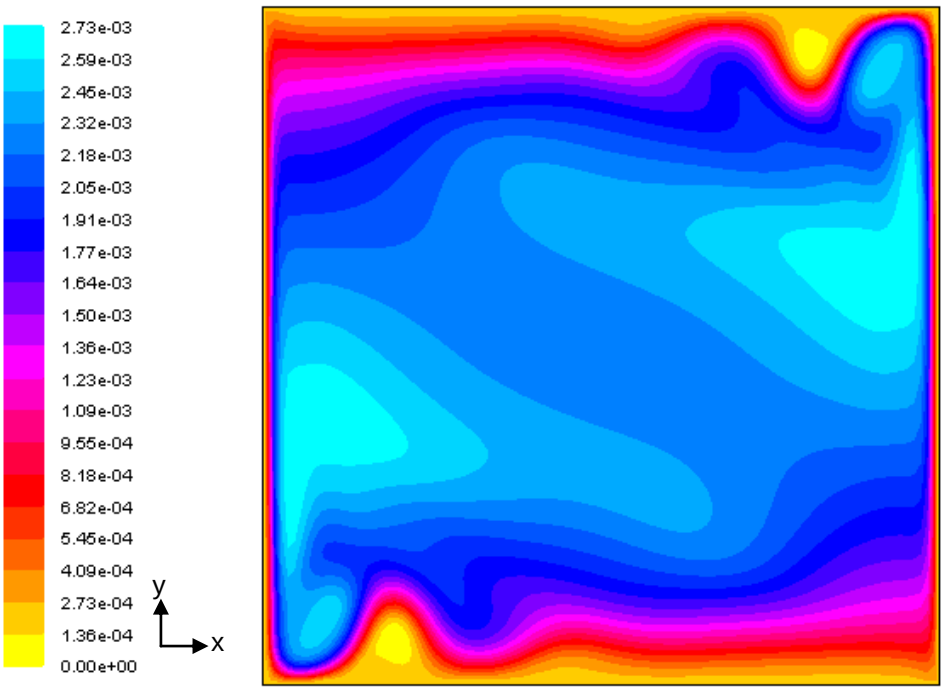

Figure 75: Streamlines of air in the enclosure (1 m by 1 m)

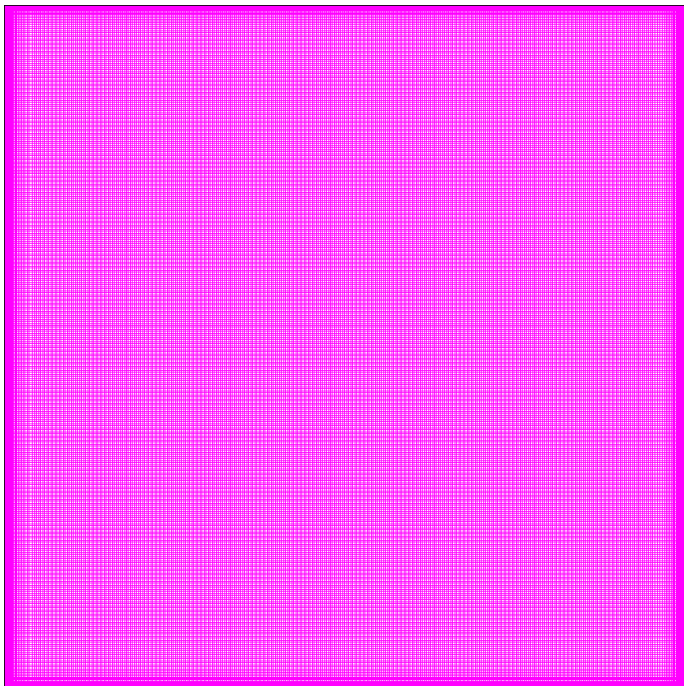

Figure 76: 2nd generation of mesh generated by Gambit®

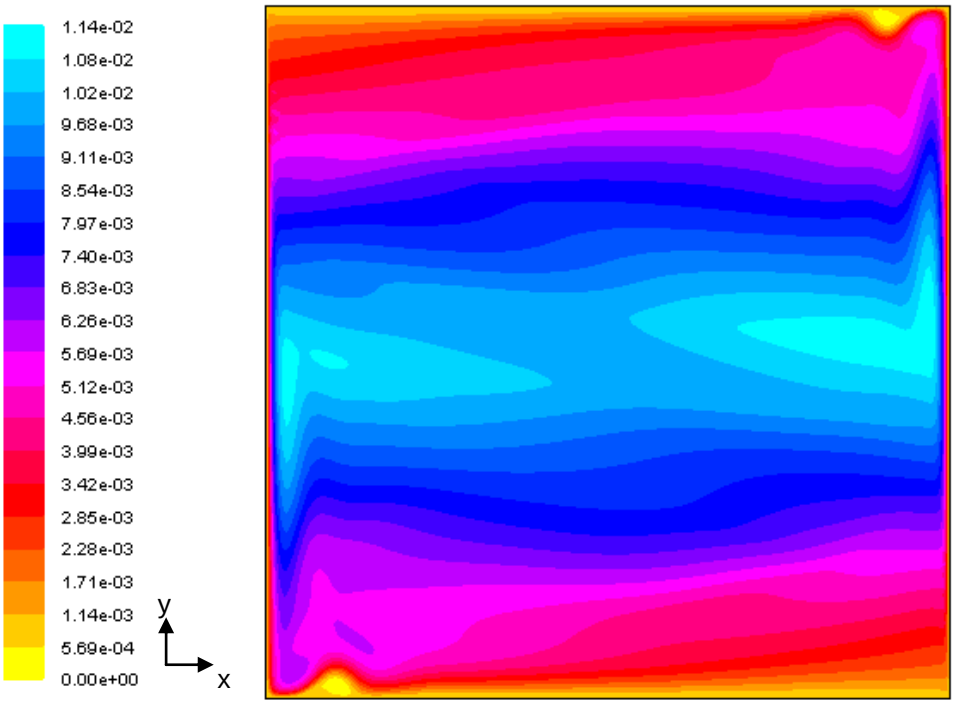

Figure 77: Streamlines of air in the enclosure (3 m by 3 m)

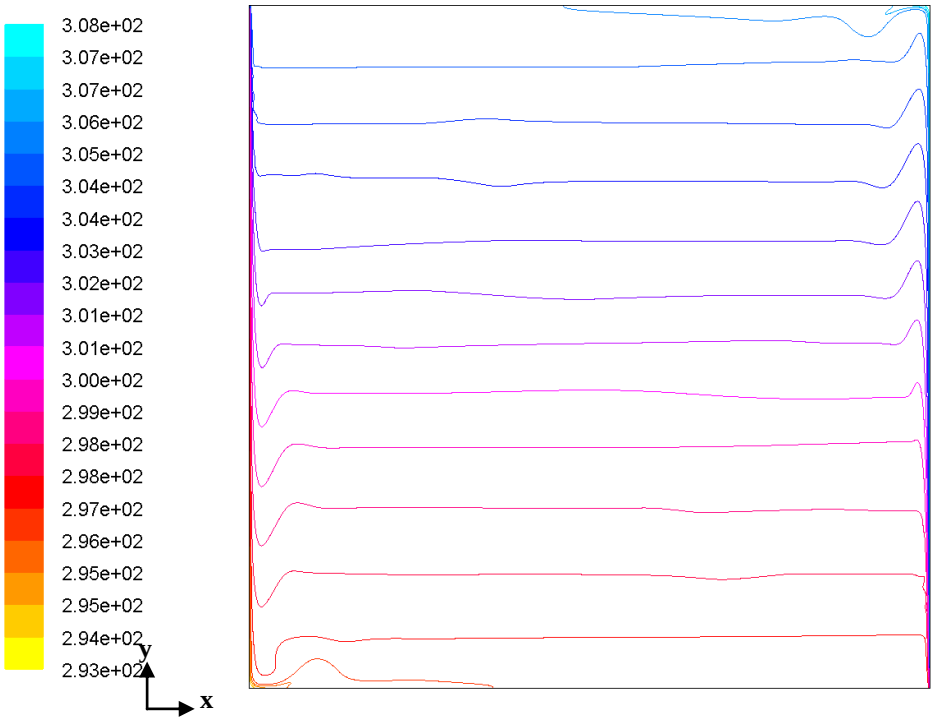

Figure 78: Isotherms of air in the enclosure (3 m by 3 m)

4.3.3 Linear Curve Fit for CFD Results

It can be found from Figure 78 that the temperature profile of bulk air in the enclosure can be simplified as a function of *y* axis (the opposite of $\vec{g}$ direction) only. The temperature of air close to the side walls has a rapid temperature change, so different correlations have to be used to predict the air temperature near the cold wall and hot wall. Eqs. (50) through (52) are the correlations used to calculate the air temperatures inside the room. More specifically, Eq. (50) is used to calculate the bulk air temperature in the room ($-1.48<y<1.48$), and Eqs. (51) and (52) are used to calculate air temperature near the cold wall and the hot wall, respectively. Figure 79 through Figure 81 demonstrate the comparisons between temperatures calculated from CFD and curve fitting.

$$T\ (\text{in K}) = 3.02\times h + 300.51 \tag{50}$$

$$T\ (\text{in K}) = -0.38\times h^6 + 0.61\times h^5 + 1.39\times h^4 - 0.69\times h^3 - 0.92\times h^2 + 1.99\times h + 298.57 \tag{51}$$

$$T\ (\text{in K}) = -0.34\times^{h^6} + 0.97\times h^5 + 0.49\times h^4 - 1.58\times h^3 + 0.0048\times h^2 + 1.67\times h + 304.4 \tag{52}$$

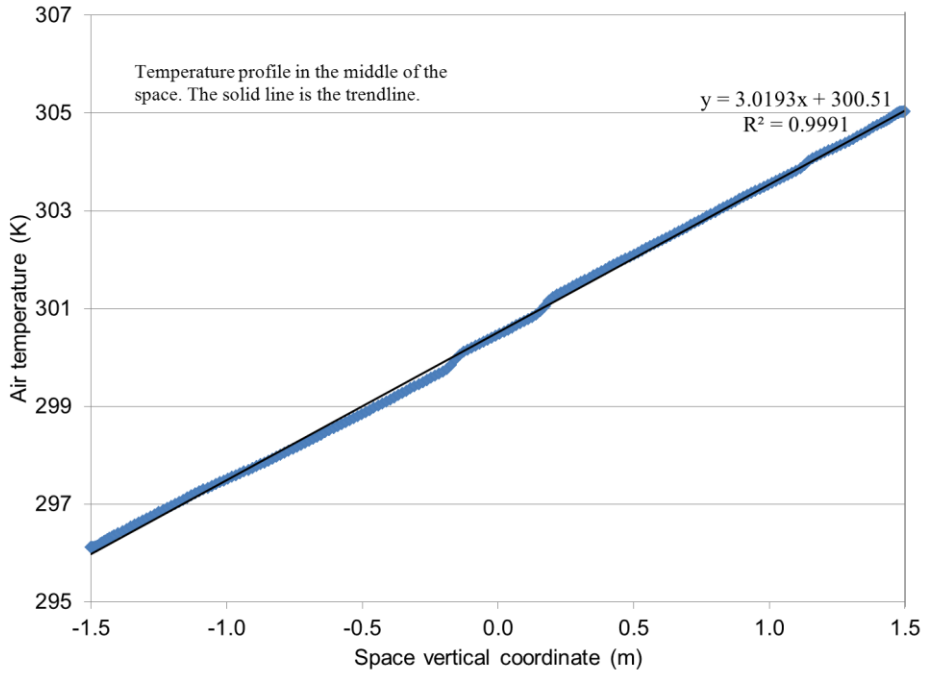

Figure 79: Comparison of temperature readings from CFD and curve fitting (bulk air region)

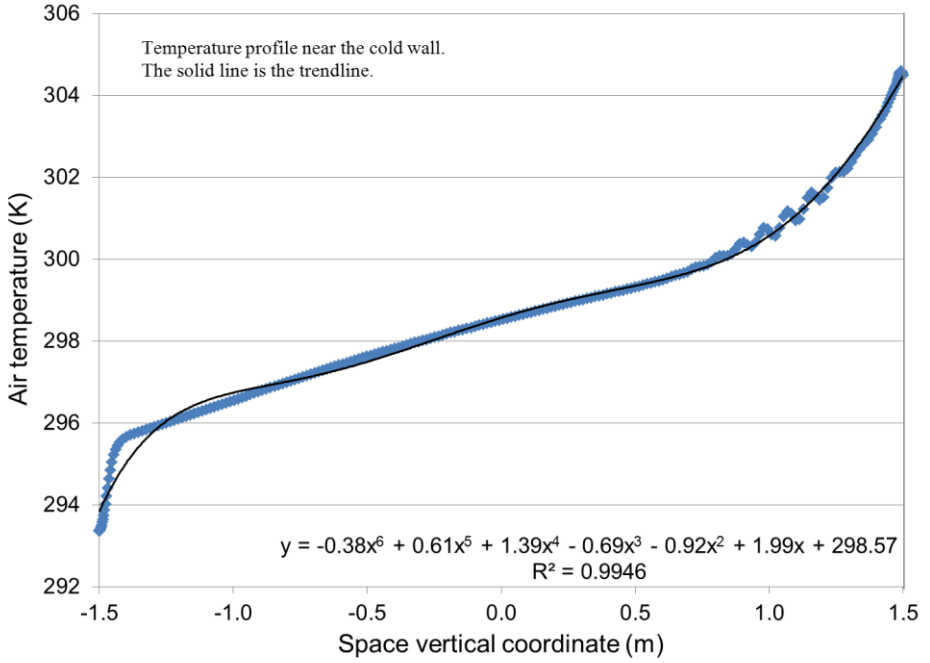

Figure 80: Comparison of temperature readings from CFD and curve fitting (close-to-cold wall region)

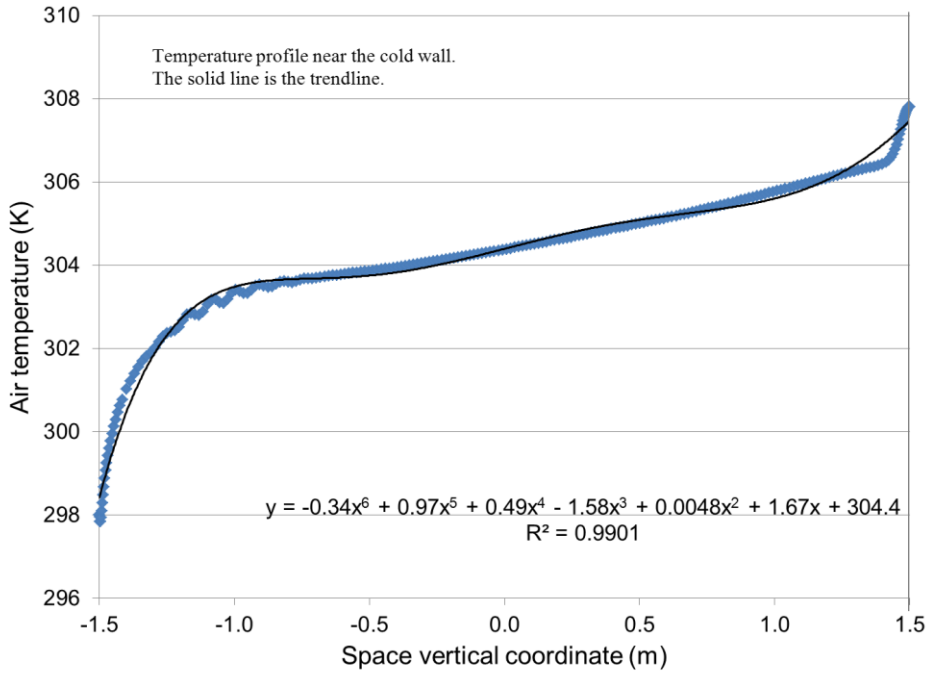

Figure 81: Comparison of temperature readings from CFD and curve fitting (close-to-hot wall region)

4.3.4 Calculation of Operative Temperature

Sections 4.3.2 and 4.3.3 describe the calculation of the MRT temperature and the air temperature in the space. Based on the previous literature review, under most cases, an operative temperature is the arithmetic mean of the MRT temperature and air temperature. EES (EES, 2009) is used to simulate the operative temperature profile. The model assumptions are listed as follows:

- An eight-surface radiation model
- Air temperature are calculated by correlations Eqs. (50) through (52).
- $T_{coldwall}$=20°C
- T_{window}=35°C
- $T_{sunlight\ area}$=35°C

- The rest of walls have the same temperature of 27°C
- Figure 82 through Figure 84 show the results of operative temperature in bulk region, near the cold wall and the hot wall. The bulk air flow region is from 0.02 m away from the cold wall to 0.02 m away from the hot wall. The cold wall region and hot wall region refer to the area within 0.02 m to the walls.

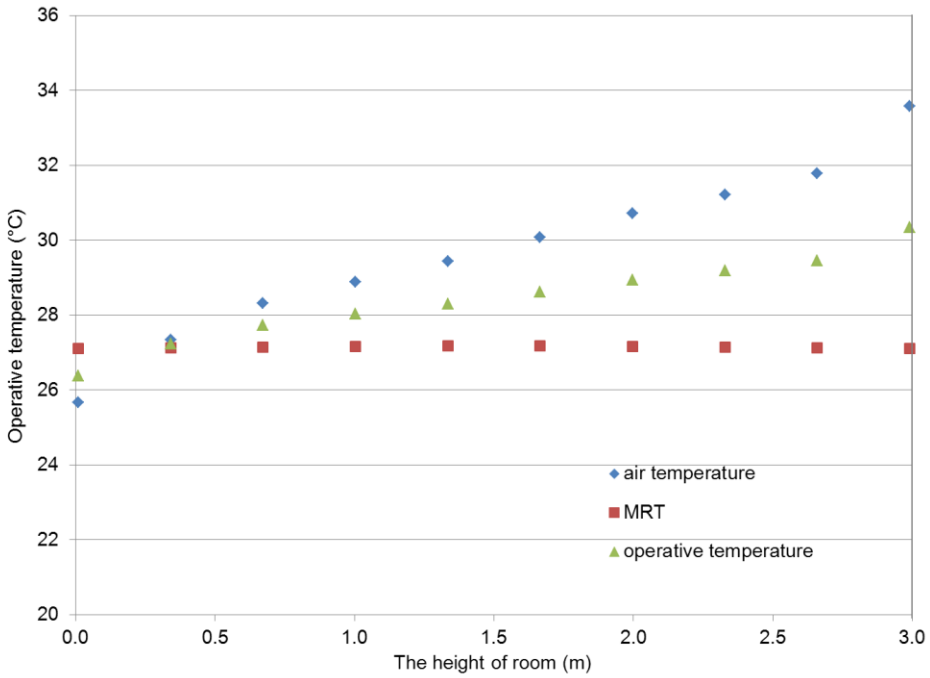

Figure 82: Simulated operative temperature of air in the bulk flow region

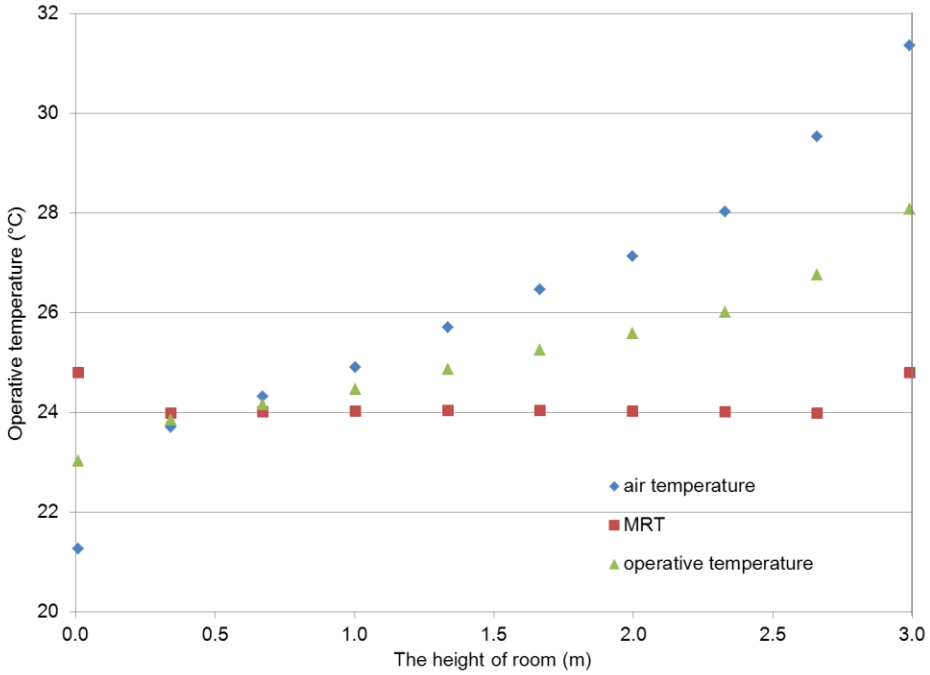

Figure 83: Simulated operative temperature of air near the cold wall

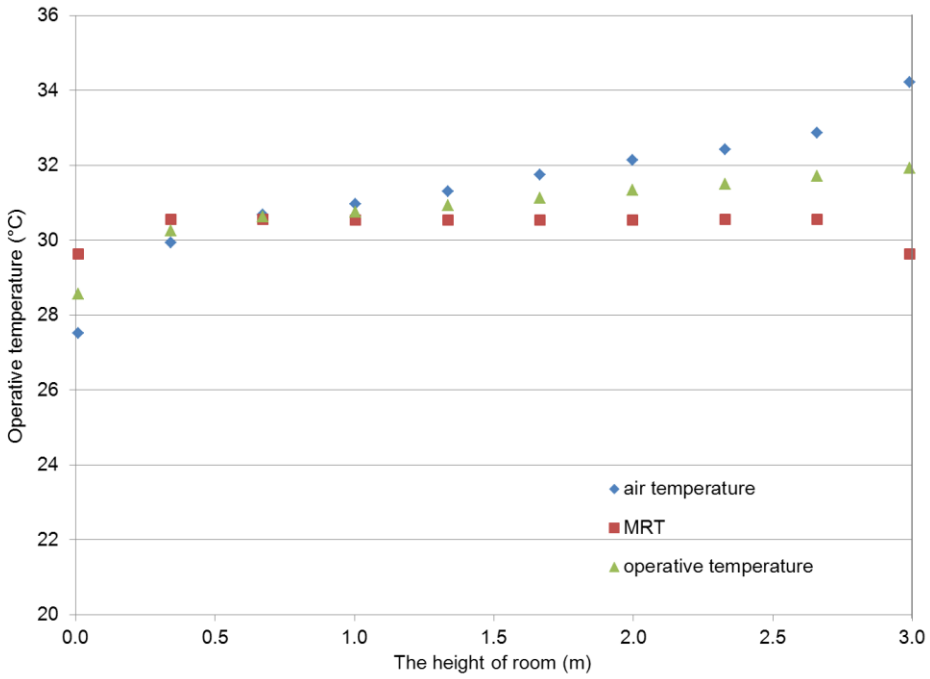

Figure 84: Simulated operative temperature of air near the hot wall

4.3.5 Validation for Operative Temperature Simulation

The simulation results from the operative temperature model were compared with the experimental data. During the test, the operative sensors were placed at the center of the roughly 3 m by 3 m floor; therefore, the model input was adjusted according to the experiments. The model was validated for two different operating conditions, i.e., with the low ΔT heat exchangers on and with the low ΔT heat exchangers off.

When the low ΔT heat exchanger was off, the baseline system was also off. The ambient temperature was around 23°C. Surface temperatures and air temperatures recorded from the experiment were used as the inputs to the model. The readings from the operative temperature sensors were used to compare with the model outputs.

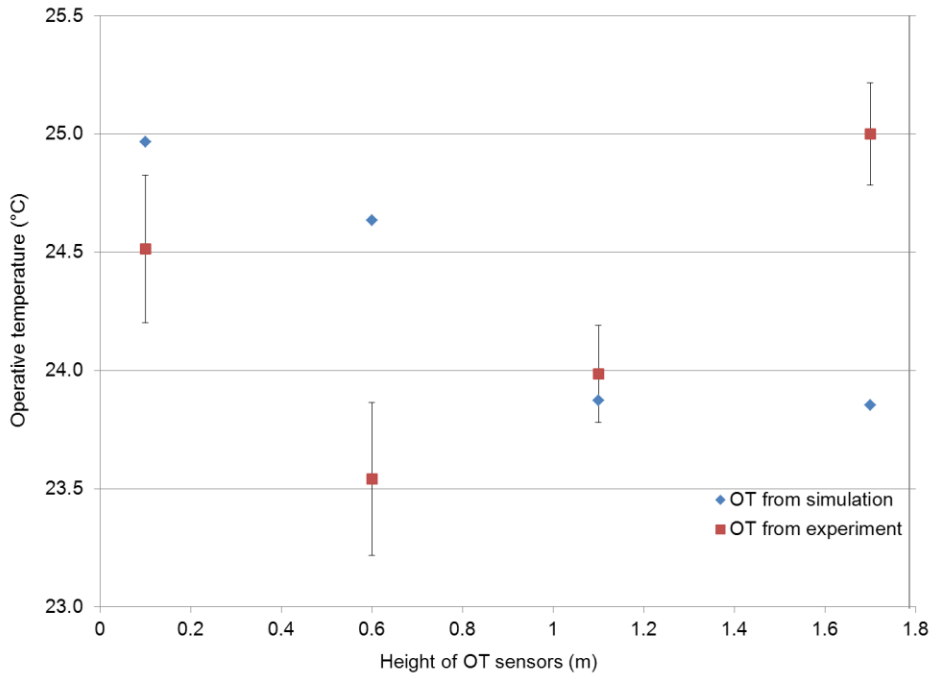

Figure 85: Comparison between OT simulation results and experimental data (low ΔT HX off)

In Figure 85, the average deviation of operative temperature between the simulation and experiment is 0.7 K. The largest deviation comes from OT 3 (0.6 m high), while the smallest deviation comes from OT 2 (1.1 m high). There are two reasons caused the deviations. First, the MRT simulation is based on the eight-surface model, however, in the real office setting, there are extra surfaces affecting the operative sensor's reading.

- The desk blocks part of the solar radiation from the window to the low height sensors
- The cabinet against the north wall and east wall may have different temperatures than the wall temperatures
- The fluorescent light bulbs emit radiation which affects at least OT sensor 1

Second, the air temperature used in this simulation is taken from a two point measurement data. There are no curve fitting correlations available (necessary) for the conditions that low ΔT heat exchanger is off. Therefore, the air temperatures for the four sensors had to refer to the two thermal couples which locate at 0.1 m and 1.0 m off the floor.

The first factor will be addressed in the future work by developing a detailed room-specified MRT calculation model. The new model should be able to import data from computer aided design software which contains the entire room layout. Hence, it can obtain all the possible surface temperatures and view factors. The second factor's impact is supposed to be minimized when the low ΔT HX is on since air temperatures from curve fitting correlations are available.

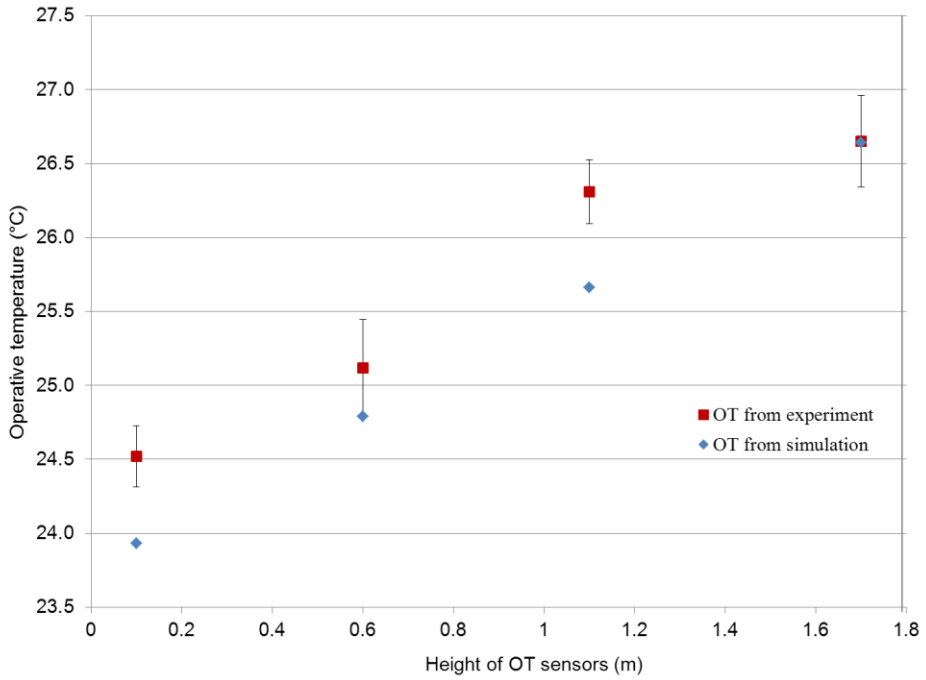

Figure 86: Comparison between OT simulation results and experimental data (low ΔT HX on)

Figure 86 shows the comparison results of operative temperature between simulation and experiments when the low ΔT heat exchanger is on. The profile of operative temperature was greatly affected by the air temperature stratification. It is clear that the deviations are reduced as compared to the previous one. The average deviation decreases from 0.70 K to 0.39 K due to better air temperature simulation. The lowest sensor, OT 4, has the largest deviation of 0.60 K while the highest sensor, OT 1, has the smallest deviation of only 0.01 K. This can be explained as the lowest sensor has the largest penalty from using simple eight-surface model. In the model, the OT 4 was assumed to be entirely subject to the cold exterior wall, however, in experiment there was a desk between the sensor and the wall. The desk blocked the radiative heat transfer from the desk to the cold wall and therefore the operative temperature obtained from the experiment is higher than the one from the simulation.

On the other hand, there was nothing between the highest sensor, OT 1, and the exterior wall. The eight-surface model fully captured the real condition of OT 1, and consequently the deviation was minimized.

In summary, the model provides reasonable accuracy to calculate the operative temperature. To be specific, when the low ΔT heat exchanger was off, the average deviation between the modeling results and experimental results were 0.7 K. When the low ΔT heat exchanger was on, the average deviation was reduced to only 0.4 K. The air temperature correlations obtained from CFD simulation were applied when the heat exchanger was on and helped reduce the deviation. The eight-surface radiation model was proved to be adequate to predict MRT for sensors located at higher position. For those sensors whose radiative heat transfer was blocked by furniture, the model failed to provide a good prediction. Future work on room-specific MRT calculation model is necessary for a better simulation.

Although the curve fitting correlations from the CFD simulation provides good results for air temperature calculation, the computational cost for the CFD simulation is expensive. It took a computer with Duo Core 2.66 GHz CPU and 2 G RAM over 24 hours to obtain the isotherms and streamlines based on one set of wall temperatures, such as a hot wall temperature of 35°C and a cold wall of 20°C. Every change of boundary conditions requires a run of CFD simulation. Besides high computation cost, another problem rising from using the correlations is that large deviation may exist locally. The isotherms in Figure 78 show a clear linear trend in

the middle part, but it is very difficult to characterize the trend at close wall region. Moreover, any correlations from linear curve fitting lack physical interpretation to the problem itself.

The next chapter focuses on developing a new reduced-order modeling method to calculate the air temperature profile in a square. The method should not only save computational cost, but also provide physical interpretation and better accuracy to the solutions.

Chapter 5: A Reduced-order Simulation Method for Air Temperature Calculation

5.1 Introduction on the POD Method

Although the simple linear curve fitting which saved computation time was able to capture the general trend of the air temperature field, the method's physical mechanisms is incomplete and lacks predictive capability (Rambo J., 2006). Therefore, it is useful to develop a new simulation method that requires less computation time compared to CFD simulation and has the capability to make prediction of temperature field in different settings.

The proper orthogonal decomposition (POD) was chosen as the reduced-order simulation to replace the above linear curve fitting. The POD method was first introduced by John Lumley (Berkooz et al. 1993). In other disciplines the same method was called as Karhunen-Loève decomposition or principal components analysis. It has several advantages as pointed out by Berkooz et al. (1993). (1) It is statistically based-extracting data from experiments and simulations. (2) Its analytical foundations supply a clear understanding of its capabilities and limitations. (3) It permits the extraction of the results.

In short, the method seeks to decompose a large degree of freedom system into a series of expansion:

$$v(x,t)=\sum_{i=1}^{m} a_i(t)\varphi_i(x) \tag{53}$$

where v can be any studied variables, such as velocity, temperature, etc.

φ is a family of modal basis of v.

a is the coefficient for the expansion, usually a function of time.

The search for good bases is the first step of constructing the expansion. A good set of bases makes the expansion efficient in terms of using as less number of m as possible. In order to make the basis to be optimal, it is equally the problem of finding a set of basis that is "most similar" to v. This can be explained from Figure 87. Assuming u is the vector to be decomposed, while ψ_1, ψ_2 and ψ_3 are the different candidates of POD basis φ. Neither ψ_1 or ψ_2 can represent u unless additional bases were introduced to offset their horizontal components. For ψ_3, it is most similar to u in the sense that no additional basis is necessary. Only a coefficient is needed to adjust the magnitude of ψ_3 to match u.

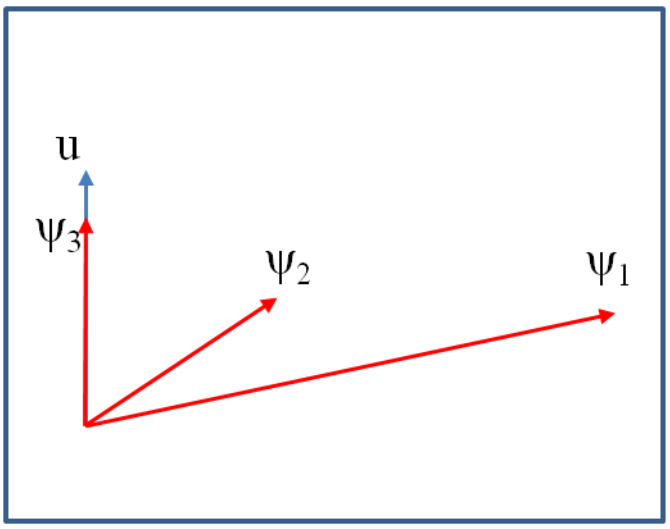

Figure 87: Indication of the search for the optimum basis of u

Thus, it is the same problem as to solve the following equations and to find φ:

$$\max \frac{|(v,\psi)|^2}{(\psi,\psi)} = \frac{\langle|(v,\varphi)|^2\rangle}{(\varphi,\varphi)} \tag{54}$$

The parentheses in the equation represent inner products. When the v and ψ are in the same direction the inner product of the two reaches maximum. If those two are perpendicular to each other, the inner product reduces to zero.

In some literatures, it is also common to use the following expression. One of the advantages to use this expression is to produce normalized basis:

$$\max\langle|(v,\varphi)|^2\rangle\text{-}\lambda(|\varphi|^2\text{-}1) \tag{55}$$

It is essential to have a restriction on the normalization in this extreme calculation. In Figure 87, ψ_3 is the worst basis of the three, however, without the normalization, it still can be the maximum of inner product due to its large magnitude.

For simplicity, several steps of extreme computing are skipped. For those who are interested in them, please refer to the spectral theory (Riesz et al., 1990).
It turns out that the base functions (φ) are the eigenfunctions of the integral equation (Hung and Tran, 1999):

$$\int C(x,x')\varphi(x')dx' = \lambda\varphi(x) \tag{56}$$

where the kernel *C* is given by:

$$C(x,x') = \frac{1}{N}\sum_{i=1}^{N} v_i(x)v_i(x') \tag{57}$$

Therefore, in short, the search for POD bases can be divided into two steps: construction of the kernel *C* and calculation of eigenvectors of the *C*.
Before we start to apply the POD to our air temperature simulation, there are two questions remain unanswered. How to guarantee that the series of expansion cover the entire span of u? How to prove that the series of expansion is the optimal one?

Completeness

By observing the kernel *C*, it is clear that the matrix is non-negative. Therefore, all the eigenvalues must be non-zero, i.e., $\lambda_i \geq 0$. Those eigenvectors corresponding to zero eigenvalues do not contribute to the entire kinetic energy of the space. The entire system space is hence reduced to be only formed by eigenvectors

corresponding to eigenvalues. There is no piece of information of *u* missing from the process. More detailed explanation can be obtained from the propositions 2.1 and 2.2 in Berkooz et al. (1991).

Optimality

The POD basis set is optimal for modeling or reconstructing *v*. Proposition 2.3 in Berkooz et al. (1993) was considered as the basis to the claim.

Proposition 2.3: Let v(x,t) be an ensemble member square integrable on Ω for almost every *t* and $\{\varphi_i, \lambda_i\}$ be the POD orthonormal basis set with associated eigenvalues. Let

$$v(x,t)=\sum_i a_i(t)\varphi_i(x) \tag{58}$$

be the decomposition with respect to this basis, where equality is almost everywhere. Let $\{\psi_i\}$ be an arbitrary orthonormal set such that

$$v(x,t)=\sum_i b_i(t)\psi_i(x) \tag{59}$$

Then the following hold:

1. $\langle a_i(t)a_j^*(t)\rangle=\delta_{ij}\lambda_i$, i.e. the POD coefficients are uncorrelated.
2. For every n we have $\sum_i^n\langle a_i(t)a_i^*(t)\rangle=\sum_i^n\lambda_i\geq\sum_i^n\langle b_i(t)b_i^*(t)\rangle$

This implies that, among all linear decompositions, this is the most efficient in the sense that, for a given number of modes the projection on the subspace used for modeling will contain the most kinetic energy possible in an average sense. In additional, the time series of the coefficient $a_i(t)$ are uncorrelated.

5.2 Application of the POD Method on the Natural Convection in an Enclosure

For the current problem, in order to obtain the POD modes for the air temperature field, matrix *C* should be calculated first as listed in Eq. (57). However it is impossible to obtain the expression of *v* in any mathematic form. The only available source of *v* is the numerical calculation results from CFD. Therefore, a technique called "snapshot" was applied to form the matrix C by utilizing the existing CFD simulation results. Nine sets of temperature fields and velocity fields were chosen to form the snapshot. The difference between each snapshot is the different Rayleigh numbers (see Eq. (8)), and they were created by changing the gravitational acceleration in each case.

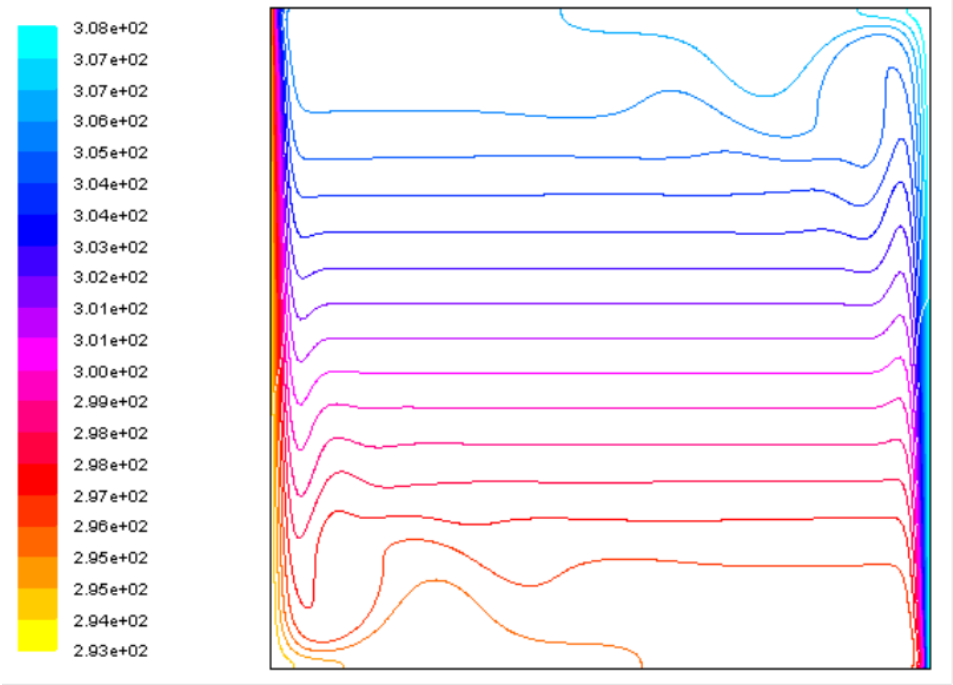

Figure 88: Isotherms of CFD snapshots (Ra ~ 10^6)

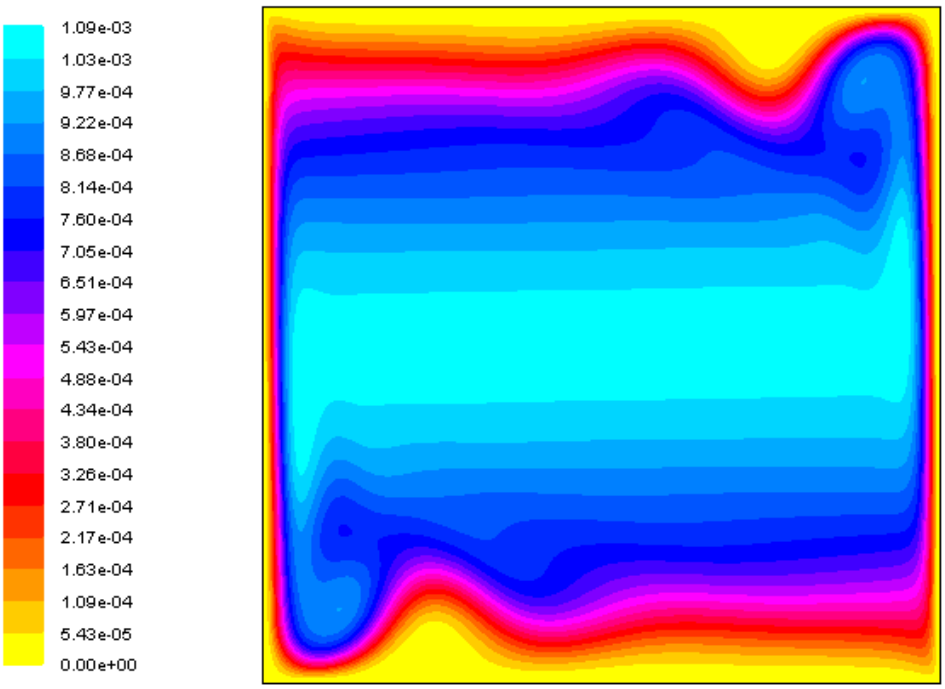

Figure 89: Streamlines of CFD snapshots (Ra ~ 10^6)

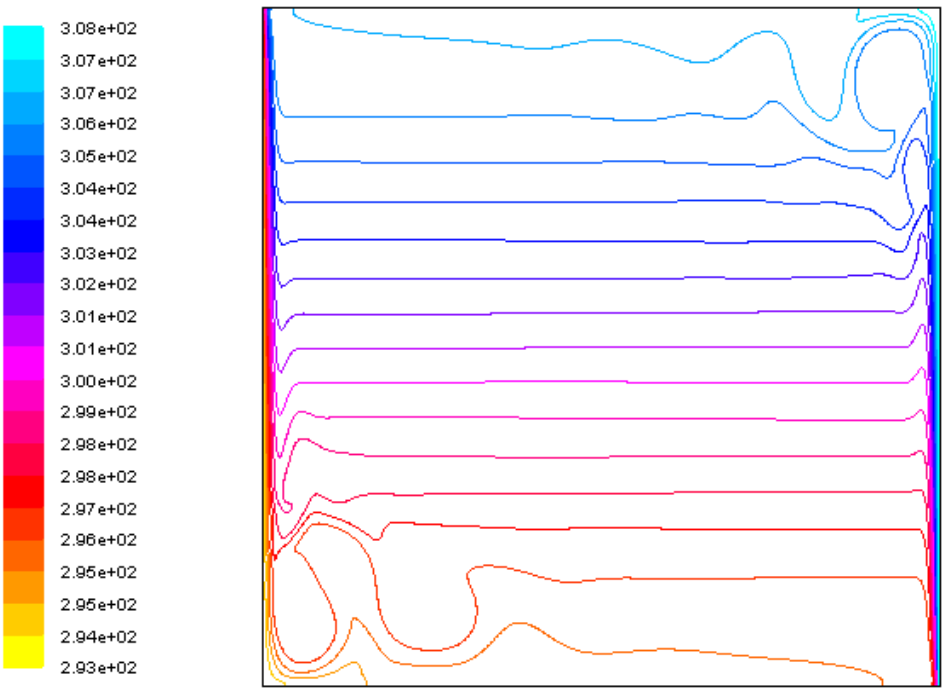

Figure 90: Isotherms of CFD snapshots (Ra ~ 10^7)

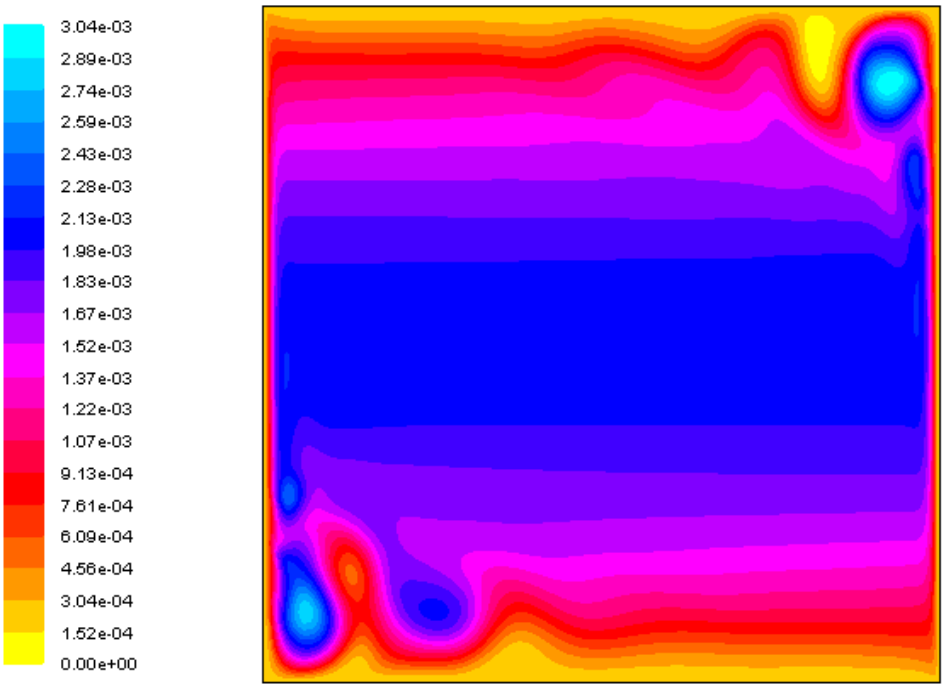

Figure 91: Streamlines of CFD snapshots (Ra ~ 10^7)

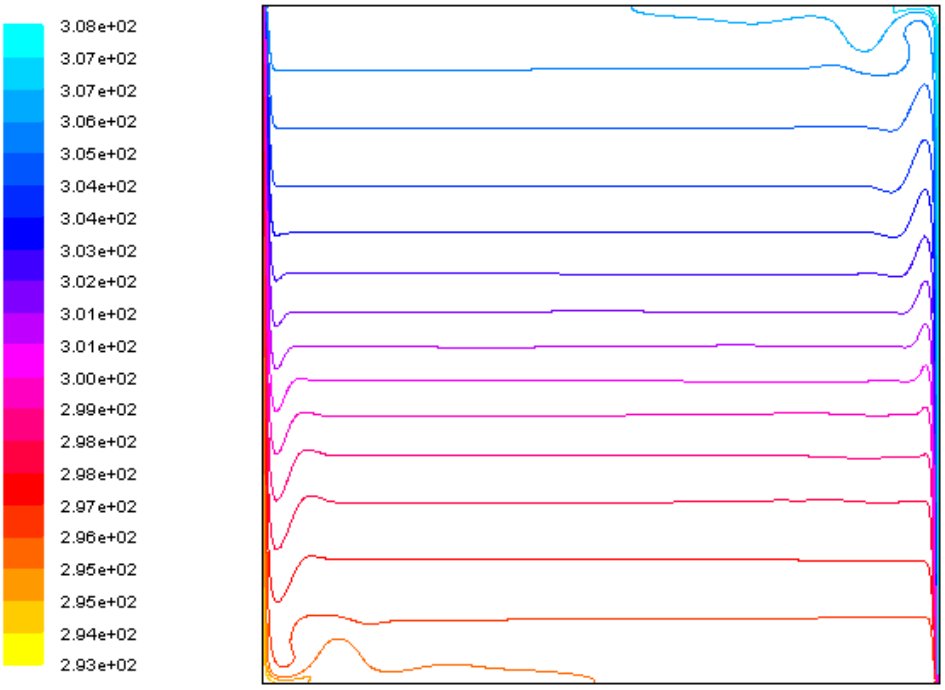

Figure 92: Isotherms of CFD snapshots (Ra ~ 10^8)

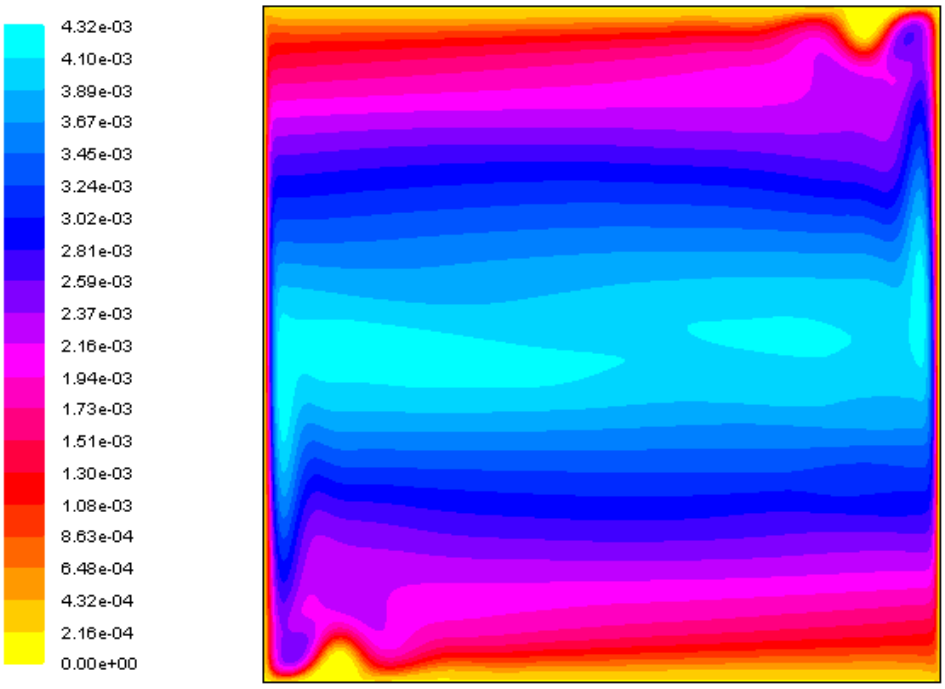

Figure 93: Streamlines of CFD snapshots (Ra ~ 10^8)

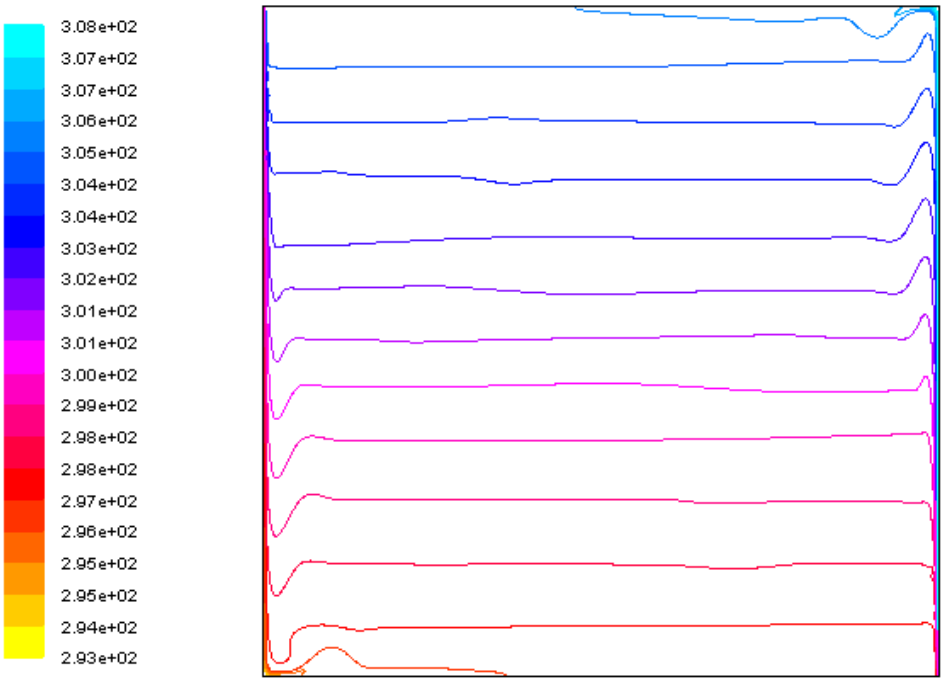

Figure 94: Isotherms of CFD snapshots (Ra ~ 10^9)

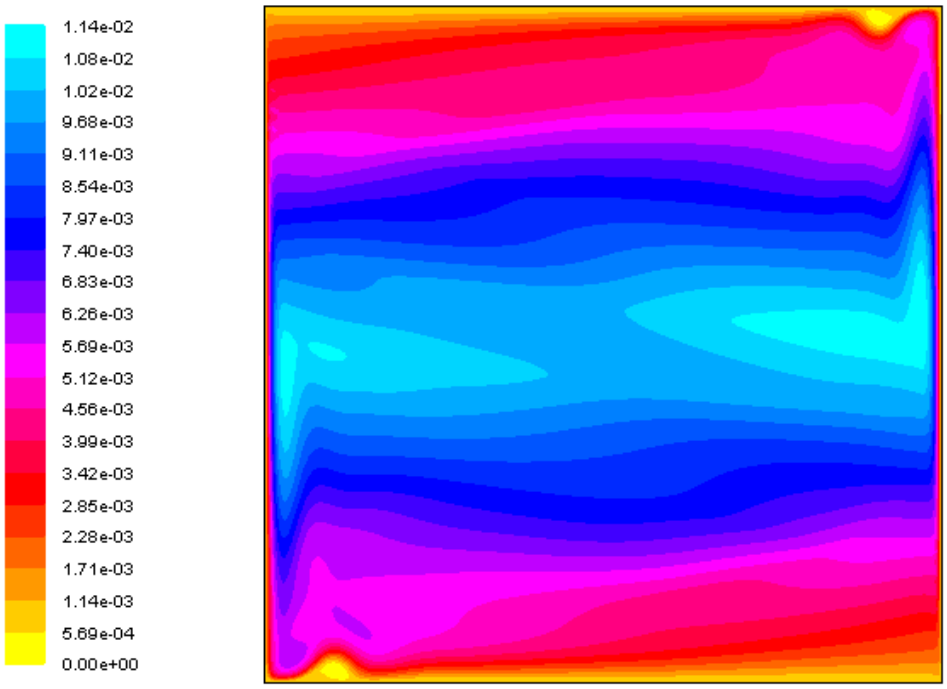

Figure 95: Streamlines of CFD snapshots (Ra ~ 10^9)

Figure 88 through Figure 95 present the isotherms (temperature) and streamlines (velocity) of four different Raleigh number cases. The range of Raleigh number varies from 10^6 to 10^9. With the increase of the Raleigh number, the maximum velocity of the air motion increased from 1.1×10^{-3} m/s to 1.1×10^{-2} m/s. From the figures of streamlines, it can be found that the maximum streamline is always located in the middle of the enclosure (For *x* and *y* velocities, it can be found from

Table **14** and Table 15 that the maximum velocities are located around the corners and close-to-wall region). Several rings representing air circulation motion exist in the enclosure, and the streamlines of each ring reduces from the most inner core to the most outer core. For the air temperature, in the lower Rayleigh number case, the laminar thermal boundary layer is thicker than the one in higher Rayleigh number case. This is due to an increased air velocity near the wall region in the high

Rayleigh number case. The motion of air is therefore intensified and breaks the thermal boundary layer near the wall. The same reason also helps to reduce the size of vortex-shaped temperature profile near the floor and ceiling in the high Rayleigh number case.

The resolution of the previous CFD output was ~75,000 cells. It had to be downgraded so that the dimension of the kernel matrix is within the capability of most software available for eigenvalue calculation. The new resolution was adjusted to be 15 times 15 (225 cells) based on the consideration of balancing between computational time and accuracy. Each temperature field represents a different Rayleigh number

In order to simplify the later eigenvalue calculation, each set of snapshots, i.e., temperature snapshots, u-velocity snapshots and v-velocity snapshots, was averaged at first. Then deviations from the mean value, called fluctuation terms, were sent to the POD calculation. For example,

$$T_i'_{@(1,1)} = T_{i\,@(1,1)} - \frac{1}{9}\sum_{i=1}^{9} T_{i\,@(1,1)} \tag{60}$$

Where (1, 1) is the coordinates of the cell, *i* is the i^{th} snapshot.

Table 14 through Table 16 are examples of the fluctuation terms matrices.

Table 14: Fluctuation terms of u-velocity snapshot

0.00147	0.00154	0.00165	0.00175	0.00190	0.00203	0.00212	0.00208	0.00201	0.00239	0.00323	0.00397	0.00246	0.00079	0.00378
0.00097	0.00088	0.00083	0.00077	0.00073	0.00073	0.00069	0.00067	0.00060	0.00028	0.00017	-0.00002	0.00027	0.00184	0.00000
0.00076	0.00081	0.00080	0.00076	0.00065	0.00056	0.00060	0.00075	0.00085	0.00050	-0.00044	-0.00023	0.00123	-0.00001	0.00017
0.00068	0.00085	0.00085	0.00085	0.00086	0.00085	0.00081	0.00080	0.00086	0.00094	0.00075	0.00041	0.00092	0.00060	0.00038
0.00061	0.00084	0.00081	0.00075	0.00070	0.00070	0.00071	0.00071	0.00070	0.00070	0.00074	0.00071	0.00072	0.00085	0.00034
0.00049	0.00076	0.00079	0.00078	0.00077	0.00071	0.00066	0.00066	0.00069	0.00072	0.00078	0.00082	0.00091	0.00088	0.00036
0.00029	0.00049	0.00045	0.00045	0.00045	0.00048	0.00050	0.00049	0.00047	0.00049	0.00053	0.00052	0.00060	0.00066	0.00024
0.00003	0.00008	0.00016	0.00017	0.00018	0.00017	0.00012	0.00008	0.00003	-0.00006	-0.00014	-0.00015	-0.00014	-0.00008	0.00000
-0.00025	-0.00067	-0.00065	-0.00060	-0.00058	-0.00056	-0.00052	-0.00050	-0.00048	-0.00040	-0.00032	-0.00028	-0.00035	-0.00044	-0.00022
-0.00041	-0.00092	-0.00094	-0.00087	-0.00080	-0.00078	-0.00077	-0.00076	-0.00078	-0.00082	-0.00088	-0.00086	-0.00089	-0.00082	-0.00039
-0.00046	-0.00071	-0.00063	-0.00070	-0.00073	-0.00072	-0.00072	-0.00073	-0.00073	-0.00074	-0.00077	-0.00076	-0.00080	-0.00081	-0.00047
-0.00048	-0.00070	-0.00079	-0.00041	-0.00070	-0.00088	-0.00079	-0.00073	-0.00074	-0.00080	-0.00084	-0.00082	-0.00091	-0.00092	-0.00050
-0.00023	-0.00026	-0.00119	0.00012	0.00042	-0.00051	-0.00081	-0.00066	-0.00053	-0.00050	-0.00058	-0.00064	-0.00072	-0.00078	-0.00051
-0.00015	-0.00162	-0.00025	0.00003	-0.00015	-0.00035	-0.00070	-0.00074	-0.00073	-0.00076	-0.00075	-0.00077	-0.00083	-0.00088	-0.00061
-0.00462	-0.00076	-0.00252	-0.00411	-0.00325	-0.00232	-0.00197	-0.00207	-0.00212	-0.00203	-0.00189	-0.00167	-0.00164	-0.00155	-0.00121

Table 15: Fluctuation terms of v-velocity snapshot

0.00155	0.00003	0.00003	0.00005	0.00005	0.00005	0.00002	-0.00005	0.00002	0.00021	0.00036	0.00023	-0.00169	0.00155	-0.00362
0.00653	0.00013	0.00011	0.00014	0.00017	0.00012	0.00001	-0.00018	0.00004	0.00084	0.00110	-0.00120	-0.00176	0.00262	-0.00912
0.00904	0.00003	0.00006	0.00006	0.00008	0.00009	0.00002	-0.00009	-0.00015	0.00021	0.00071	-0.00064	-0.00059	0.00090	-0.00998
0.01093	0.00004	0.00005	0.00004	0.00004	0.00003	0.00004	0.00002	-0.00009	-0.00006	0.00002	0.00002	-0.00019	-0.00028	-0.01119
0.01274	0.00000	0.00001	0.00002	0.00004	0.00004	0.00003	0.00001	0.00001	-0.00003	-0.00009	-0.00011	0.00007	-0.00048	-0.01273
0.01427	-0.00001	-0.00002	-0.00002	-0.00001	0.00001	0.00003	0.00003	0.00001	-0.00001	-0.00002	-0.00004	0.00001	-0.00036	-0.01424
0.01522	0.00000	-0.00001	-0.00001	0.00000	-0.00001	-0.00001	0.00002	0.00004	0.00003	0.00003	0.00002	-0.00002	-0.00024	-0.01547
0.01555	0.00008	-0.00002	-0.00003	-0.00003	-0.00002	-0.00001	-0.00001	-0.00001	0.00001	0.00004	0.00004	0.00003	-0.00006	-0.01611
0.01501	0.00025	0.00002	-0.00001	0.00000	0.00000	-0.00001	-0.00002	-0.00001	-0.00001	-0.00002	-0.00002	-0.00001	-0.00001	-0.01587
0.01385	0.00036	0.00000	0.00007	0.00004	0.00001	-0.00001	-0.00002	-0.00001	0.00001	0.00003	0.00003	0.00002	-0.00002	-0.01504
0.01239	0.00052	-0.00004	0.00011	0.00006	0.00001	-0.00001	-0.00001	-0.00002	-0.00002	-0.00002	-0.00002	-0.00001	0.00000	-0.01358
0.01093	0.00037	0.00012	-0.00004	-0.00004	0.00005	0.00001	-0.00002	-0.00005	-0.00005	-0.00004	-0.00003	-0.00002	-0.00001	-0.01184
0.01003	-0.00112	0.00093	0.00046	-0.00071	-0.00018	0.00012	0.00007	-0.00005	-0.00011	-0.00010	-0.00007	-0.00004	-0.00002	-0.00982
0.00941	-0.00246	0.00213	0.00097	-0.00122	-0.00083	0.00011	0.00021	0.00002	-0.00014	-0.00018	-0.00014	-0.00012	-0.00013	-0.00738
0.00404	-0.00160	0.00171	-0.00020	-0.00045	-0.00020	0.00001	0.00006	0.00000	-0.00005	-0.00005	-0.00004	-0.00003	-0.00004	-0.00195

Table 16: Fluctuation terms of temperature snapshot

-2.716	0.024	0.041	0.043	0.049	0.055	0.060	0.058	0.055	0.092	0.171	0.234	0.176	-0.122	0.033
-2.644	0.180	0.205	0.214	0.239	0.268	0.270	0.212	0.107	0.175	0.545	0.638	-0.075	-0.366	-0.331
-2.561	0.295	0.299	0.290	0.293	0.321	0.354	0.340	0.256	0.172	0.411	0.630	0.184	0.061	-0.344
-2.515	0.191	0.192	0.182	0.171	0.159	0.158	0.170	0.181	0.161	0.117	0.183	0.162	0.109	-0.424
-2.412	0.076	0.079	0.080	0.080	0.078	0.073	0.069	0.069	0.078	0.078	0.052	0.035	0.103	-0.501
-2.272	0.021	0.016	0.017	0.020	0.024	0.027	0.028	0.027	0.026	0.030	0.036	0.012	0.029	-0.549
-2.124	-0.036	-0.040	-0.041	-0.043	-0.046	-0.047	-0.047	-0.046	-0.047	-0.047	-0.043	-0.042	-0.042	-0.633
-1.912	0.005	-0.003	-0.003	-0.003	-0.003	-0.002	-0.002	-0.001	0.001	0.003	0.002	0.003	-0.005	-0.664
-1.699	0.015	0.014	0.015	0.019	0.020	0.020	0.020	0.020	0.018	0.015	0.012	0.014	0.010	-0.734
-1.505	-0.008	0.017	-0.001	0.008	0.012	0.011	0.012	0.014	0.018	0.023	0.026	0.029	0.021	-0.815
-1.321	-0.066	-0.015	-0.043	-0.063	-0.062	-0.055	-0.056	-0.061	-0.068	-0.072	-0.069	-0.073	-0.076	-0.950
-1.138	-0.117	-0.204	-0.222	-0.137	-0.178	-0.199	-0.189	-0.178	-0.178	-0.189	-0.186	-0.208	-0.213	-1.128
-0.998	-0.034	-0.217	-0.625	-0.390	-0.160	-0.251	-0.329	-0.337	-0.304	-0.276	-0.249	-0.275	-0.281	-1.255
-0.942	0.365	-0.007	-0.677	-0.542	-0.162	-0.106	-0.224	-0.280	-0.273	-0.245	-0.198	-0.205	-0.192	-1.274
-0.666	0.117	-0.200	-0.266	-0.187	-0.108	-0.073	-0.076	-0.078	-0.072	-0.065	-0.046	-0.052	-0.044	-1.105

The matrix *C* was then formed by using the following equation:

$$C_{ij} \equiv \frac{1}{nt}(T_i', T_j')_\Omega \tag{61}$$

where: *nt* is the number of snapshots

(,) is the inner product.

Table 17 through Table 19 are the results of kernel matrices of velocities and temperature. Each kernel matrix is symmetric which can be derived from Eq. (62)

$$C_{ij} \equiv \frac{1}{nt}(T_i', T_j')_\Omega = \frac{1}{nt}(T_j', T_i')_\Omega \equiv C_{ji} \tag{62}$$

Table 17: Kernel matrix of u-velocity

2.90E-05	2.50E-05	1.92E-05	1.62E-05	9.50E-06	-5.97E-06	-1.99E-05	-2.39E-05	-4.91E-05
2.50E-05	2.31E-05	1.82E-05	1.57E-05	8.35E-06	-5.75E-06	-1.84E-05	-2.21E-05	-4.42E-05
1.92E-05	1.82E-05	1.77E-05	1.55E-05	6.76E-06	-4.91E-06	-1.60E-05	-1.98E-05	-3.66E-05
1.62E-05	1.57E-05	1.55E-05	1.65E-05	6.99E-06	-4.53E-06	-1.49E-05	-1.81E-05	-3.34E-05
9.50E-06	8.35E-06	6.76E-06	6.99E-06	6.57E-06	-2.09E-06	-7.99E-06	-9.59E-06	-1.85E-05
-5.97E-06	-5.75E-06	-4.91E-06	-4.53E-06	-2.09E-06	3.54E-06	4.73E-06	4.46E-06	1.05E-05
-1.99E-05	-1.84E-05	-1.60E-05	-1.49E-05	-7.99E-06	4.73E-06	1.77E-05	2.05E-05	3.43E-05
-2.39E-05	-2.21E-05	-1.98E-05	-1.81E-05	-9.59E-06	4.46E-06	2.05E-05	2.77E-05	4.09E-05
-4.91E-05	-4.42E-05	-3.66E-05	-3.34E-05	-1.85E-05	1.05E-05	3.43E-05	4.09E-05	9.62E-05

Table 18: Kernel matrix of v-velocity

4.63E-04	4.63E-04	3.59E-04	2.21E-04	9.00E-05	-1.23E-04	-3.43E-04	-4.22E-04	-7.09E-04
4.63E-04	4.63E-04	3.59E-04	2.21E-04	9.00E-05	-1.23E-04	-3.43E-04	-4.22E-04	-7.09E-04
3.59E-04	3.59E-04	2.91E-04	1.86E-04	7.67E-05	-9.83E-05	-2.74E-04	-3.39E-04	-5.60E-04
2.21E-04	2.21E-04	1.86E-04	1.26E-04	5.14E-05	-6.30E-05	-1.75E-04	-2.15E-04	-3.52E-04
9.00E-05	9.00E-05	7.67E-05	5.14E-05	3.63E-05	-2.27E-05	-7.61E-05	-9.66E-05	-1.49E-04
-1.23E-04	-1.23E-04	-9.83E-05	-6.30E-05	-2.27E-05	3.54E-05	9.25E-05	1.12E-04	1.90E-04
-3.43E-04	-3.43E-04	-2.74E-04	-1.75E-04	-7.61E-05	9.25E-05	2.62E-04	3.24E-04	5.32E-04
-4.22E-04	-4.22E-04	-3.39E-04	-2.15E-04	-9.66E-05	1.12E-04	3.24E-04	4.04E-04	6.55E-04
-7.09E-04	-7.09E-04	-5.60E-04	-3.52E-04	-1.49E-04	1.90E-04	5.32E-04	6.55E-04	1.10E-03

Table 19: Kernel matrix of temperature

8.12	8.12	-1.52	-0.51	-1.23	-2.29	-3.03	-3.23	-4.42
8.12	8.12	-1.52	-0.52	-1.23	-2.28	-3.03	-3.23	-4.43
-1.52	-1.52	2.61	1.95	1.33	0.35	-0.42	-0.69	-2.09
-0.51	-0.52	1.95	1.90	1.16	0.09	-0.64	-0.79	-2.64
-1.23	-1.23	1.33	1.16	1.24	0.57	-0.03	-0.20	-1.63
-2.29	-2.28	0.35	0.09	0.57	0.92	0.92	0.88	0.85
-3.03	-3.03	-0.42	-0.64	-0.03	0.92	1.59	1.77	2.86
-3.23	-3.23	-0.69	-0.79	-0.20	0.88	1.77	2.13	3.35
-4.42	-4.43	-2.09	-2.64	-1.63	0.85	2.86	3.35	8.15

Matlab® (MathWorks, Inc, 2008) was used to calculate the eigenvalues of the kernel matrix *C*. The built-in singular value decomposition (SVD) function was applied to return the eigenvalues and the corresponding eigenvectors. The eigenvectors are in fact the POD bases according to Eq. (56). The eigenvalues in each plot are sorted from high to low. As previously mentioned, when the eigenvalue becomes zero, it has no impact on the system anymore. All three eigenvalue spectrum figures show that the eigenvalues approach zero within the first nine ones. It proves that nine snapshots are enough in terms of capturing most of the system kinetic energy.

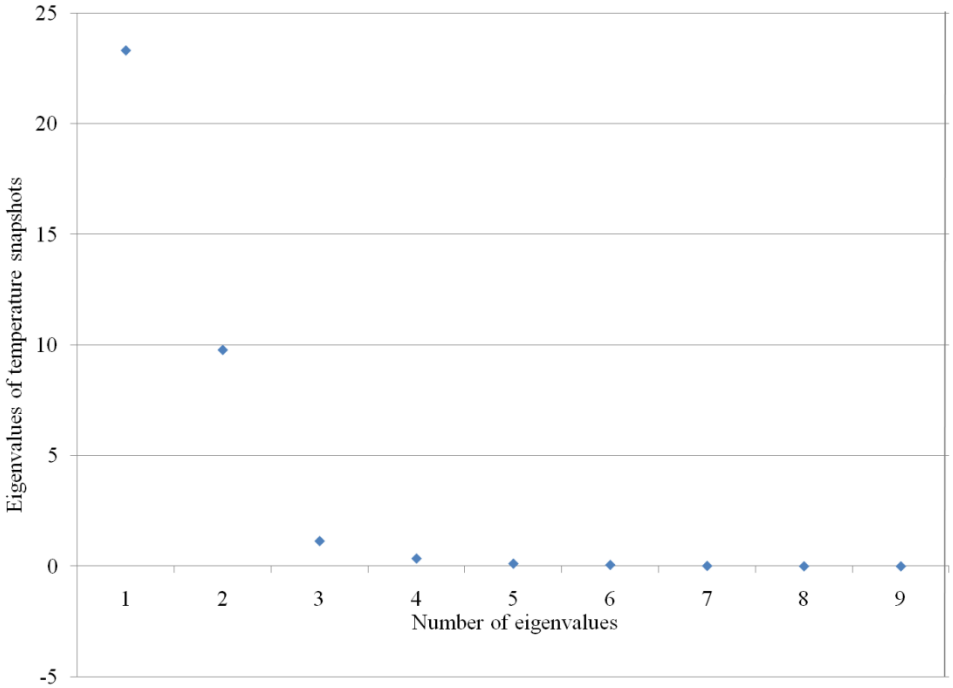

Figure 96: Eigenvalue spectrum of temperature snapshots

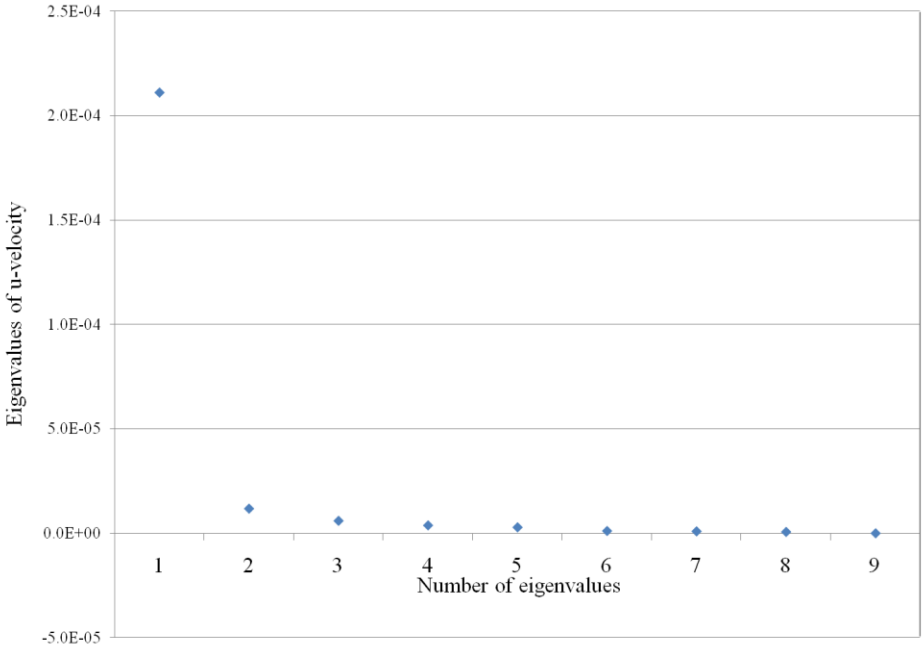

Figure 97: Eigenvalue spectrum of u-velocity snapshots

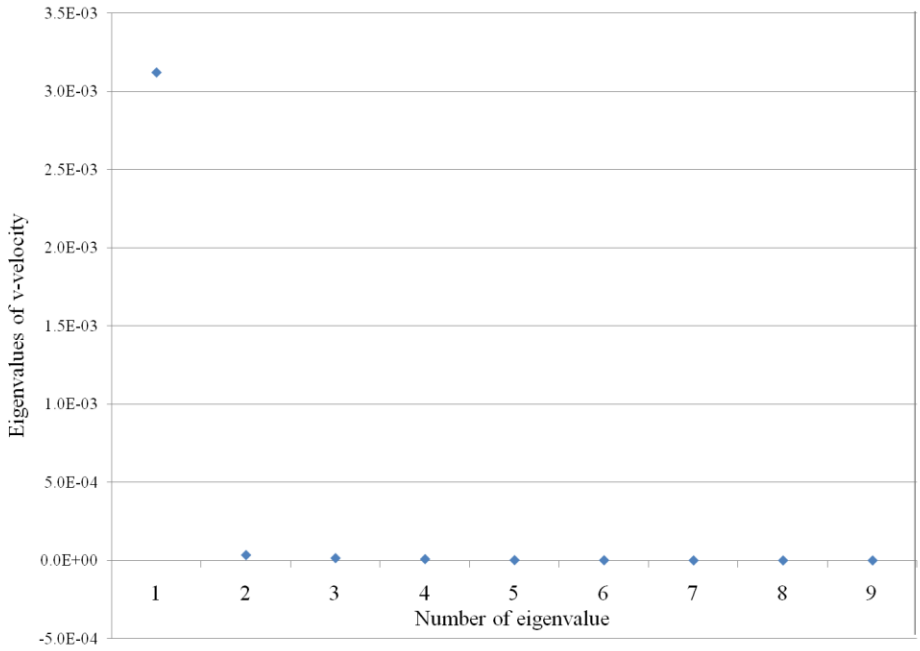

Figure 98: Eigenvalue spectrum of v-velocity snapshots

5.3 Introduction on the Galerkin Projection Method

The proper orthogonal decomposition provides the POD basis from the snapshots method. The next step is to find the coefficients in the expansion (Eq. (53)). A method called Galerkin projection is considered to be a standard approach to obtain the coefficients of the POD basis. The approach is to project the governing equations on the modal subspace and then solve the governing equations, usually in the form of ODE equations, to obtain the coefficients.

Consider the governing equations for the natural convection problem (Park and Jung, 2000):

$$x=\frac{x^*}{d_x},\ y=\frac{y^*}{d_y},t=\frac{\kappa t^*}{d_y^2},v=\frac{d_y v^*}{\kappa},T=\frac{T^*-T^*_{cold}}{T^*_{hot}-T^*_{cold}},\ P'=\frac{d_y^2 P^*}{\rho\kappa^2} \tag{63}$$

Eq. (63) defines the dimensionless quantities used in the following governing equations (Eq. (64) through Eq. (66)), where superscript asterisk is used to denote dimensional quantities.

$$\nabla\cdot v=0 \tag{64}$$

$$\frac{\partial v}{\partial t}+v\cdot\nabla v=-\nabla P+Pr\nabla^2 v+RaPrTj \tag{65}$$

$$\frac{\partial T}{\partial t}+\vec{u}\cdot\nabla T=\frac{1}{\rho c_p}\nabla^2 T \tag{66}$$

where: *v,T* represent the velocity and temperature,

Pr is the Prandtl number

Ra is the Rayleigh number.

The projection can be defined as the following:

$$\int_{\Omega} \varphi\cdot(\frac{\partial v}{\partial t}+v\cdot\nabla v+\nabla P-Pr\nabla^2 v-RaPrTj\,)dx=0 \tag{67}$$

Assuming

$$v=\sum_{n=1}^{NT} a_n(t)\phi_{(n)}(x,y) \tag{68}$$

$$T=\sum_{n=1}^{NT} b_n(t)\varphi_{(n)}(x,y) \tag{69}$$

to be the expansion of velocity and temperature field, where ϕ and φ are POD modes of velocity and temperature

a_n and b_n are the coefficients need to be determined by using Galerkin Projections.

After applying the projection, the above continuity, momentum and energy equations become the following forms (The continuity and momentum equations are combined into one equation) (Park and Jung 2000):

$$M_j\frac{da_j}{dt}+\sum_{l=1}^{NM}\sum_{m=1}^{NM} a_l a_m Q_{jlm}+Pr\sum_{n=1}^{NM} H_{jl}a_l-RaPr\sum_{n=1}^{NT} b_l S_{jl}=0 \tag{70}$$

$$N_j\frac{db_j}{dt}+\sum_{l=1}^{NM}\sum_{m=1}^{NT} a_l b_m R_{jlm}+\sum_{n=1}^{NT} L_{jl}b_l=0 \tag{71}$$

where:

$$M_j=\int_{\Omega}\phi_{(j)}\cdot\phi_{(j)}d\Omega \tag{72}$$

$$Q_{jlm}=\int_{\Omega}\phi_{(j)}\cdot\left(\phi_{(j)}\cdot\nabla\phi_{(m)}\right)d\Omega \tag{73}$$

$$H_{jl}=\int_{\Omega}(\nabla\phi_{(j)}):(\nabla\phi_{(l)})^T d\Omega \tag{74}$$

$$S_{jl}=\int_{\Omega}\varphi_{(l)}\,\phi^{v}_{(j)}d\Omega \tag{75}$$

$$N_{j}=\int_{\Omega}\varphi^{2}_{(j)}\,d\Omega \tag{76}$$

$$R_{jlm}=\int_{\Omega}(\phi_{(l)}\cdot\nabla\varphi_{(m)})\varphi_{(j)}\,d\Omega \tag{77}$$

$$L_{jl}=\int_{\Omega}\nabla\varphi_{(l)}\cdot\nabla\varphi_{(j)}\,d\Omega \tag{78}$$

The left-hand side terms in Eq. (72) through Eq. (78) can be obtained by taking the gradient and inner product operations of the POD basis, φ and ϕ. Therefore, the Galerkin projection has been simplified to solve two sets of ODE functions (Eq. (70) and Eq.(71)). There are two sets of unknowns ($a_n(t)$, $b_n(t)$), and two sets of ODE equations. The problem is closed. Matlab was used to solve the two sets of equations.

5.4 POD Simulation Results and Validations

Since the air temperature is more important in terms of obtaining operative temperature, the POD simulation results will be focused on reporting the temperature profile. Eq. (79) can be used to construct the temperature field. $\overline{T}$ is the matrix of average temperature in different snapshots. b_i is the coefficient obtained from Galerkin projection. T'_{PODi} is the matrix of the i^{th} POD basis developed based on fluctuation items.

$$T_{POD}=\overline{T}+\sum_{i=1}^{NT} b_i \cdot T'_{PODi} \tag{79}$$

Figure 99 plots the average temperature matrix from nine snapshots. Compared to other CFD simulation results, it captures the major trend of temperature profile. The temperature close to the wall region has much better accuracy than using the linear curve fitting correlations.

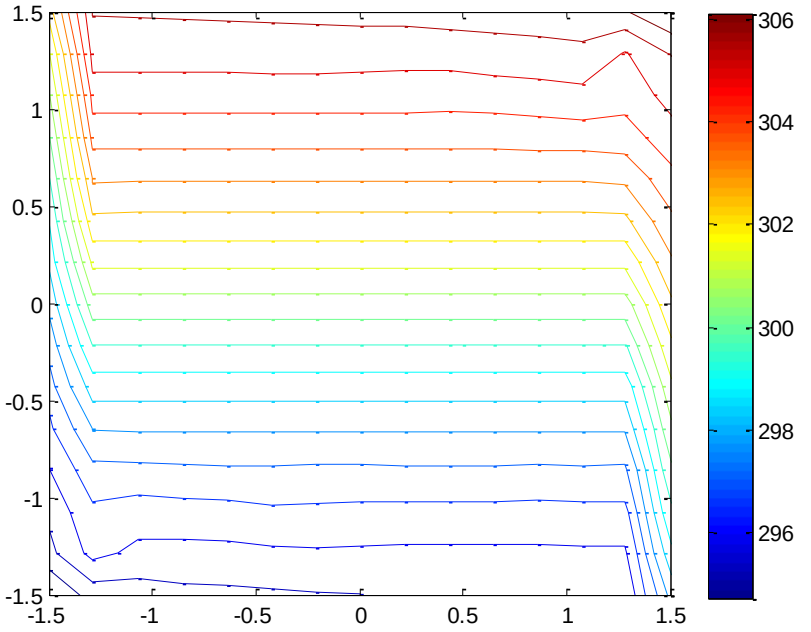

Figure 99: The matrix of average temperature

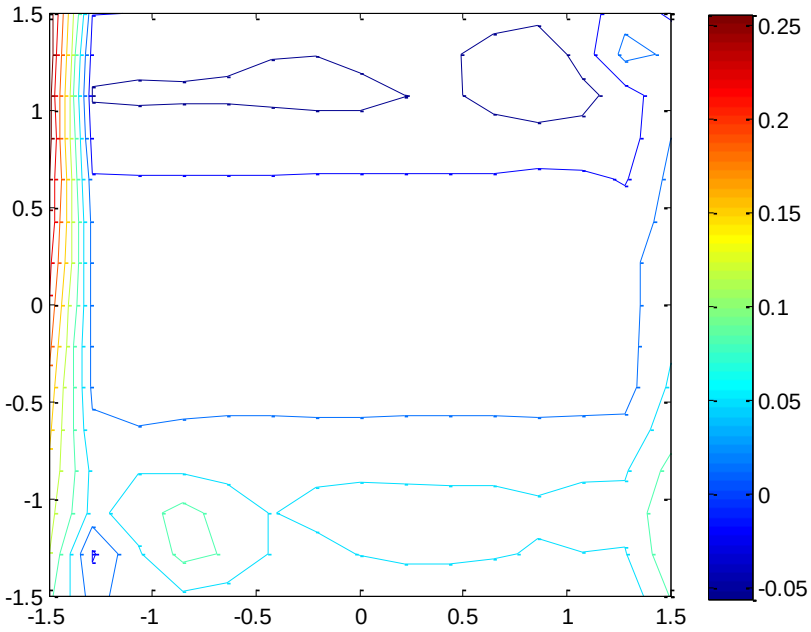

Figure 100: Temperature POD mode #1

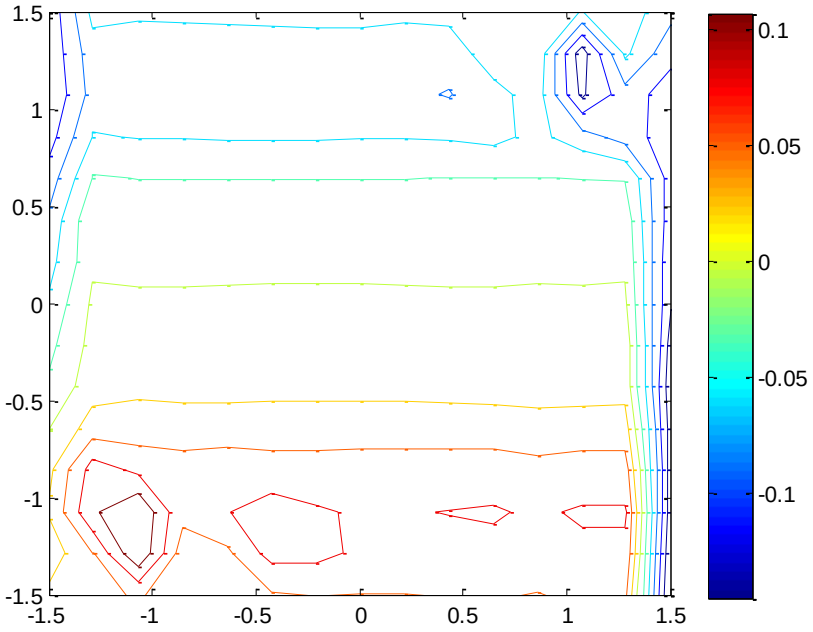

Figure 101: Temperature POD mode #2

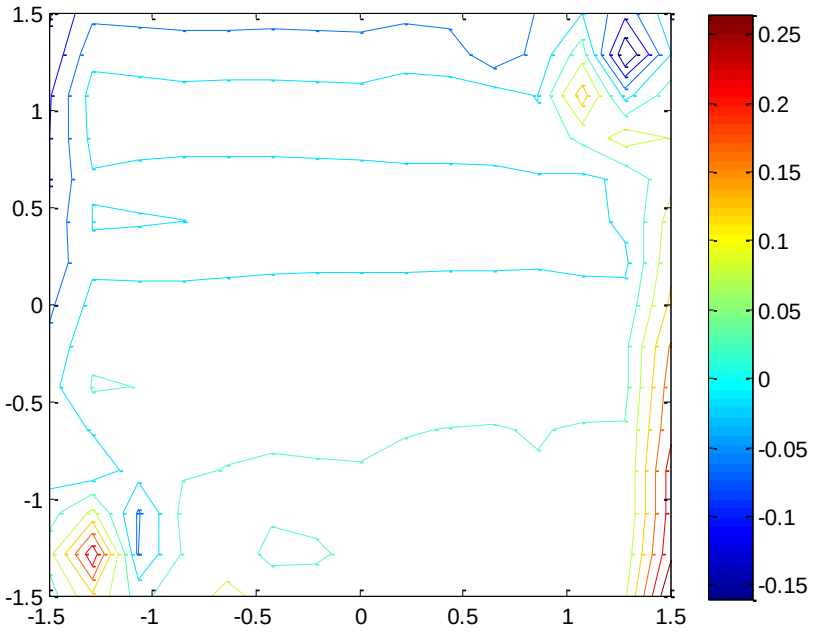

Figure 102: Temperature POD mode #3

Figure 100 through Figure 102 are the matrices of the first three eigenvectors plotted in the dimension of the 3 m by 3 m space. The eigenvectors are demonstrated in the form of contours of the fluctuation temperatures.

In order to verify the correctness of the POD simulations, two case of POD calculation results were compared to those from CFD simulation. Case 1 is solving for air temperature inside a 3 m by 3 m square enclosure when the Rayleigh number is 10^6. Case 2 is solving for the same problem when the Rayleigh number is 10^9.

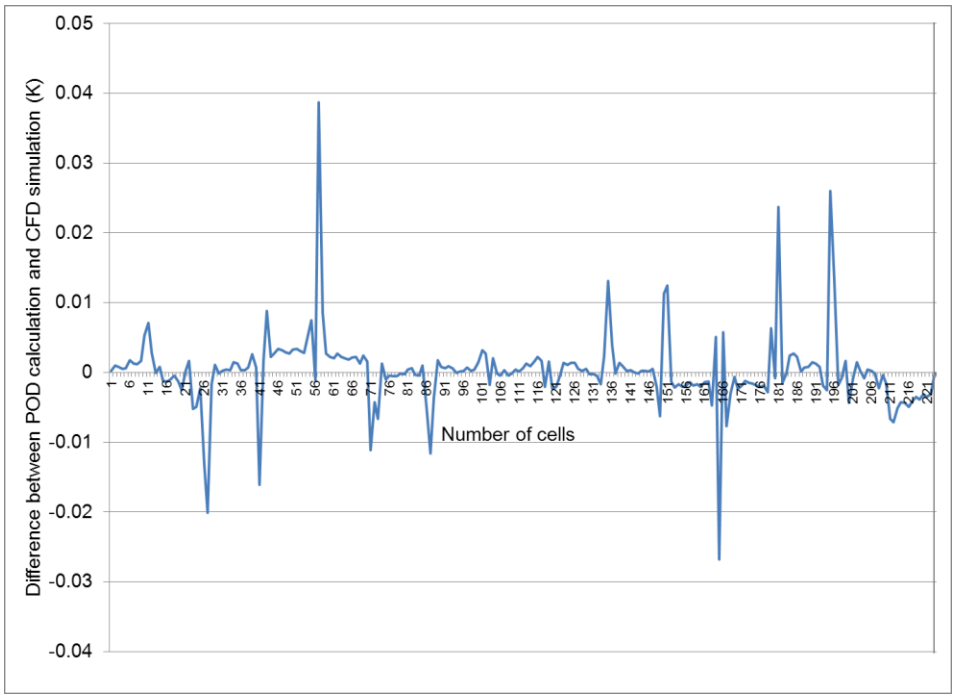

Figure 103: Comparison of POD calculation and CFD simulation (Ra = 10^6)

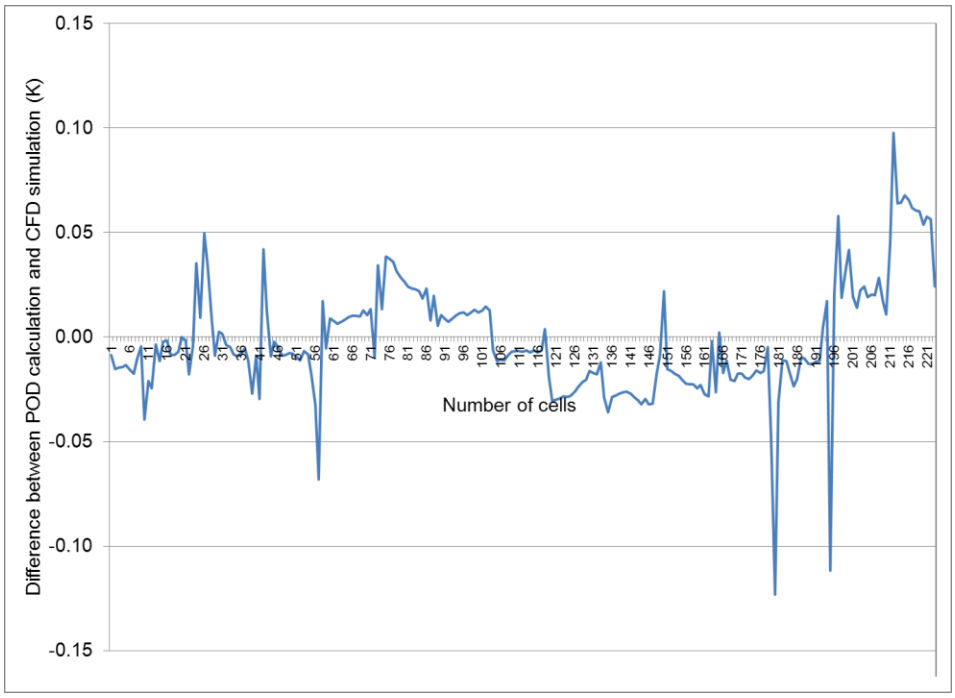

Figure 104: Comparison of POD calculation and CFD simulation (Ra = 10^9)

Figure 103 and Figure 104 demonstrate the comparison results. The 3 m by 3 m enclosure was divided into 225 cells. The x-axis represents the 225 cells. For example, the top left cell is number 1, the rightmost cell of the top row is number 15, and the right bottom cell is number 225. The temperature results in each cell were compared to those from CFD simulation. Both POD cases show good agreement to the CFD simulations. In case one, the maximum deviation is only 0.04 K, while in case 2, the maximum deviation is around 0.1 K. It demonstrates that the POD calculation provides enough accuracy compared with CFD calculation. Considering the fact that it takes only several minutes for the Matlab codes to solve all the ODE functions and output the results, the benefit of using POD is very clear. However, the fast speed depends on the existence of snapshots. The first preparation of snapshots may take a week, and then POD calculation can solve any problem within the range of snapshots.

The air temperature calculated from the POD method was then combined with the MRT simulation results to obtain simulated operative temperatures. Figure 105 demonstrates the comparison of OTs calculated from POD modeling and those from experiments. Since the POD simulation results are very close to the CFD simulation, the comparison shares the same general trend as that shown in Figure 86. The largest discrepancy (1.1 K) between simulation and experiments comes from OT 3, and the smallest discrepancy (0.1 K) comes from OT 4. The detailed discussion of the comparison has been conducted in 4.3.5.

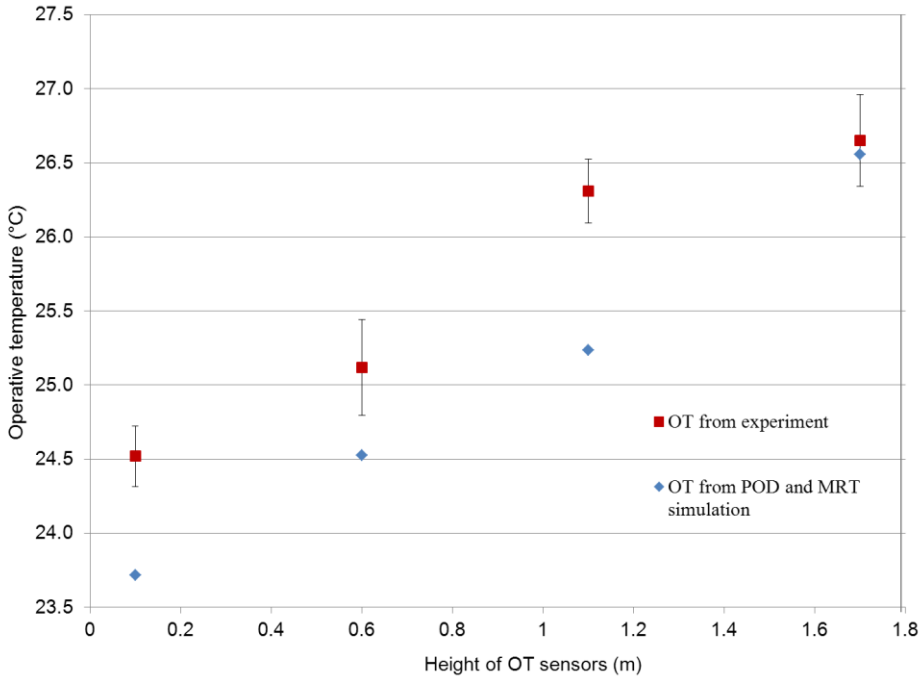

Figure 105: Comparison of POD simulated OT and experimental results

Chapter 6: Summary and Conclusions

6.1 SSLC System Using Two Vapor Compression Cycles

The SSLC system using R-410A as its working fluid has been theoretically investigated. Under the ARI standard ambient condition for air-conditioning application (35°C, 44% RH), a 30% energy savings was calculated for the SSLC system as compared to the conventional air-conditioning system. It was also found that the energy savings of the SSLC system varied depending upon ambient conditions. The hot and dry climate tends to have the maximum energy savings potential. The total displacement volumes of the compressors in the SSLC system were estimated to be 25% smaller than that in the baseline system. In order to address the larger air flow rate requirement in the SSLC system, a new air distribution method with a single-bank evaporator design was proposed to replace the conventional designs. The simple estimation using fan laws demonstrated that the SSLC system could reduce the fan motor power by 30% as compared to the baseline system. In order to compare the heat exchanger cost, in-house HX design software was used to optimally design the heat exchangers of the SSLC system and to estimate its total heat transfer area. The design shows that the heat exchangers of the SSLC system can have 13% smaller total heat transfer area than that of the baseline. This design example means that the SSLC system can save energy without increasing heat exchanger and compressor cost.

However, such a system has still limited independence of varying sensible to latent load ratio and the extra cost of an internal heat exchanger.

6.2 SSLC System Using One Vapor Compression Cycle and Desiccant Wheel

An experimental facility for SSLC system using one VCS and one solid DW was constructed. The experimental results of the SSLC system with a single condenser (gas cooler) demonstrated a limited COP improvement, which was 7% for both R-410A and CO_2 systems, when the DW regeneration temperature was set at 50°C. Although bigger improvement was recorded at the 45°C regeneration temperature case, which were 32% for CO_2 and 34% for R-410A, such improvement could not be provided by the DW. Two challenges, heat of adsorption and excessive high side pressures, were identified as the reasons for the reduction of the COP of the SSLC systems. To address the second issue, the idea of dividing condensers (or gas coolers) resulted in a reduced high side pressure and a reduced refrigerant outlet temperature. This led to the COP improvement of 20% and 44% for R-410A and CO_2 systems, respectively. Simulation results show that the additional evaporative cooling further improves the system performance. The CO_2 system had more benefits from using the evaporative cooling than the R-410A system, which was supported by a 16.8% COP improvement for the CO_2 system as compared to a 4.8% COP improvement for the R-410A system. The reason for the CO_2 system outperforming R-410Awas that the operating condition of the gas cooler (condenser) was shifted to a lower inlet air temperature that was more favorable to CO_2 refrigerant. The DW-assisted SSLC technology also could be adopted for the DOS system. Application of both SW and EW in addition to the dividing heat exchanger and the evaporative cooling was investigated. It was concluded that the SW was not suitable for the DW-assisted SSLC systems. This was because the SW lowered the heat generation from

the vapor compression cycle, making it hard to match the hot air requirement for the regeneration of the DW. On the other hand, the EW performed well because it not only lowered the cooling requirement of the vapor compression cycle, but also lowered the heat requirement for DW regeneration. The ratio of heating to cooling could be used as a measure to determine the feasibility of different configurations of a DW-assisted SSLC system.

6.3 The low ΔT heat exchanger test

A low ΔT heat exchanger test facility has been developed in a CEEE office. Four operative temperature sensors were built and applied in the test for measuring the thermal comfort created by both the baseline fan-coil unit and the low ΔT heat exchangers. The baseline fan-coil unit had a hot water temperature of 80°C. The unit created 3.24 K temperature difference between occupants head and feet which should be considered as uncomfortable. Although the hot water temperature was high, the temperature at occupant's feet was still out of the thermal comfort zone.

On the other hand, the low ΔT heat exchanger had a hot water temperature of only 35°C. The additional radiative heat transfer from the heat exchanger helped create a much better thermally comfortable environment. The temperature difference between occupant's head and ankle was reduced to only 2.0 K. Moreover, almost all the operative temperature measured during the test fell in the ASHRAE thermal comfort zone.

The experimental results prove the statement that low ΔT heat exchanger is able to provide better thermal comfort for the given conditions with a much lower temperature difference between air and hot fluid.

6.4 Modeling the operative temperature field in an office setting

The operative temperature field in a 3 m by 3 m by 3 m office setting was simulated. The model was able to calculate both the MRT and air temperature everywhere in the office. It provided reasonable accuracy compared with the experimental data. Specifically, when the low ΔT heat exchanger was off, the average deviation between modeling results and experimental results was 0.7 K. When the low ΔT heat exchanger was on, the average deviation was reduced to only 0.4 K. The air temperature correlations obtained from CFD simulation were applied to the case when the heat exchanger was on and they helped to reduce the deviation. The eight-surface radiation model was proved to be adequate to predict MRT for sensors located at higher positions. For those sensors whose radiative heat transfer was blocked by the furniture, the model failed to provide a good prediction. Future work on more room-specific MRT calculation model is necessary for a better simulation.

Although the curve fitting correlations from the CFD simulation provides good results for air temperature calculation, the computational cost for the CFD simulation is expensive. It takes a computer with Duo Core 2.66 GHz CPU and 2 G RAM over 24 hours to obtain the isotherms and streamlines based on one set of wall temperatures, such as a hot wall temperature of 35°C and a cold wall of 20°C. Every change of boundary conditions requires a run of CFD simulation. Besides high computation cost, another problem arising from using the correlations is that large deviations may exist locally such as in close proximity to the wall. A method with

more sophisticated techniques other than the curve fitting correlation while less computational intensive is required to address the above issues.

6.5 A Reduced-order Simulation Method for Air Temperature Calculation

A reduced-order simulation method, called proper orthogonal decomposition (POD), was applied to replace the air temperature by using curve fitting correlations. The objective is to calculate the air temperature in the form of a series of expansion. Snapshots from CFD simulation results were created one time in the beginning of the calculation, and POD was used to find the optimal bases to the expansion. Galerkin projection was then applied to project governing equations onto the bases and to obtain the coefficients for the bases by solving ODE equations. Two cases of air temperature in a cubic enclosure problem with different Rayleigh numbers were solved by the POD method and their results were compared to direct CFD simulations. The maximum deviation for the lower Rayleigh number case was only 0.04 K and the one for higher Rayleigh number case was around 0.1 K.

The POD method not only provides higher accuracy results than using curve fitting correlations, but also saves computational time of the problem from around 24 hours by CFD simulation to only minutes of ODE equations solving.

Chapter 7: List of major contributions and future work

7.1 List of major contributions

A study on SSLC systems and their major component, the low ΔT heat exchanger, is presented in this dissertation and it provides a comprehensive understanding on the energy saving potential and thermal comfort of such systems. The detailed contributions are listed as follows:

Exploration of energy saving potential of the SSLC systems:

- Designed, fabricated and tested an SSLC air conditioning system and compared its performance to a conventional system
- Compared the performance of SSLC systems using two refrigerants, R-410A and CO_2
- Based on experimental results, established models to simulate SSLC systems
    - Simulated SSLC system performance under different ambient conditions
    - Optimized the vapor compression cycle operation under each ambient condition
    - Explored maximum energy saving options (configurations) of an SSLC system

Thermal comfort study of the low ΔT heat exchanger:

- Established a low ΔT heat exchanger test facility with sensors for operative temperature measurement
- Compared the thermal comfort zone created by the baseline fan-coil unit and low ΔT heat exchanger system

- Developed a software tool to simulate the thermal comfort zone in an office setting
    - Simulate natural convection by a commercial CFD tool and obtain 2D air temperature field in the conditioned space
    - Simulate radiation cooling (heating) and obtain 3D mean radiation temperature field in the conditioned space
- Developed a reduced-order POD model to replace the CFD simulation of air temperature in the conditioned space and verify the POD model by comparing its results to the original CFD model

7.2 List of related publications

Peer-reviewed Journal papers:

Ling, J., Hwang, Y., Radermacher, R., 2010, Theoretical study on separate sensible and latent cooling air-conditioning system, International Journal of Refrigeration, vol. 33 (3), pp. 510-520

Ling, J., Kuwabara, O., Hwang, Y., Radermacher, R., 2010, Enhancement of the separate sensible and latent cooling air-conditioning systems by divided heat exchangers, Journal of Refrigeration and Air-conditioning, vol. 8(13), pp. 153-159

Ling, J., Kuwabara, O., Hwang, Y., Radermacher, R., 2010, Experimental evaluation and performance enhancement of desiccant assisted separate sensible and latent cooling air-conditioning system, International Journal of Refrigeration (in Press, available online 22 December 2010)

Conference papers:

Ling, J., Hwang, Y., Radermacher, R., 2008, Theoretical study on separate sensible and latent cooling air-conditioning system, International Refrigeration and Air Conditioning Conference at Purdue, July 14-17, 2008

Ling, J., Kuwabara, O., Hwang, Y., Radermacher, R., 2010, Enhancement of the separate sensible and latent cooling air-conditioning systems, International Refrigeration and Air Conditioning Conference at Purdue, July 12-15, 2010

Kuwabara O., **Ling J.,** Hwang, Y., Radermacher R., 2010, Experimental evaluation of separate sensible and latent cooling air-conditioning system integrated with

desiccant wheel, International Refrigeration and Air Conditioning Conference at Purdue, July 12-15, 2010

Ling, J., Kuwabara, O., Hwang, Y., Radermacher, R., 2011, Enhancement options for Separate Sensible and Latent Cooling Air-Conditioning Systems, The 23rd IIR International Congress of Refrigeration at Prague, August, 2011

Magazine:

Hwang, Y., **Ling, J.,** 2009, Estudio teórico del sistema de aire acondicionado con enfriamiento separado sensible y latente, Frío-calor y aire acondicionado, 420, pp. 54-61 (In Spanish, submitted by invitation)

Patent Application:

Kuwabara, O., Radermacher, R., Hwang, Y., **Ling, J.,** Air conditioning system with heat pump regenerated desiccant wheel, submitted to USPTO 12/850943

Kuwabara, O., Radermacher, R., Hwang, Y., **Ling, J.,** Air conditioning system with heat pump regenerated desiccant wheel, submitted to JPTO P100133601

Invention Disclosures:

Kuwabara, O., Radermacher, R., Hwang, Y., **Ling, J.,** Air conditioning system with heat pump regenerated desiccant wheel, University of Maryland invention disclosure, PS 2010006

Kuwabara, O., Radermacher, R., Hwang, Y., **Ling, J.,** Commercial refrigeration system with desiccant wheel, University of Maryland invention disclosure, PS 2010007

Kuwabara, O., Radermacher, R., Hwang, Y., **Ling, J.,** Commercial refrigeration system using liquid coolant which absorbs moisture, University of Maryland invention disclosure, PS 2010008

Kuwabara, O., Radermacher, R., Hwang, Y., **Ling, J.,** Refrigerator and desiccant dehumidifier using 2-stage compression cycle, University of Maryland invention disclosure, PS 2010009

7.3 Future work

While this dissertation provides a comprehensive study on the understanding of the energy saving potential of SSLC system and thermal comfort created by low ΔT heat exchangers, the following items of research could be of significant use in the near future.

- To establish a closer link between the low ΔT heat exchanger simulation and thermal comfort prediction. The current work simplifies the heat exchanger as a constant wall temperature boundary condition to the thermal comfort simulation. Therefore, the next phase research should focus on simulating the heat exchanger using a more sophisticated model like the segment-by segment method. A more sophisticated heat exchanger model helps to provide the user with more direct information, such as how to design the tube length, tube pitch, etc., of heat exchanger based on specified thermal comfort requirements
- To test the low ΔT heat exchanger's performance in cooling mode. The current experiments of low ΔT heat exchanger were conducted in winter for heating, therefore the next phase of experiments would be to compare the thermal comfort zone created by the window-type AC unit and the low ΔT heat exchanger
- To add furniture (desk, cabinets) and lights into mean radiation temperature calculation model
- To expand the CFD simulation of air temperature in an enclosure from 2-dimension to 3-dimension
- To expand the usage of the POD method to different room geometries and different boundary condition inputs. The current work for the POD simulation code

restricts the room size to be 3 m by 3 m and the wall temperature difference to be 15 K. For other geometries and temperature differences, the entire database of snapshot needs to be rebuilt. It would be extremely helpful to explore an extrapolate method to expand the boundary condition inputs of POD method to more general cases.

References

Adbullah, A., & Mohamad, A. (2008). Enhancement of natural convection heat transfer from a fin by triangular perforation of bases parallel and toward its tip. *Applied Mathematics and Mechanics, 29*(8), 1033-1044.

Ahmed, C., Gandhidasan, P., Zubair, S., & Al-Farayedhi, A. (1998). Exergy analysis of a liquid-desiccant-based hybrid air-conditioning system. *Energy, 23*, 51-59.

AHRI. (2008). *ANSI/ARI Standard 210/240 for Performance rating of unitary air-conditioning and air-source heat pump equipment.* Arlinton: Air-Conditioning and Refrigeration Institute.

Ameen, A., Mollik, S., Mahmud, K., Quadir, G., & Seetharamu, K. (2006). Numerical analysis and experimental investigation into the performance of a wire-on-tube condenser of a retrofitted refrigerator. *International Journal of Refrigeration, 29*(3), 495-504.

ANSI/ASHRAE Standard 140. (2004). *Standard Method of Test for the Evaluation of Building Energy Analysis Computer Program.* Atlanta, GA, USA: ASHRAE.

ANSI/ASHRAE Standard 62.1. (2004). *Ventilation for Acceptable Indoor Air Quality.* Atlanta, GA, USA: ASHRAE.

ANSYS, Inc. (2006). Fluent version 6.3.26.

ANSYS, Inc. (2011). Gambit version 2.3.16.

Aounallah, M., Belkadi, M., Adjlout, L., & Imine, O. (2005). 2005. *International Journal of Heat Technology, 23*(2), 123-128.

ASHRAE . (2008). *ASHRAE Handbook: HVAC Systems and Equipment Chapter 37: Compressors.* Atlanta, GA, USA: ASHRAE.

ASHRAE. (2004). *ANSI/ARI Standard 55-2004: Thermal Environmental Conditions for Human Occupancy.* Atlanta: American Society of Heating, Refrigerating and Air-Conditioning Engineers Inc.

ASHRAE. (2005). *ASHRAE Handbook: Fundamentals Chapter 35: Duct design.* Atlanta, GA, USA: ASHRAE.

ASHRAE. (2007). *Handbook - HVAC Applications Chapter 53.* Atlanta, GA: American Society of Heating Refrigerating and Air-conditioning Engineers Inc.

ASHRAE. (2008). *ASHRAE Handbook: HVAC Systems and Equipment.* Atlanta, GA, USA: ASHRAE.

Bansal, P., & Chin, T. (2003). Modelling and optmisation of wire-and-tube condenser. *International Journal of Refrigeration, 26*(5), 601-613.

Bean, R., Olesen, B. W., & Kim, K. W. (2010). History of Radiant Heating & Cooling Systems, Part 2. *ASHRAE Journal, 52*(2), 50-55.

Bean, R., Olsen, B. M., & Kim, K. W. (2010). History of Radiant Heating & Cooling Systems, Part 1. *ASHRAE Journal, 52*(1), 40-47.

Bennakhi, A., & Chamkha, A. (2007). Conjugate natural convection in a square enclosure with inclined thin fin of arbitrary length. *International Journal of Thermal Sciences, 46*(5), 467-478.

Ben-Nakhi, A., & Chamkha, A. (2007). Conjugate natural convection in a square enclosure with inclined thin fin of arbitrary length. *Journal of Thermal Sciences, 46*, 467-478.

Berkooz, G., Holmes, P., & Lumely, J. L. (1991). Intermittent dynamics in simple modles of the wall layer. *Journal of Fluid Mechanics, 230*, 75-95.

Berkooz, G., Holmes, P., & Lumley, J. (1993). The proper orthogonal decomposition in the analysis of turbulent flows. *Annu. Rev. Fluid Mech., 33*, 539-575.

Bouali, H., Mezrhab, A., Amaoui, H., & Bouzidi, M. (2006). Radiation-natural convection heat transfer in an inclined rectangular enclosure. *International Journal of Thermal Sciences, 45*(6), 553-566.

Buyuk, O. (2009). Natural covnection of water-based nanofluids in an inclined enclosure with a heat source. *International Journal of Thermal Sciences, 48*(11), 2063-2073.

Casas, W., & Schmitz, S. (2005). Experiences with a gas driven, desiccant assisted air conditioning system with geothermal energy for an office building. *Energy and Buildings, 37*, 493-501.

Casson, V., Cavallini, A., Cecchinato, L., Col, D., Doretti, L., Fornasieri, E., et al. (2002). Performance of finned coil condensers optimized for new HFC refrigerants. *ASHRAE Transactions, 108*(2), 517-527.

Chiu, H., Jang, J., & Yan, W. (2007). Combined mixed convection and radiation heat transfer in rectangular ducts rotating about a paralle axis. *International Journal of Heat and Mass Transfer, 50*(21-22), 4229-4242.

Chiu, H., Jang, J., & Yan, W. (2007). Mixed convection heat transfer in horizontal rectangular ducts with radiation effects. *International Journal of Heat and Mass Transfer, 50*(15-16), 2874-2882.

Cormack, D., Leal, L., & Imberger, J. (1974). Natural convection in a shallow cavity with differetially heated end walls, Part 1: Asymptotic theory. *Journal of Fluid Mechanics, 65*(2), 209-229.

Cuckovic-Dzodzo, D. (1999). Laminar natural convection in a fully partitioned enclosure containing fluid with nonlinear thermo. *International Journal of Heat and Fluid Flow, 20*(6), 614-623.

Dai, Y., Wang, R., Zhang, H., & Yu, J. (2001). Use of liquid desiccant cooling to improve the performance of vapor compression air conditioning. *Applied Thermal Engineering, 21*, 1185-1202.

de Vahl Davis, G. (1968). Laminar natural convection in an enclosed rectangular cavity. *International Journal of Heat and Mass Transfer, 11*(11), 1675-1693.

Dhar, P., & Singh, S. (2001). Studies on solid desiccant based hybrid air-conditioning systems. *Applied Thermal Enginering, 21*, 119-134.

Dialameh, L., Yaghoubi, M., & Abouali, O. (2008). Natural convection from an array of horizontal rectangular thick fins with short length. *Applied Thermal Engineering, 28*(17-18), 2371-2379.

Domanski, P., Yahsar, D., & Kim, K. (2005). Performance of finned-tube evaporator optimized for different refrigerants and its effect on system efficiency. *International Journal of Refrigeration, 28*, 820-827.

Dunkle, R. (1963). Configuration factors for radiant heat transfer calculations involving people. *Journal of Heat Transfer*, 71-76.

Ede, A. (1967). Advances in free convection. *4*, 1-62.

Fanger, P. O. (1967). Calculation of thermal comfort - introduction of a basic comfort equation. *ASHRAE Transactions, 73*(2), 111.4.1-111.4.20.

F-chart Software. (2009). Engineering Equation Solver (EES).

Feingold, A., & Gupta, K. (1970, February). New analytical approach to the evaluation of configuration factors in radiation from spheres and infinitely long cylinders. *Journal of Heat Transfer*, 69-76.

Frederick, R. (2007). Heat transfer enhancement in cubical enclosures with vertical fins. *Applied Thermal Engineering, 27*(8-9), 1585-1592.

Fujii, M. (2007). Enahancement of natural convection heat transfer from a vertical heated plate using inclined fins. *Heat Transfer - Asian Research, 36*(6), 334-344.

Gebhart, B. (1971). *Heat transfer* (2nd Edition ed.). Mcgraw-Hill Book Company.

Ghali, K. (2008). Energy savings potential of a hybrid desiccant dehumidification air conditioning system in Beirut. *Energy Conversion and Management, 49*, 3387-3390.

Glück, B. (1993). Empfindungstemperatur und ihre Meßbarkeit. *Gesundheits-Ingenieur, 114*(3), 134-142.

Gupta, J., & Ramgopal, M. (2008). Modeling of hot-wall condensers for domestic refrigerators. *International Journal of Refrigeration, 31*(6), 979-988.

Han, T., Huang, L., Kelly, S., Huizenga, C., & Hui, Z. (2001). *Virtual thermal comfort engineering.* SAE.

Heatex AB. (2009). Heatex Select software package version 4.7.0. Sweden.

Heindel, T. (1996). Enhancement of natural convection heat transfer from an array of discrete heat sources. *International Journal of Heat and Mass Transfer, 39*(3), 479-490.

Henkes, R., & Hoogendoorn, C. (1995). Comparison exercise for computations of turbulent natural convection in enclosures. *Numerical Heat Transfer Part B, 28*, 59-78.

Hwang, Y. (2004). Potential energy benefits of integrated refrigeration system with microturbine and absorption chiller. *International Journal of Refrigeration, 27*, 816-829.

International Organization of Standardization. (1998). *ISO 7726: 1998 Ergonomics of the thermal environment - Instruments for measuring phsyical quantities.* Geneva, Switzerland: International Organization of Standardization.

ISO. (2005). *ISO standard 7730: 2005, Ergonomics of the thermal environment - Analytical determination and interpretation of thermal comfort using calculation of the PMV and PPD indices and local thermal comfort criteria.* Geneva: International Organization for Standardization.

ISO. (2005). *ISO standard 8996: 2004, Ergonomics of the thermal environment - Determination of metabolic rate.* Geneva: International Organization for Standardization.

ISO. (2007). *ISO 9920:2007, Ergonomics of the thermal environment - Estimation of thermal insulation and water vapor resistance of a clothing ensemble.* Geneva: International Organization for Standardization.

Jia, C., Dai, J., Wu, J., & Wang, R. (2006). Analysis on a hybrid desccant air-conditioning system. *Applied Thermal Engineering, 26*, 2392-2400.

Katjanekarn, T., & Kumar, S. (2008). Performance of a solar-regenerated liquid desiccant ventilation pre-conditioning system. *Energy and Buildings, 40*, 1252-1267.

Kaynakli, O., Pulat, E., & Kilic, M. (2005). Thermal comfort during heating and cooling periods in an automobile. *Heat and Mass Transfer, 41*(5), 449-458.

Koepke, M. (2011). *Experimental investigations on the thermal comfort of an office setting conditioned by low dT heat exchangers.* Technishce Universitat Berlin & University of Maryland.

Kopko, W. L. (2002). *Patent No. US 6,405,543 B2.* US.

Krishnan, A., Premachandran, B., Balaji, B., & Venkateshan, S. (2004). Combined experimental and numerical approaches to multi-mode heat transfer between vertical parallel plates. *Experimental Thermal and Fluid Science, 29*, 75-86.

Kuznetsov, G., & Sheremet, M. (2009). Conjugate natural convection with radiation in an enclosure. *International Journal of Heat and Mass Transfer, 52*(9-10), 2215-2223.

Liaqat, A. (2001). Conjugate natural convection in a square enclosure containing volumetric sources. *International Journal of Heat and Mass Transfer, 44*(17), 3273-3280.

Ling, J., Hwang, Y., & Radermacher, R. (2010). Theoretical study on separate sensible and latent cooling air-condition system. *International Journal of Refrigeration, 33*(3), 510-520.

Ly, H. V., & Hein, T. T. (2001). Modeling and control of physical processes using proper orthogonal decomposition. *Math. Comput. Modelling, 33*, 223-236.

Ma Q., W. R. (2006). Performance analysis on a hybrid air-conditioning system of a green building. *Energy and Buildings*, 447-453.

Malkus, W., & Veronis, G. (1958). Finite amplitude cellular convection. *Journal of Fluid Mechanics, 4*(3), 225-260.

MathWorks, Inc. (2008). Matlab 2008a version 7.6.0.324.

McQuiston F., P. J. (2005). *Heating, ventilation, and air conditioning: analysis and design.* John Wiley & Sons Inc.

Melo, C., & Hermes, C. (2009). A heat transfer correlation for natural draft wire-and-tube condensers. *International Journal of Refrigeration, 32*(3), 546-555.

Neti, S., & Wolfe, E. (Applied Thermal Engineering). 2000. *Measurements of effectiveness in a silica gel rotary exchanger, 20*, 309-322.

Olesen, B. W., Hasebe, Y., & de Dear, R. J. (1988). Clothing insulation asymmetry and thermal comfort. *ASHRAE Transactions, 94*(1), 32-51.

Ostrach, S. (1964). Laminar flows with body forces. *High Speed Aerodynamics and Jet Propulsion Theory - Theory of laminar flows, 4*, 528-718.

Ostrach, S. (1982). Natural convection heat transfer in cavities and cells. *1*, pp. 365-379. Munich: Proceedings of Seventh International Heat Transfer Conference.

Ostrach, S. (1988). Natural convection in enclosures. *Journal of Heat Transfer, 110,* 1175-1190.

Ostrach, S., & Hantman, R. (1981). Natural convection inside a horizontal cylinder. *Chemistry Engineeing Community, 9,* 213-243.

Park, H. M., & Jung, W. S. (2001). The Karhunen-Loeve Galerkin method for the inverse natural convection problems. *International Journal of Heat and Mass Transfer, 44*, 155-167.

Parsons, K. (2001). Introduction to thermal comfort standards. *Moving Thermal Comfort Standards into the 21st Century Conference*, (pp. 537-548). Windsor.

Patankar, S. V. (1980). *Numerical Heat Transfer and Fluid Flow.* New York: McGraw-Hill.

Pearson, A. (2005). Carbon dioxide - new uses for an old refrigerant. *International Journal of Refrigeration, 28*(8), 1140-1148.

Premachandran, B., & Balaji, C. (2006). Conjugate mixed convection with surface radiation from a horizontal channel with protruding heat sources. *International Journal of Heat and Mass Transfer, 49*(19-20), 3568-3582.

Rambo, J. (2006). *Reduced-order modeling of multiscale turbulent convection: application to data center thermal management.* Georgia Institute of Technology.

Rao, V., Naidu, S., Rao, B., & Sharma, K. (2006). Heat transfer from a horizontal fin array by natural convection and radiation-a conjugate analysis. *International Journal of Heat and Mass Transfer, 49*(19-20), 3379-3391.

Riesz, F., & Nagy, B. S. (1990). *Functional Analysis.* New York: Dover Publications.

Riffat, S. B., Zhao, X., & Doherty, P. S. (2004). Review of research into and application of chilled ceilings and displacement ventilation systems in Europe. *International Journal of Energy Research, 28*, 257-286.

Rohan, D. M., Tzempelikos, A., & Horton, W. T. (2010). Development of an advanced radiation exchange module for use in simulation of spaces with radiant systems. *International High Performance Buildings Conference at Purdue.* West Lafayette.

Sabet, M., & Chung, B. (1987). Radiation view factors from a sphere to nonintersecting planar surfaces. *Journal of Thermophysics, 2*(3), 286-288.

Schluter, A., Lortz, D., & Busse, F. (1965). On the stability of steady finite amplitude convection. *Journal of Fluid Mechanics, 23*(1), 129-144.

Sharma, A., Velusamy, K., Balaji, C., & Venkateshan, S. (2007). Conjugate turbulent natural convection with surface radiation in air filled rectangular enclosures. *International Journal of Heat and Mass Transfer, 50*(3-4), 625-639.

shimizu, S., Hara, H., & Asakawa, F. (1983). Analysis on air-conditioning heat load of a passenger vehicle. *International Journal of Vehicle Design, 4*(3), 293-311.

Sigey, J., Gatheri, F., & Kinyanjiu, M. (2004). Numerical study of free convection turbulent heat transfer in an enclosure. *Energy Conversion and Management, 45*, 2571-2582.

Stene, J. (2005). Residential CO2 heat pump system for combined space heating and hot water heating. *International Journal of Refrigeration, 28*(8), 1259-1265.

Tagliafico, L., & Tanda, G. (1997). Radiation and natural convection heat transfer from wire-and-tube heat exchangers in refrigeration applicances. *International Journal of Refrigeration, 20*(7), 461-469.

Talukdar, P. (2004). Combined radiation and convection heat transfer in a porous channel bounded by isothermal parallel plates. *International Journal of Heat and Mass Transfer, 47*(5), 1001-1013.

Tamura, T., Yakumaru, Y., & Nishiwaki, F. (2005). Experimental study on automotive cooling and heating air conditioning system using CO2 as a refrigerant. *International Journal of Refrigeration, 28*(8), 1302-1307.

Tanabe, S., Arens, E. A., Bauman, F. S., Zhang, H., & Madsen, T. L. (1994). Evaluating thermal environments by using a thermal manikin with controlled skin surface temperature. *ASHRAE Transactions, 100*(1), 39-48.

Tsuji, T., Kajitani, T., & Nishino, T. (2007). Heat transfer enhancement in a turbulent natural convection boundary layer along a vertical flat plate. *International Journal of Heat and Fluid Flow, 28*(6), 1472-1483.

Uponor GmbH. (2010). *Uponor Product catalog.* Retrieved 12 8, 2010, from http://www.catalog.uponor.com/index.php?id=28&no_cache=1&L=DEde&tx_uponorproduct_pi1[child]=569

Van Lear, B., & Sparrow, E. (2010). Enhancment of naural convection fins by high-frequency forced oscillations. *International Journal of Heat and Mass Transfer, 53*(7-8), 1570-1574.

walgama, C., Fackrell, S., Karimi, M., Fartaj, A., & Rankin, G. W. (2006). Passenger thermal comfort in vehicles - a review. *Proceedings of the Institution of Mechanical Engineers, Part D: Journal of Automobile Engineering. 220*, pp. 543-562. Professional Engineering Publishing.

Whitman, B., Johnson , B., & Tomczyk, J. (2004). *Refrigeration and Air Conditioning Technology.* Delmer Cengage Learning.

Wikipedia. (n.d.). *the Free Encyclopedia*. Retrieved from http://en.wikipedia.org/wiki/Sensible_heat

Winter, D. A. (1979). *Biomechanics of human movement.* New York: John Wiley & Sons Inc.

Yadav, Y. (1995). Vapor-compression and liquid-desiccant hybrid solar space-conditioning system for energy conservation. *6*(7), 719-723.